

BIOLOGICALLY INSPIRED HAIRY SURFACES FOR LIQUID REPELLENCY

By

SHU-HAU HSU

A DISSERTATION PRESENTED TO THE GRADUATE SCHOOL  
OF THE UNIVERSITY OF FLORIDA IN PARTIAL FULFILLMENT  
OF THE REQUIREMENTS FOR THE DEGREE OF  
DOCTOR OF PHILOSOPHY

UNIVERSITY OF FLORIDA

2010

© 2010 Shu-Hau Hsu

To my lovely Mom and Dad

## ACKNOWLEDGMENTS

I would like to first and foremost thank Dr. Wolfgang Sigmund, who is not only just an adviser but an incredibly energetic mentor and scientist. His vision, compassion, support, understanding and guidance helped me through the entire work. I would also like to thank my committee members, Drs. Moudgil, Baney, El-Shall, and C-Y Wu for their constructive comments. Also, I would like to thank Dr. Tonia Hsieh at Temple University for the extensive discussions on biological system. I would like to recognize the help of the staff of MAIC (Materials Analytical Instrument Center) and PERC (Particle Engineering Research Center) regarding the characterization of the surface properties.

There are also a lot of students and friends who without their help I would not have finished this work. I would like to acknowledge all the past and current members in the Sigmund's group for assisting me in many ways during my work. I particularly thank former group member, Yi-Chung Wang, for the preparation of the fluorocarbon coated samples. Special thanks would need to go to the people who had lived in Arbor (Howard, Ian, Kenneth, Sophia, Pei-Ching and Ray) for sharing the life in Gainesville.

Last but not least, I am extremely grateful to my parents for their love and unselfish support throughout my study in United States. Without them, this dissertation would have never been accomplished.

## TABLE OF CONTENTS

	<u>page</u>
ACKNOWLEDGMENTS.....	4
LIST OF TABLES.....	8
LIST OF FIGURES.....	9
LIST OF ABBREVIATIONS.....	14
ABSTRACT.....	16
CHAPTER	
1 INTRODUCTION.....	18
Water Repellent Interfaces: A Green Technology.....	18
Superhydrophobic Surfaces in Nature.....	19
Research Objectives.....	21
2 PRINCIPLES OF LIQUID-REPELLENT SURFACES.....	24
Issues of Wetting on Solid Surfaces.....	24
Surface Tension.....	24
Wetting on Ideal Smooth Surfaces.....	25
Wetting on Roughened Surfaces I: Wenzel Model.....	26
Wetting on Roughened Surfaces II: Cassie-Baxter Model.....	27
Transition Between Cassie-Baxter and Wenzel State.....	27
Contact Angle Hysteresis and Sliding Angle.....	28
Water Repellent Surfaces from Nature.....	30
Plant Kingdom.....	31
Animal Kingdom.....	33
3 FABRICATION OF ARTIFICIAL HAIRY SURFACES.....	41
Experimental Work of Making Hairy Surfaces.....	41
Self-Assembly of Hair-Like Structure.....	42
Materials Selection.....	42
Experimental procedure.....	42
Characterization.....	43
Making Hairy Surfaces via Moulding Techniques.....	43
Casting with lithographed moulds.....	44
Casting with natural leaves.....	45
Casting with commercial porous membrane.....	45
Characterization of surface morphology.....	47

Characterization of thermal properties .....	47
Characterization of mechanical properties .....	48
Experimental Results .....	48
Making Hairy Surface via Self-Alignment of Carbon Nanotubes .....	48
Colloidal carbon nanotubes.....	48
Results and discussion .....	49
Making Hairy Surfaces via Moulding Technique.....	51
Casting with lithographed moulds .....	51
Casting with natural leaves .....	52
Making Hairy Surfaces via Moulding with Commercial Membranes .....	53
Membrane casting on elastomer .....	53
Membrane casting on thermoplastic polymers.....	54
Issues of the current membrane casting .....	59
General Discussion.....	62
The Artificial Hairy Surfaces .....	62
The Scope of the Casting Process .....	63
Durability of the Cast Structure.....	65
Summary .....	66
<b>4 WETTABILITY OF HAIRY SURFACES .....</b>	<b>92</b>
Contact Angle Measurement .....	92
Concerns of Contact Angle Measurement.....	93
Fitting Model of Contact Angle Measurement.....	94
Experimental Work of Wettability Evaluation .....	95
Static Contact Angle Measurement .....	95
Contact Angle Hysteresis Measurement .....	96
Video Assessment of the Surface Hydrophobicity .....	97
Surface Tension Determination .....	97
Contact Area and Theoretical Contact Angle Interpretation .....	98
Wetting Property of Hairy Plants.....	98
Observations on Hairy Leaves .....	98
Droplets on Hairy Plants.....	99
Wetting Property of Artificial Hairy Surfaces .....	101
Contact Angles of Cast PDMS Surface .....	101
Contact Angles of Cast Thermoplastic Surface .....	102
Polypropylene substrate .....	103
LDPE substrate.....	106
PVDF substrate.....	106
Perfectly Hydrophobic Response .....	106
Self-Cleaning Ability .....	109
General Discussion.....	110
Summary .....	114

5	TOWARDS SUPEROLEOPHOBIC SURFACES .....	134
	Experimental Work of Plasma Treatment .....	134
	Introduction.....	134
	Surface Treatment with Water Plasma.....	135
	Surface Treatment with Fluorocarbon Plasma Deposition .....	136
	Characterization of Plasma Treated Surface.....	137
	Surface morphology .....	137
	Surface chemistry .....	137
	Contact angle measurement.....	138
	Experimental Results.....	138
	Surface with Water Plasma Treatment.....	138
	Surface with Fluorocarbon Coating .....	139
	General Discussion.....	141
	Summary .....	143
6	CONCLUSIONS AND SUGGESTIONS FOR FUTURE WORK.....	153
	Conclusions .....	153
	Suggestions for Future Work .....	155
	The Role of Elasticity on Water Repellency.....	155
	Quantitative Study of Self-Cleaning Effect.....	155
	LIST OF REFERENCES .....	157
	BIOGRAPHICAL SKETCH.....	165

## LIST OF TABLES

<u>Table</u>		<u>page</u>
3-1	List of materials for casting hairy surfaces in this study.....	69
3-2	Glass transition temperature ( $T_g$ ) and melting point ( $T_m$ ) of the thermoplastics used in this work.....	88
3-3	Mechanical properties of the thermoplastics used in mould casting.....	89
4-1	Measured surface tensions of the liquids used in contact angle measurement.....	118
4-2	Contact angles of all the cast thermoplastic surfaces and the theoretical contact angles calculated from Cassie-Baxter theory.....	122
5-1	Liquid drops on plasma treated 0.6 $\mu$ m-peeled PP samples. ....	147
5-2	Contact angles of low surface tension liquids on cast PP surfaces before and after CF coatings. ....	151

## LIST OF FIGURES

<u>Figure</u>	<u>page</u>
1-1 SEM images of lotus leaf surface. ....	23
1-2 SEM image of lady's mantle leaf, stem of <i>Dicliptera Suberecta</i> and stem of tomato. ....	23
2-1 Schematic diagram of liquid molecules at the surface and the surface tension..	36
2-2 Wetting behavior of a liquid droplet on solid surface and their mathematical models. ....	37
2-3 Contact angle hysteresis is the angle difference between $\theta_{adv}$ and $\theta_{rec}$ . ....	38
2-4 Relationship between sliding angles and contact angle hysteresis .....	38
2-5 Few examples of microscopic morphology of water-repellent leaf surfaces. ....	39
2-6 SEM micrographs of a lady's mantle leaf .....	39
2-7 SEM images of the hair layer of the water strider's body.....	40
2-8 Hairs protrude from the leg of fish spider, and Plastron of fish spider, visible as a silver envelope around the body and legs. ....	40
3-1 Schematic procedure of self-alignment of functionalized carbon nanotubes with polyelectrolytes. ....	67
3-2 The procedure of high-aspect-ratio surface structure by photolithography and e-beam lithography.....	68
3-3 Creating negative PDMS elastomer mould by using leaf <i>Dicliptera Suberecta</i> as a positive mould.....	69
3-4 Two commercial membranes, AAO and PC, used for casting.....	70
3-5 The procedure of casting PDMS elastomer with polycarbonate and alumina membranes.....	71
3-6 The procedure of casting thermoplastics substrate with polycarbonate membrane. The membrane is removed by either direct peeling or dissolving. ....	72
3-7 $T_g$ is determined by the midterm point B from curve obtained by DSC analysis. ....	73
3-8 Standard dog-bone shaped samples for ultimate tensile test. ....	73

3-9	A typical tensile stress-strain curve and the represented properties for polymeric materials.....	73
3-10	Zeta-potential of functionalized and non-functionalized carbon nanotubes showing the shift of the IEP (isoelectrical point). ....	74
3-11	SEM picture of Si substrate after immersed into colloidal CNTs suspension ....	74
3-12	The surface structure of cast PDMS elastomer from moulds developed by photolithography and by electron beam lithography .....	75
3-13	SEM pictures showed the hairs structures of Dicliptera Suberecta and Lady's Mantle.....	75
3-14	The surface morphology of cast PDMS elastomer by using Dicliptera Suberecta as master moulds.....	76
3-15	Lady's Mantle was dehydrated after curing process making it very difficult to be removed from the PDMS elastomer. ....	76
3-16	A negative PDMS mould after peeling off the leaf of Lady's Mantle .....	77
3-17	The interface of PDMS substrate cast by PC membrane .....	77
3-18	PDMS substrate cast with different pore size PC membrane.....	78
3-19	The microstructure of PP substrate cast with AAO membrane ( $\phi=0.2\mu\text{m}$ ) .....	79
3-20	PP substrate cast with different pore size PC membrane. The membrane was dissolved after casting.....	80
3-21	Top-viewed post structure of cast PP substrate after dissolving the membrane. ....	81
3-22	SEM images of PP substrate cast with different pore size PC membranes.....	82
3-23	SEM images of LDPE substrate cast with different pore size PC membranes... ..	83
3-24	SEM images of PVDF substrate cast with different pore size PC membranes... ..	84
3-25	SEM images of PS and PMMA substrates cast with PC membrane. ....	85
3-26	DSC analysis curve of PP substrate.....	86
3-27	DSC analysis curve of LDPE substrate .....	86
3-28	DSC analysis curve of PVDF substrate .....	87
3-29	DSC analysis curve of PS substrate.....	87

3-30	DSC analysis curve of PMMA substrate.....	88
3-32	Comparison between the surface microstructure on PP substrate after peeling off the PC membrane and the microstructure of water strider's abdomen. ....	90
3-33	Images of Immersed regular PP substrate and PP substrate with artificial hairy structure.....	90
3-34	SEM images of cast PP and PVDF substrates before and after being rubbed by fingers.....	91
4-1	Contact angle measurement on a superhydrophobic surface with different diameters of syringe .....	116
4-2	Images of the same water droplet on a superhydrophobic surface under different fitting modes of the static contact angle.....	116
4-3	The equipment set-up of goniometer. ....	117
4-4	The interface of DropSnake program. ....	117
4-5	Selected sequential images during contact/compression/release test on a superhydrophobic surface. ....	118
4-6	Schematic picture of Wilhelmy plate method of measuring liquid surface tension.....	118
4-7	The fraction of contact area is estimated by adjusting the threshold of top-view SEM pictures. ....	119
4-8	Water droplets on the leaf of Lady's Mantle .....	120
4-9	Stereo microscopic Images of a droplet on the leaf of Lady's Mantle.....	120
4-10	Variety of hair density of the leaves of Lady's Mantle leaves. ....	121
4-11	Morphology of different cast PDMS surfaces and their contact angles.....	121
4-12	The surface morphology of the membrane-dissolved PP surfaces and their sessile drop images.....	123
4-13	The surface morphology of the membrane-peeled PP surfaces and their sessile drop images.....	124
4-14	The surface morphology of the membrane-peeled LDPE surfaces and their sessile drop images.....	125

4-15	The surface morphology of the membrane-peeled PVDF surfaces and their sessile drop images.....	126
4-16	The images of contact angle measurement acquiring from goniometer. (a) a steel ball and (b) a droplet on cast PP hairy surface. ....	127
4-17	Selected images during contact/compression/release test on a perfectly hydrophobic hairy PP substrate.....	127
4-18	Selected images during contact/compression/release test on a non-perfectly superhydrophobic PP substrate.....	128
4-19	Selected images during motion test on 0.6 $\mu$ m-peeled hairy PP substrate.....	129
4-20	Schematic diagram of self-cleaning effect (Lotus effect) .....	130
4-21	Water droplets on an uncast PP sheet contaminated by carbon powder. ....	131
4-22	Water droplets on an cast hairy PP surface contaminated by dirt particles. ....	132
4-23	Two configurations of models for water-repellent hair pile.....	133
4-24	The interaction between water droplet and artificial hairy surface. ....	133
5-1	Schematic diagram of the water plasma system used in this work.....	145
5-2	Photo of the water plasma chamber used in this work. ....	145
5-3	Schematic diagram of the STS deep reactive ion etch system.....	146
5-4	Schematic diagram of the typical process of deep reactive ion etching.....	146
5-5	The morphology of hairy surface before and after Ar plasma.....	148
5-6	The surface morphology of CF coated PP samples after casting process. ....	148
5-7	The hairy structure before and after plasma deposition of CF layer in DRIE chamber. ....	149
5-8	Contact angles of methanol-water mixture on hairy surfaces coated with different plasma power. ....	149
5-9	XPS results of CF coated surfaces under different plasma power.....	150
5-10	Low contact angle of nonpolar liquid (dodecane) on CF coated hairy PP surfaces.....	150
5-11	Low surface tension liquid (dodecane) on PVA and (b) pHEMA substrates .....	152

5-12 Schematic diagrams of interfacial force when a liquid with contact angle  $\theta_c$  on the non-reentrant and reentrant structure..... 152

## LIST OF ABBREVIATIONS

AAO	anodic aluminum oxide
ASTM	American Society for Testing and Materials
CAD	computer aided design
CB	Cassie-Baxter
CCD	charge-coupled device
CF	fluorocarbon
DRIE	deep reactive ion etching
DSC	differential scanning calorimetry
HMDS	hexamethyl-disilazane
ICP	induced coupled plasma
IEP	iso-electrical point
LDPE	low-density polyethylene
MeOH	methanol
MWCNT	multi-walled carbon nanotube
PC	polycarbonate
PDAC	poly(diallyldimethylammonium chloride)
PDMS	polydimethyl siloxane
PMMA	polymethyl methacrylate
PP	polycarbonate
PS	polystyrene
PVDF	polyvinylidene fluoride
RF	radio frequency
RFGD	radio frequency glow discharge
SEM	scanning electron microscope

THF	tetrahydrofuran
XPS	x-ray photoelectron spectroscopy
$A_{LV}$	contact area of liquid/vapor interface
$A_{SL}$	contact area of solid/liquid interface
$A_{SV}$	contact area of solid/vapor interface
$f_s$	area fraction of liquid/solid interface
$f_v$	area fraction of liquid/vapor interface
$R_f$	roughness factor
$T_g$	glass transition temperature
$T_m$	melting temperature
$\gamma$	surface tension
$\gamma_c$	critical surface tension
$\gamma_{LV}$	surface tension of liquid/vapor interface
$\gamma_{SL}$	surface tension of solid/liquid interface
$\gamma_{SV}$	surface tension of solid/vapor interface
$\lambda_p$	linear fraction of contact line
$\Delta\theta$	contact angle hysteresis
$\theta_c$	contact angle of liquid to solid
$\theta_w$	contact angle of Wenzel state
$\theta_{CB}$	contact angle of Cassie-Baxter state
$\theta_{adv}$	advancing contact angle of liquid
$\theta_{rec}$	receding contact angle of liquid
$\theta_{trans}$	transition contact angle
$\theta_{slide}$	sliding angle of drops

Abstract of Dissertation Presented to the Graduate School  
of the University of Florida in Partial Fulfillment of the  
Requirements for the Degree of Doctor of Philosophy

## BIOLOGICALLY INSPIRED HAIRY SURFACES FOR LIQUID REPELLENCY

By

Shu-Hau Hsu

December 2010

Chair: Wolfgang M. Sigmund  
Major: Materials Science and Engineering

Owing to remarkable features, such as self-cleaning, anti-biofouling and drag reduction, interest on rendering surfaces water-repellent has significantly grown within this decade. Attempts on making surfaces “superhydrophobic”, where high water contact angle ( $\theta_c > 150^\circ$ ) accompanied with only few degrees of roll-off angle, have been extensively demonstrated through the mimicking of the surface chemistry and morphology of lotus leaves. This appealing phenomenon also exists on another structure from nature: surfaces comprising soft hairs. Although the role of this piliferous integument has long been recognized for providing life, arthropods in particular, water-repellency, the synthetic superhydrophobic surfaces based on this structure are still very limited.

In this study, the goal was to develop a novel liquid-repellent surface by mimicking the hairy exterior of species. The artificial hairy surfaces were prepared by means of pressurized membrane casting, in which thermoplastic sheets were forced to flow into porous membranes at elevated temperature. The  $\Gamma$ -shaped pillars on the membrane cast polypropylene substrate are particularly similar to the conformation of natural hairs.

The principle of this fabrication technique is relatively accessible and is expected to be compatible with large-area fabrication of superhydrophobic interfaces.

The artificial hairy surface features perfectly hydrophobic response where no contact angle hysteresis was observed from video assessment. Thus the artificial hairy surface of the current work appears to be the first report to have such extreme hydrophobicity with only structural modification from the original substrate. This ultralow adhesion to water droplet is believed to be attributed to the hydrophobic methyl groups and the mechanical response of the artificial hairs. Liquid repellency of the hairy surfaces was further enhanced by coating with fluorocarbon (CF) layers via deep reactive ion etching (DRIE). The contact angle of water-methanol mixture ( $\gamma < 35.2$  mN/m) was raised from  $60^\circ$  to around  $140^\circ$ . The surface energy of coated samples, however, was still not low enough to repel non-polar liquids. Moreover, the hairy structure is not favorable for maintaining the low surface tension liquid in Cassie-Baxter state.

## CHAPTER 1 INTRODUCTION

### **Water Repellent Interfaces: A Green Technology**

Research on how liquids act on solid surfaces dates back to the early 19th century when P. S. Laplace and T. Young studied capillary action.<sup>1</sup> The study, dealing with the cohesion of water molecules and adhesion of those molecules to solid materials, uncovered some fundamental aspects of wetting on solid materials. In the modern study of this field, significant interest has been directed towards the control of the degree of surface wetting, especially in rendering surface liquid repellent.<sup>2-6</sup> Liquid droplets show low adhesion to these particular engineered surfaces and are easily to be shed. Some applications based on this similar response can be seen in our daily lives, such as non-stick frying pans, rain repellent windshields, or waterproof fabrics, where less effort is needed to clean surfaces or keep them dry.

In the last decade, extreme water-repellency existing in some natural species has specifically caught people's attention. Their exteriors show a very high water contact angle ( $\theta_c > 150^\circ$ ) with only a few degrees of contact angle hysteresis, which enables water droplets to form spherical beads and to be shaken away from the surfaces quickly. This superior water-repellent behavior is now generally recognized as *Superhydrophobicity* (where *hydro-* and *phobos* stand for water and fear respectively in Attic Greek). Some crucial functions for these species are provided through this property, such as the reduction of surface contamination from microorganisms, and the performance of locomotion on water or to sustain the impact from raindrops. Interests have not only increased concerning the science behind this unique phenomenon, but

also concerning the design and fabrication of the superb anti-wetting surfaces. A few remarkable applications of the superhydrophobic surface may include:

- **Self-cleaning surfaces:** One of the most astonishing phenomena of the superhydrophobic surface is its self-cleaning ability, on which water droplets pick up the dirt and remove it while rolling off from the surface. With less consumption of water as well as small required force for removing the dirt, the superhydrophobic surfaces effortlessly remain smudge free.
- **Anti-biofouling surfaces:** Surfaces showing superhydrophobicity may have potential to reduce the undesired adherence of the microorganisms, plants and algae to the surfaces. This function merely results from the architecture of the surface, rather than chemistry responses.<sup>7</sup> This is considered to be more environmentally friendly, since toxic coatings, such as tributyltin (TBT) and triphenyltin (TPT), for marine hulls may be avoided.<sup>8</sup>
- **Drag force reduction:** As a thin air layer is trapped on the superhydrophobic interface, the direct interaction between solid and fluid is diminished. The reduction of the drag force can be as high as 50%.<sup>9</sup> A more energy efficient watercraft could be designed by covering it with a water-repellent surface.

All these features are leading us to applications concerning the conservation of the natural environment and the reduction of resource consumption, which are two of the biggest concerns this century. Along with other developments in surface science, superhydrophobic surfaces in turn provide a significant contribution to green technology.

### **Superhydrophobic Surfaces in Nature**

Water-repellent and hydrophobic properties of many plants and living creatures have been acknowledged for a long time. The most well-known example is observed on the leaves of lotus (*Nelumbo Nucifera*), which beautifully demonstrates the self-clean ability owing to its superior water repellency.<sup>10,11</sup> Despite emerging from muddy marshlands, the lotus flower has stood as a symbol of purity in Asian culture for centuries. Barthlott and Neinhuis<sup>10</sup> examined the surface morphology of water repellent leaves by using electron microscopy. Figure 1-1 shows these water repellent leaves were found to have micrometer scale protrusions (~ 1 $\mu$ m) covered with nanometer sized

epicuticular wax crystals (~20 nm). A water droplet on the lotus leaf typically shows a contact angle larger than  $150^\circ$  accompanying with only few degrees of the contact angle hysteresis. Since then, many attempts have been made to imitate the now so-called “*Lotus Effect*,” where strategies are based on discoveries from the lotus, the combination of hydrophobic coatings and the surface roughness.

The hydrophobic nature of the wax crystals as well as the multiple-scaled roughness they generate on lotus leaf plays key roles in having strong water repellency. The mechanism, which heavily relies on chemistry, however turns out to have some restrictions. For instance, these so-called superhydrophobic surfaces show remarkably decreased repellency to hot water (50–80°C).<sup>12</sup> This may arise from the dissolving of the wax crystals while leaves getting in contact with hot water droplets.

Another type of leaf showing this amazing water-repellent property is found to be very different from lotus leaf. These plants, such as the Lady’s Mantle (*Alchemilla vulgaris*), Tomato or *Dicliptera Suberecta*, comprising a plurality of flexible hairs (trichomes) on their leaves and stems, exhibit a feature similar to “*Lotus effect*”. Water droplets on their fuzzy leaves can be suspended by the trichomes, which effectively prevent the droplets from wetting the leaf. (Figure 1-2b, c, d) Although the leaf itself shows an excellent hydrophobicity, those trichomes were found to be hydrophilic.<sup>13</sup> This is somewhat surprising since based on a classical model a roughened hydrophilic surface will tend to be even more hydrophilic.<sup>14</sup> Which indicates making superhydrophobic surfaces out of hydrophilic materials is possible with an appropriate geometry of surface structure.

In addition to the plants, this piliferous exterior plays a more crucial role for numerous arthropods by not only effectively protecting their bodies from getting wet, but by providing various functions for their living activities. These hairs protrude several micrometers from their cuticles, typically inclined at certain angles, with diameters in the micrometer to submicrometer range. These structures can resist the impact of raindrops,<sup>15</sup> allow locomotion on the surface of water,<sup>16</sup> or even trap a layer of air for respiration when submerged<sup>17,18</sup>. Legs of water striders, composed of numerous hair-like setae with diameters in micrometer, have water contact angle above 160°, which in turn provide a great supporting force and enable them to walk on water.<sup>19</sup>

### **Research Objectives**

While the water-repellent property of those hairy structures has been recognized for over 100 years,<sup>20</sup> unlike lotus effect, only a few studies have been reported on the creation of the superhydrophobic hairy surfaces. The main reason is making this high-aspect-ratio structure is relatively difficult by using top-down technique.<sup>21</sup> Moreover, obtaining the unique arrangement of these natural hairs is also a challenge. Two studies were published demonstrating attempts to duplicate the hairy structure via a two-step casting technique by using species as the template for the mould.<sup>22,23</sup> Although one report of a cast surface showed superhydrophobicity, only samples with small area could effectively be prepared.<sup>23</sup> Therefore, our major efforts focus on creating artificial hairy surfaces and to study their wetting behavior in-depth. The hypotheses of this study are set as:

- (1) The surface covered with hair-like structures can be made on some specific substrates at moderate size.
- (2) Surfaces with artificial hair will feature superhydrophobicity.

- (3) Surface with artificial hair is able to repel low surface tension liquids without a further modification of their surface chemistry.

The following specific objectives are set in this dissertation to verify the hypotheses.

- (1) Develop an effective method to fabricate surfaces covered with high-aspect ratio flexible materials for scientific investigation.
- (2) Characterize these hairy structures, their hair surface density, shape and geometry as well as key material properties such as thermal, mechanical and surface chemical properties.
- (3) Examine the wetting properties, including contact angles and contact angle hysteresis for a variety of liquids ranging from water to hydrocarbons.
- (4) Modify the surface chemistry to explore the limitation of the prepared hairy structures towards specific liquids and analyze data with current theories.
- (5) Provide hypotheses for explaining the liquid repellency of hairy surfaces.

In order to provide a comprehensive overview of this research, a general review of the science concerning wetting behavior is presented in Chapter 2. The classic Wenzel and Cassie-Baxter models together with other recent theoretical works are described. The main work of this research is given in the rest of the chapters. Each chapter contains its own perspective, and it starts with the main experimental work, which is followed by a presentation and discussion of the results. Chapter 3 focuses on the making of the artificial hairy surfaces and the major protocol of fabrication of the liquid repellent surfaces is presented. The main characterization of the wetting properties of the hairy surfaces will be described in Chapter 4. In Chapter 5, making artificial hairy surfaces towards repelling organic liquids is described and discussed. The culmination of these findings lead to a general conclusion in Chapter 6, in which the possibility of future work on this topic is suggested, since the research initiates another possibility to make surfaces liquid repellent. The possible implications are also presented in this chapter as well.

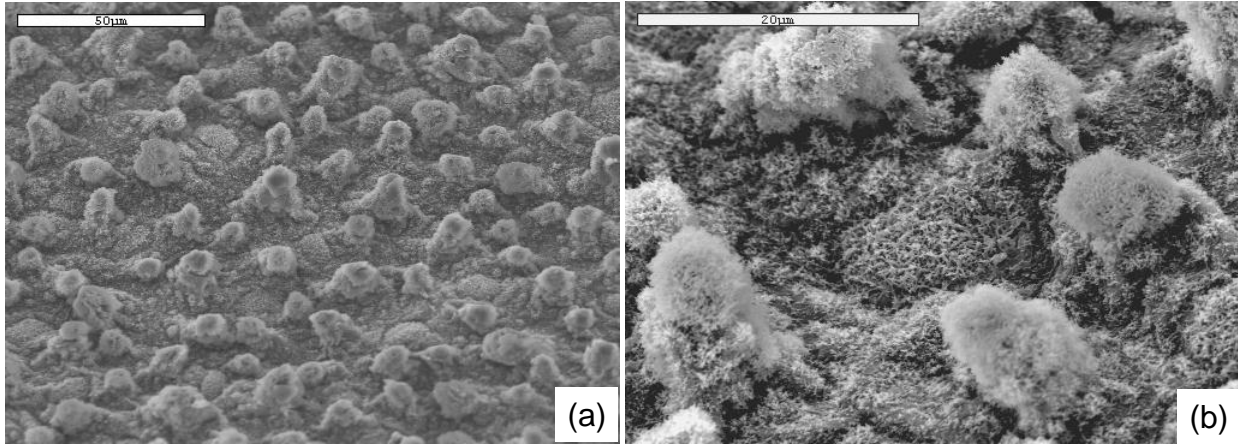


Figure 1-1. SEM images of lotus leaf surface where it is covered with micron-sized protrusions (a), and (b) submicron-sized wax crystals.

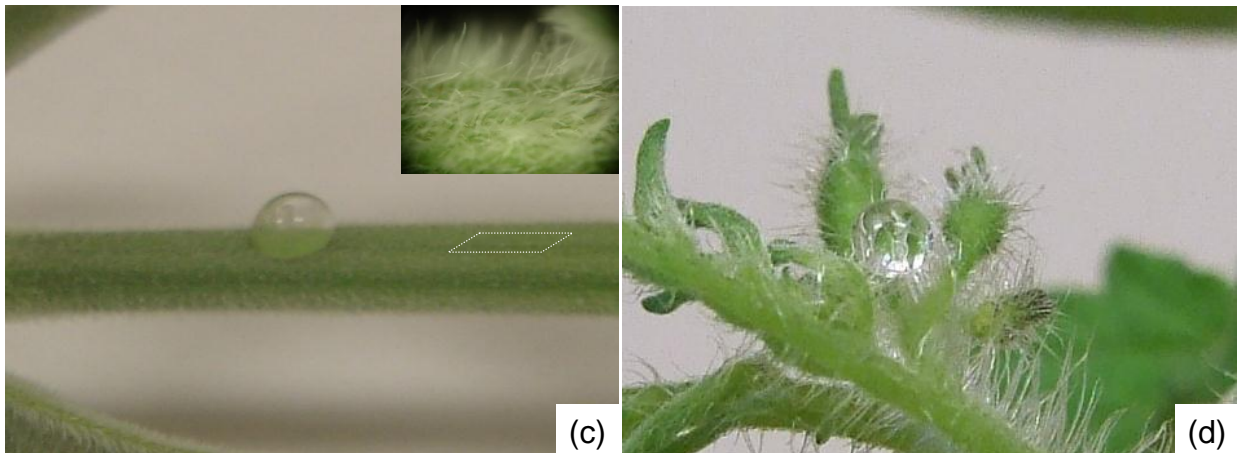
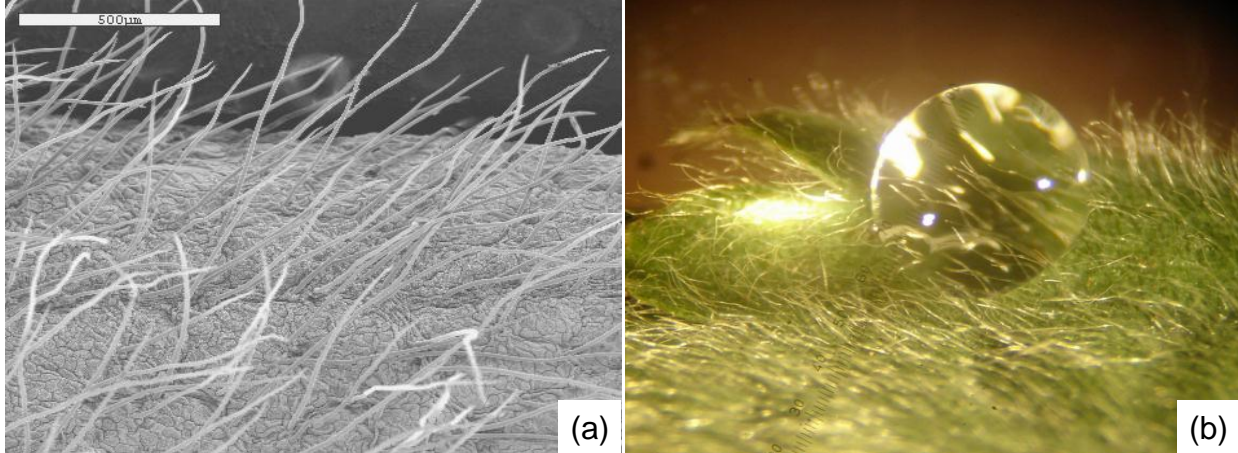


Figure 1-2. (a) SEM image showing the lady's mantle leaf densely covered with hairs (trichomes). Water droplet which is supported by the hairs (b) leaf of lady's mantle, (c) stem of *Dicliptera Suberecta* and (d) stem of tomato.

## CHAPTER 2 PRINCIPLES OF LIQUID-REPELLENT SURFACES

The purpose of this chapter is to provide readers with essential background knowledge while moving towards the preparation of liquid-repellent interfaces. Hence an overview of the theoretical and experimental work regarding liquid-repellency is presented. The chapter begins with the fundamental aspects of wetting behavior, and advances with some mathematical models. Since this dissertation is inspired by some cuticles of natural species, an exploration of different water repellent surfaces discovered from nature is provided. The major strategies and examples that make surfaces liquid repellent are briefly given at the end of this chapter.

### **Issues of Wetting on Solid Surfaces**

#### **Surface Tension**

Surface tension is a property of the surface of a liquid or solid. Surface tension is caused by the imbalance of the attraction force at the surface where the molecules are surrounded by a reduced number of similar atoms or molecules than those in the interior. (Figure 2-1a) This causes liquid molecules at the surface to be in an energetically unfavorable state, and therefore the surface generates a force to minimize its free surface area. This force is usually characterized quantitatively as the surface tension ( $\gamma$ ) in fluid system, or free surface energy for solid materials, which is the energy required for creating a unit area of the surface at constant pressure and temperature. The units can be interpreted either as tension force per unit length of a line (e.g. N/m) or as energy per unit surface area (e.g. J/m<sup>2</sup>) at the surface (Figure 2-1b).

The system energy of two solid and liquid phases will be lowered if they are in contact with each other. This is expressed by the Young-Dupré equation:<sup>24</sup>

$$W_{SL} = \gamma_{SV} + \gamma_{LV} - \gamma_{SL} \quad (2-1)$$

where  $W_{SL}$  is the work of cohesion per unit area between two surfaces,  $\gamma_{SV}$  and  $\gamma_{SL}$  are the surface tensions of the solid against vapor and liquid, and  $\gamma_{LA}$  is the surface tension of liquid against vapor.

### Wetting on Ideal Smooth Surfaces

Wetting of a solid surface is usually characterized by contact angle ( $\theta_c$ ), which is the angle where the three different phases meet one another (Figure 2-2a). The value of the angle is determined by three surface tensions where the chemical potential in the three phases should be equal. Considering a liquid drop on a solid surface, the total energy of the system,  $E$ , is expressed as

$$E = \gamma_{LV}(A_{LV} + A_{SL}) - W_{SL}A_{SL} \quad (2-2)$$

where  $A_{LV}$  and  $A_{SL}$  are the contact areas of the liquid with the solid and vapor, respectively. At the equilibrium state,  $dE = 0$ ; therefore,

$$\gamma_{LA}(dA_{LA} + dA_{SL}) = W_{SL} dA_{SL} \quad (2-3)$$

It is generally assumed that the gravitational potential energy can be neglected, and the volume and pressure are constant. The angle between the three phases can be given by geometrical considerations, which is

$$dA_{LV}/dA_{SL} = \cos\theta_c \quad (2-4)$$

Therefore, the contact angle  $\theta_c$  can be obtained from the combination of Eqs. (2-1), (2-3) and (2-4).

$$\cos\theta_c = (\gamma_{SV} - \gamma_{SL}) / \gamma_{LV} \quad (2.5)$$

This is the Young's equation for the determination of contact angles.<sup>1</sup>

The wettability of a surface is commonly evaluated by the apparent liquid contact angle. If the value of the static contact angle is  $0^\circ \leq \theta_c \leq 90^\circ$ , the liquid tends to spread on the surface. It is usually referred to as *hydrophilic* or *oleophilic* surface in terms of aqueous or oily liquid, respectively. If the value of the contact angle is  $90^\circ < \theta_c \leq 180^\circ$ , the wet area tends to shrink. It is then referred to as *hydrophobic* or *oleophobic* surface in terms of aqueous or oily liquid, respectively. Surfaces with the water contact angle between  $150^\circ$  and  $180^\circ$  are usually called superhydrophobic.

### **Wetting on Roughened Surfaces I: Wenzel Model**

The Young's equation is an oversimplified expression, and is only valid for ideally flat surfaces that are atomically smooth and chemically homogeneous. Conversely, very few solids are atomically flat. Wetting on rough surfaces was first considered by Wenzel.<sup>14</sup> In the Wenzel state, where the roughness grooves are completely filled with liquid (Figure 2-2b), the contact angle ( $\theta_w$ ) can be described by

$$\cos \theta_w = R_f [(\gamma_{SV} - \gamma_{SL}) / \gamma_{LV}] \quad (2-5)$$

where  $R_f$  is the surface roughness factor, which is defined as

$$R_f = (\text{Actual Area}) / (\text{Projection Area}) \quad (2-6)$$

Combining eq. (2-6) with Young's equation yields

$$\cos \theta_w = R_f \cos \theta_c \quad (2-7)$$

Since the roughness factor is always larger than unity in a practical situation, therefore it is obvious that the apparent angle on a roughened surface will become smaller if its intrinsic contact angle on a smooth surface is less than  $90^\circ$ . The apparent contact angle will be larger, if its intrinsic contact angle is larger than  $90^\circ$ .

## Wetting on Roughened Surfaces II: Cassie-Baxter Model

The Wenzel regime is usually recognized as homogeneous wetting, since the liquid completely penetrates into the grooves. While under some circumstances, especially the increase of the surface roughness, vapor pockets may be trapped underneath the liquid yielding a composite interface. (Figure 2-2c) This heterogeneous wetting is usually described by Cassie-Baxter (CB) theory,<sup>25</sup> from which the apparent contact angle ( $\theta_{CB}$ ) is given by equation (2-8),

$$\cos\theta_{CB} = f_s \cos \theta_c + f_v \cos \theta_v \quad (2-8)$$

where  $\theta_c$  is the intrinsic contact angle on the original smooth surface, and  $f_s$  and  $f_v$  are the area fractions of the solid and vapor on the surface, respectively. Since  $f_s + f_v = 1$ , and  $\theta_v = 180^\circ$  (This implies that a suspended liquid droplet in air is a perfect sphere.), equation (2-8) can be rewritten as follows:

$$\cos\theta_{CB} = f_s (\cos \theta_c + 1) - 1 \quad (2-9)$$

From equations 2-9, it can be found that droplets will have a higher apparent contact angle if less area is being in contact with the solid substrate. The CB equation simply indicates the contact angle can be increased even when the intrinsic contact angle of a liquid on the original smooth surface is less than  $90^\circ$ .

## Transition Between Cassie-Baxter and Wenzel State

The apparent contact angle for a rough surface can be given by the equation (2-7) and (2-9), depending on the solid-liquid interface. It has also been reported that the solid-liquid contact mode may change from the CB state to the Wenzel state by applying a small pressure, evaporating some liquid, or adjusting the volume of the droplet.<sup>26-28</sup> A transition between these two wetting states can occur, and there is a critical value of  $f_s$ ,

below which the CB regime exists and above which the Wenzel regime is thermodynamically more stable.<sup>29-32</sup> During the transition, the droplet will penetrate into the groove of structure, and the equation should be still valid before and after the transition. The threshold value  $\theta_{trans}$  between the two modes can therefore be obtained by combining eq. (2-7) and (2-9),<sup>33</sup>

$$\cos \theta_{trans} = (f_s - 1)/(R_f - f_s) \quad (2-10)$$

Hence if the contact angle is lower than the threshold angle  $\theta_{trans}$ , the trapped air pockets underneath will be thermodynamically unfavorable and the Wenzel mode will be easily obtained. To have a droplet to agree with the CB model, the solid substrate must be hydrophobic enough or  $\theta_{trans}$  must be as small as possible, because the underneath trapped air pockets will be only stable when contact angle above  $\theta_{trans}$ .

### **Contact Angle Hysteresis and Sliding Angle**

The fundamental aspects of static contact angles are described in the previous sections. In addition to static behavior, the contact angle hysteresis, and the sliding behavior of liquid droplets are also dominated factors for the evaluation of the liquid repellency of a surface.

The contact angle hysteresis is an important characteristic of a solid-liquid interface which is induced by the roughness and chemical inhomogeneity of a surface. Superhydrophobicity means not only a high contact angle, but also a low hysteresis of the contact angle. Contact angle hysteresis,  $\theta_{hys}$ , defined by equation (2-11),

$$\theta_{hys} = \Delta\theta = \theta_{adv} - \theta_{rec} \quad (2-11)$$

Where  $\theta_{adv}$  and  $\theta_{rec}$  are advancing and receding angles, respectively. For a given solid substrate, a range of static contact angle may be observed. The advancing contact

angle is the maximum value of contact angle before the liquid-solid contact line starts to advance, and receding angle is the minimum value of contact angle before the liquid-solid contact line starts to retreat. (Figure 2-3) Therefore, the measured contact angle lies anywhere within the range  $\theta_{adv} > \theta_c > \theta_{rec}$ . Advancing and receding angles are usually determined by sessile drop measurement, where liquid is progressively pumped into or withdrawn from the droplet to constantly vary the contact angle and record their values when the contact line migrates.

Low contact hysteresis of superhydrophobic surfaces is responsible for the self-cleaning properties, which means that a water droplet can easily roll off the surface and pick up dust from the surface.<sup>11,34,35</sup> The degree of rolling-off behavior of a liquid droplet is measured by sliding angle,  $\theta_{slide}$ , at which a liquid droplet begins to roll or slide down an inclined plate. The sliding angle can be directly measured by titling the solid substrate to have the value. It can also be obtained from the contact angle hysteresis by using equation (2-11).<sup>36</sup>

$$mg(\sin\theta_{slide}) / w = \gamma_{LA} (\cos\theta_{rec} - \cos\theta_{adv}) \quad (2-11)$$

where  $\theta_{rec}$  and  $\theta_{adv}$  are the advancing and receding contact angles, respectively,  $g$  is the gravitational acceleration, and  $m$  and  $w$  are the mass and width of the droplet, respectively. The equation simply denotes that the lower contact angle hysteresis (smaller difference between the advancing and receding contact angles) the more easily the drop will slide. The force,  $F_{slide}$ , required to initiate the sliding of a drop over a solid substrate can also given by the contact angle hysteresis:<sup>40</sup>

$$F_{slide} = \gamma_{LA} (\cos\theta_{rec} - \cos\theta_{adv}) \quad (2-12)$$

If contact angle hysteresis is small, then only small external forces, like wind, gravity, or mechanical shaking can easily shed off the drops to have the surface dry.

Similar to static contact angles, contact angle hysteresis is also greatly dominated by the surface roughness.<sup>33</sup> When the droplet is in Wenzel state, the liquid droplet is mainly pinned on the substrate even it is tilted to a significant angle, while in CB state, the pinning barrier is more easily to be overcome even if the substrate is only slightly tilted. Therefore, increasing the surface roughness can be used to lower the sliding angle; unfortunately, to date there is no simple expression for the contact angle hysteresis as a function of roughness.<sup>4,5,94</sup> The contact mode can be switched continuously from Wenzel to CB states with increasing surface roughness.<sup>37,39</sup> The sliding behavior of a liquid droplet is also governed by the movement of the three-phase contact line toward its sliding direction.<sup>38,39</sup> With the same fraction of the solid phase, low contact angle or low sliding angle is favorable for a short continuous contact line. It is also found that water slides off more easily when moving in the direction parallel to the pillars.<sup>39</sup> Therefore, not only the surface roughness but also the surface geometrical structure need to be taken into account in order to prepare an effective superhydrophobic surface, where a high water contact angle and low sliding angle can be achieved.

### **Water Repellent Surfaces from Nature**

Many plants and arthropods are known for having their exterior water-resistant. With the advance of microscopy in the last few decades, a variety of microstructures is found on these surfaces which vigorously stimulate the research on making superhydrophobic surfaces. Here some remarkable water-repellent surfaces of plants and animals are presented from which the beauty of nature is amazed.

## Plant Kingdom

Lotus leaf (*Nelumbo nucifera*) has become the epitome of natural superhydrophobic surfaces. This strong water repellency leads Lotus leaf to another impressive ability, self-cleaning, where leaves remain unsmudged even being immersed into muddy water. Thus, in oriental cultures lotus is long considered as a sacred symbol of purity. Nowadays the ability of self-cleaning and water repellency is termed “Lotus effect”. Hydrophobicity and self-cleaning of leaves are suggested as a mechanism to resist harmful micro-organism bounding to the leaf surface, since water is usually required for the germination.

The relationship between surface roughness and wettability or particle deposition of the leaves has long been known;<sup>41</sup> however, systematically detailed investigation was not conducted until Neinhuis and Barthlott<sup>10,11</sup> studied more than 200 water-repellent plants via scanning electron microscopy where several types of epidermal relief, a single-layered group of cells covering a plant, and epicuticular wax crystals are reported. The epidermal relief is ranged from 5  $\mu\text{m}$  in multipapillate cells to 100  $\mu\text{m}$  in large epidermal cells. However, this variation in scale had almost no effect on wettability.<sup>11</sup> Overall, the SEM study reveals that the water-repellent leaf surfaces are all covered by small protrusions (Figure 2-5a and b) called papillae, which are covered by an additional layer of epicuticular waxes. (Figure 2-5c and d) The wax is present in crystalline tubules with water contact angles of about  $95^{\circ}$ – $110^{\circ}$ , which is considered hydrophobic.<sup>42</sup>

The superhydrophobicity of leaves is obviously dominated by their surface roughness. The papillae create the first-degree of roughness on which the wax crystals generate an additional roughness in a smaller length of scale. This kind of hierarchical

roughness on superhydrophobic surfaces seems to play a crucial role, but the detailed mechanism is not yet completely clear. Some explanations have been proposed to provide a reason why most natural surfaces are hierarchical.<sup>43-45</sup> This arrangement may be generated for having a general purpose: to repel both macroscopic and microscopic droplets.<sup>46-49</sup> Surfaces with only one scale of roughness repelled macroscopic droplets fairly well, while the condensation may easily form microscopic droplets between the grooves of the surface structure.<sup>50</sup>

While it is known that self-cleaning is mainly attributed to the strong water-repellency, to quantify the ability of self-cleaning is still a challenge. Therefore, a further study is needed to quantitatively address how these two properties are related to each other. It is usually believed that the dirt particles on a smooth surface are partially redistributed when water droplets slide away, while on a rough surface, the dirt particles easily adhere to the droplet interface and are removed away when the droplets roll off.<sup>11</sup>

The second type of surfaces is the leaves covered with soft dense hairs (trichomes), such as Lady's Mantle (*Alchemilla vulgaris* L.). These hairs with an aspect ratio above 100 have a diameter around 10  $\mu\text{m}$  and a height up to around 1 mm (Figure 2-6a). As presented in Chapter 1, water droplet rests on the trichomes as a perfect sphere (Figure 1-2b), whose apparent contact angle may be taken as  $180^\circ$ , without contacting to the leaf cuticle. The droplets also run off these leaves very easily, and consequently the leaves keep unwetted. Despite the difference of the morphology, the composition of these trichomes has some interesting features. Electron microscopy confirmed that the cuticle of the Lady's Mantle is covered with cuticular wax crystals (Figure 2-6b), similar to Lotus leaf. However, the contact angle of the trichomes is

shown to be below  $60^\circ$ ,<sup>13</sup> which indicates the trichomes are well hydrophilic. This is unexpected from a surface comprised of hydrophilic dense hairs, since liquid is supposed to be sucked into the brush as the capillary suction.

A model was proposed by Otten and Herminghaus<sup>13</sup>, in which the elasticity of the trichomes as well as the hydrophobicity from cuticular wax crystals are believed to be the main reasons for having strong water repellency. As trichomes are more hydrophobic than the cuticle, droplets tend to get in contact with the hairs. If the hairs' contact angle is different from  $90^\circ$ , the liquid surface will deform around the hair according to Young's equation. On the other hand, most of the hairs have to bend in order to form a bundle, which costs elastic energy. For a sample of infinite size, the combination of both contributions leads to a minimization of the total energy of the system if the hairs group into bundles of a particular size. This particular size depends on the height and separation of the hairs, their mechanical modulus and on the distance  $h$  between the leaf surface and the drop/air interface. As a result a water drop resting on such a bundle of hairs cannot come in contact with the substrate.

### **Animal Kingdom**

As presented in the previous section, the wettability of leaves is dominated by both their surface chemicals and the topography. Similar to plants, the principles also apply to living creatures whose cuticles are water repellent; however, this water-repellency or water-proofing provides more crucial functions for their living activity, such as to resist the impact of raindrops, to perform locomotion on the surface of water, or even to trap a layer of air for respiration when submerged. Two general criteria for having water-repellent surfaces: the resistance to fluid penetration and the resistance to adhesion by droplets. Thorpe and Crisp referred these two concepts as water- and rain-proofing

respectively for water-repellent insects.<sup>51</sup> Both water- and rain-proofing are enhanced by rigid roughened exterior, but the preferred morphologies are different for these two features. Higher solid-liquid contact is favored for water-proofing, while minimizing this contact will benefit rain-proofing as water droplets is more easily to be shaken off.

Similar to the water-repellent leaves, insect cuticle is covered with a layer of epicuticular wax that renders the exterior hydrophobic to ease the penetration of water. The presence of this waxy layer has long been known.<sup>52,53</sup> Holdgate<sup>15</sup> reported that the wax layer had two-way benefit. It is not only important in water-repellency, but also in water-retention: removing the wax layer of insects lead to their rapid desiccation.<sup>54</sup> The cuticle typically has numerous irregular structures such as hairs, scales and regions of varying curvature, all of which make the contact angle highly variable.<sup>55</sup> Here the attention is on the hairy structure, since the piliferous exterior is found in almost in all water-repellent arthropods and has been noted for over 100 years.<sup>20</sup> The characteristics of the hair layer of these water-repellent arthropods, however, have just been established within this 30 years via using scanning electron microscopy. The arthropods cuticle and its interaction with the free surface can be now qualitative elucidated with macrophotography.<sup>56</sup>

Figure 2-7 shows the hair layer of the water strider's body and its leg. The hair on strider's abdomen is tilted relative to the body surface. The hair tips are bent inwards towards the leg, which discourages their piercing the water surface. The hairs are typically 30  $\mu\text{m}$  long, tapering to a point from a 1  $\mu\text{m}$ -diameter base and inclined at an angle around  $30^\circ$  to the underlying leg surface, forming a layer 10  $\mu\text{m}$  thick. These hairs, termed macrotrichia, point in the direction of the leg tip, and bend inwards at their

tips so as to lie roughly tangent to the leg and water surface. The hair density varies along the leg: the density is  $4\text{--}6 \times 10^3$  hairs  $\text{mm}^{-2}$  on the front tarsus,  $1.2\text{--}1.6 \times 10^4$   $\text{mm}^{-2}$  on the middle tarsus and  $8\text{--}10 \times 10^3$   $\text{mm}^{-2}$  on the hind tarsus.<sup>56</sup> Their non-wetting piliferous legs have shown to have contact angles above  $150^\circ$ , and to provide a maximal supporting force of 152 dyne for each leg, which effectively enables water striders to stand and walk on water.<sup>19</sup>

Another example is the fish spider (*Argyroneta aquatica*) which is known to submerge and fish underwater with an trapped air layer that serves as an air supply (Figure 2-8).<sup>57</sup> When submerged the water spider as well as many insects appears to have shiny coatings owing to a total reflection from a thin layer of air trapped by their hair coating. The hair structure is thus necessary not only to lower the contact area with the water surface, but to enable these creatures to breathe when submerged. This activity is termed *Plastron respiration* as the hairs acting like a shield.<sup>17</sup> The oxygen and carbon dioxide are supplied and removed through the diffusion across the bubble surface from the ambient water. The structure of plastron hairs was extensively studied by Hinton<sup>18</sup> which illustrated the air layer is maintained by an array of hairs that their tips lie roughly parallel to the body. The air layer is then retained before the hairs collapsed due to the increase of water pressure.<sup>17,18</sup>

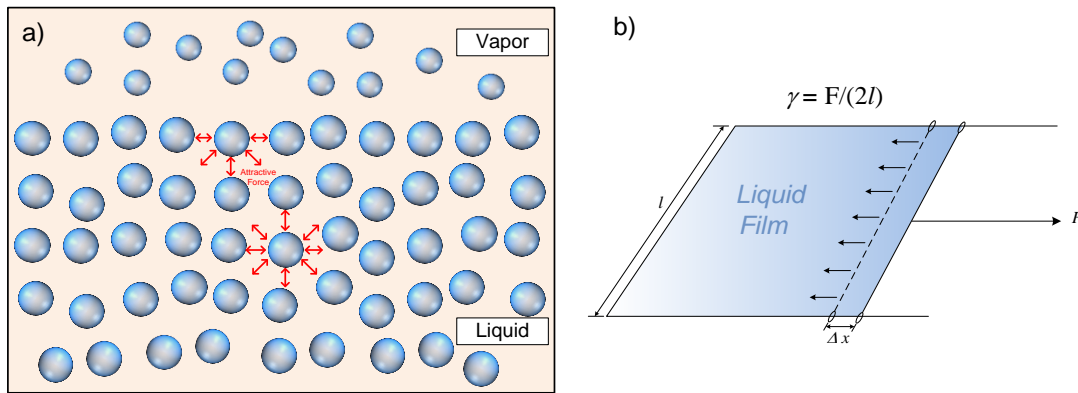
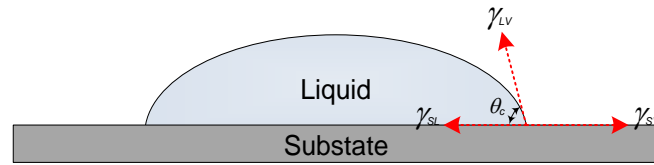
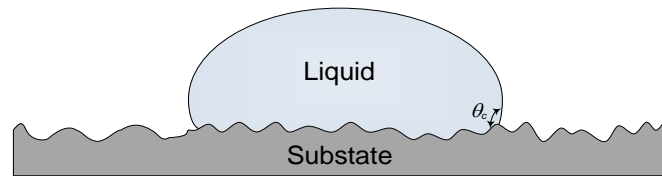


Figure 2-1. (a) Liquid molecules at the surface have fewer neighbors than interior molecules, and are in a higher state of energy. Therefore the system tends to minimize the total free surface area. (b) The surface tension ( $\gamma$ ) is a force per unit length of a film to resist the expansion of the surface area, or the work required to create a new unit surface area.

(a)



(b)



(c)

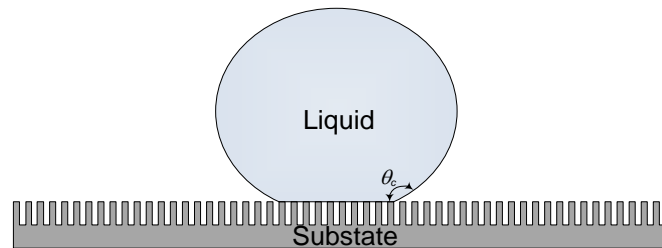


Figure 2-2. Wetting behavior of a liquid droplet on solid surface and their mathematical models. (a) A liquid droplet on an ideally flat surface, Young's equation, (b) Liquid droplet on a rough surface, Wenzel model, (c) Vapor pockets are trapped between the grooves and the liquid droplet, Cassie-Baxter model.

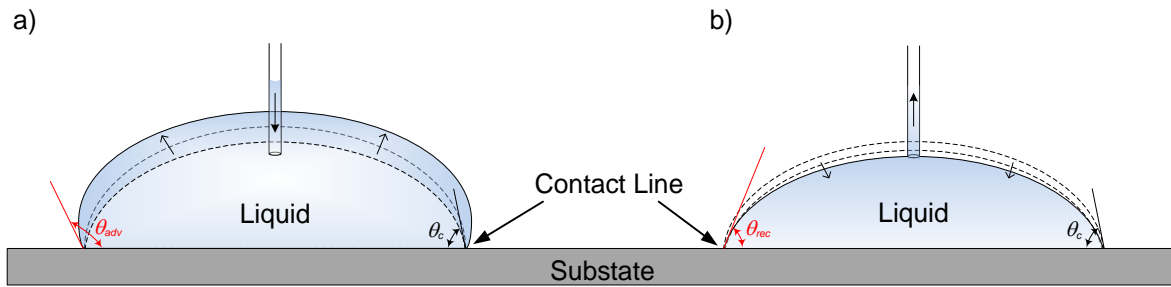


Figure 2-3. (a) Advancing angle ( $\theta_{adv}$ ) is the maximum contact angle of a droplet before its contact line (liquid-solid interface) starts advancing. (b) Receding angle ( $\theta_{rec}$ ) is the minimum contact angle of a droplet before its contact line starts receding. Contact angle hysteresis is the angle difference between  $\theta_{adv}$  and  $\theta_{rec}$ .

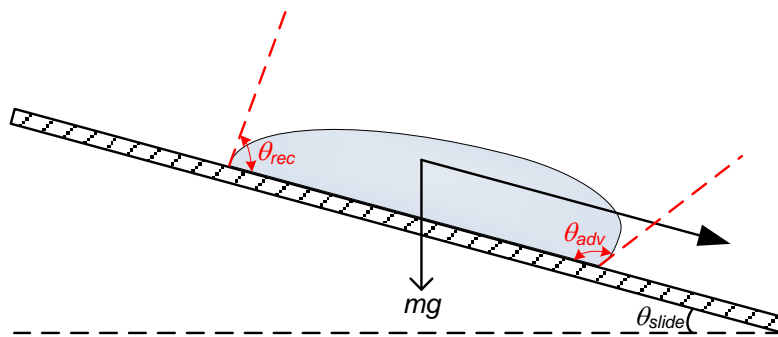


Figure 2-4. Relationship between sliding angles and contact angle hysteresis (advancing and receding angles)

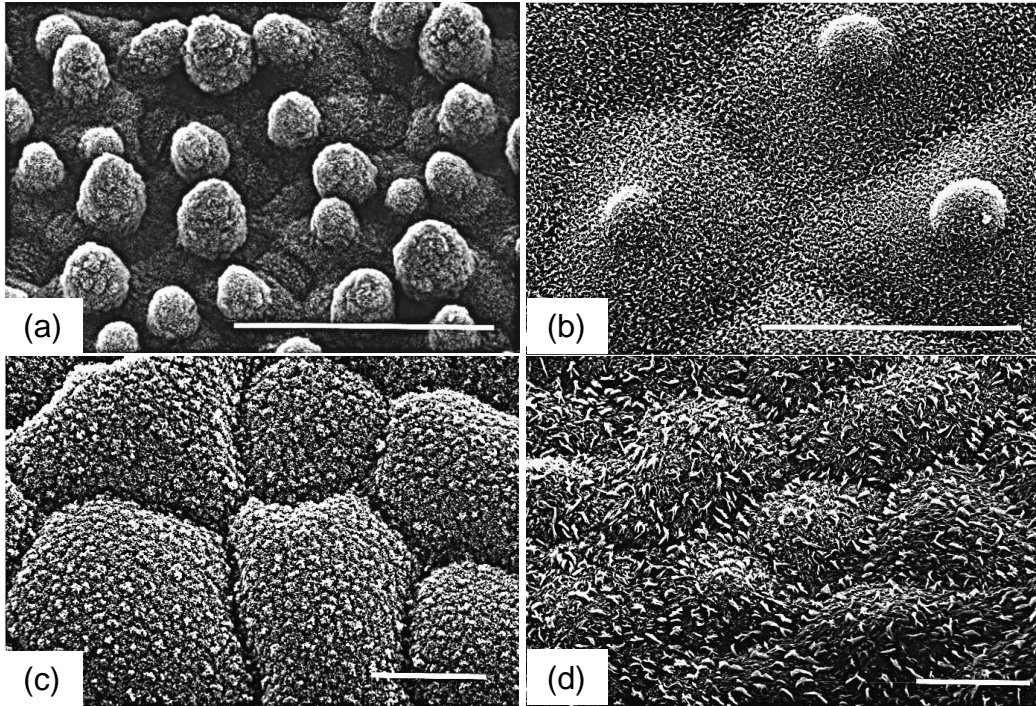


Figure 2-5. Few examples of micromorphological morphology of water-repellent leaf surfaces. Water repellent leaf surfaces of *Nelumbo nucifera* (a) and *Lupinus polyphyllus* (b). Bars=50  $\mu\text{m}$ . Every epidermal cell forms a papilla and is superimposed by a dense layer of epicuticular waxes. An increased roughness due to a differentiation within the wax layer: on the leaf surfaces of *Tropaeolum majus* (c) and *Melaleuca hypericifolia* (d). Bars=20  $\mu\text{m}$ .<sup>11</sup> (reproduced by permission of Oxford University Press)

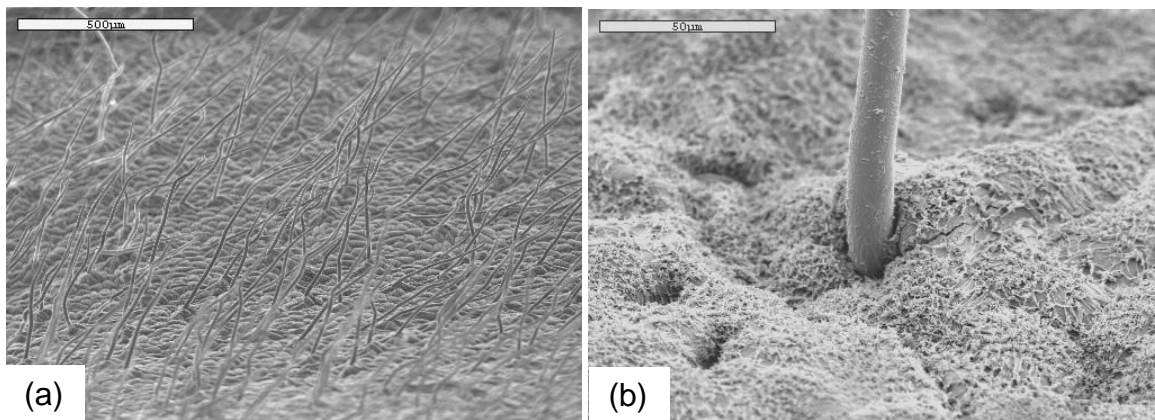


Figure 2-6. (a) SEM micrograph of a lady's mantle leaf covered with high-aspect ratio dense hairs. (b) The cuticular wax crystals on lady's mantle leaf.

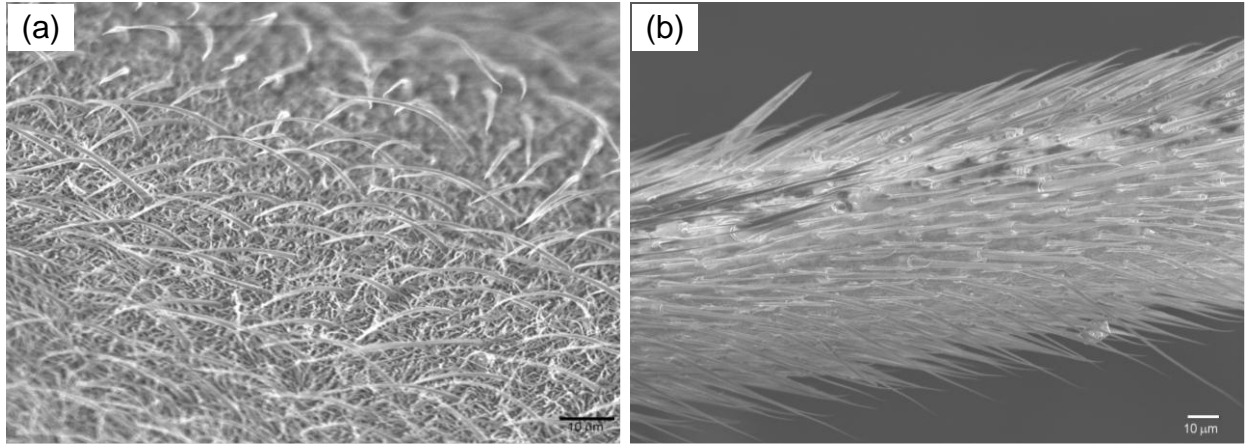


Figure 2-7 SEM images of the hair layer of the water strider's body. (a) The hair on strider's abdomen are tilted at around  $30^\circ$  relative to the body surface. (b) The hair on strider's leg. The hair tips are bent inwards towards the leg, which discourages their piercing the water surface.

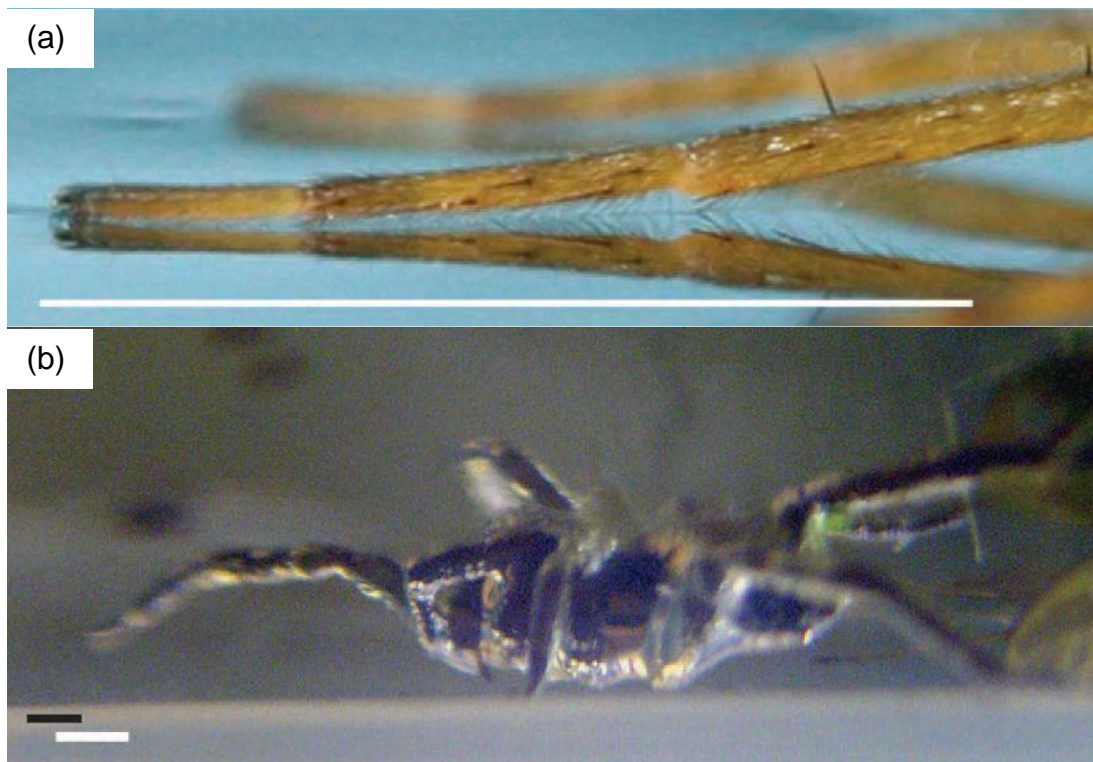


Figure 2-8. (a) Hairs protrude from the leg of fish spider, which allow water spider to perform locomotion on water. (b) Plastron of fish spider, visible as a silver envelope around the body and legs.<sup>56</sup> (reproduced by permission of *Elsevier Ltd.*)

## CHAPTER 3 FABRICATION OF ARTIFICIAL HAIRY SURFACES

This chapter focuses on the preparation of artificial hairy surfaces. Certain techniques, including self-assembly and moulding, that have been employed are presented here. The final objective is to obtain a practical approach that effectively fabricates artificial hairy surfaces which mimic the hairs from biological system and allow us to study their wetting properties. The chapter begins with a brief consideration on the strategy of making artificial hairy surfaces. All the experimental work is presented in the latter sections, although some of them are not used as the main process to make hairy surfaces. The challenge and the results, as well as the created morphology, are discussed in the second part of the chapter.

### **Experimental Work of Making Hairy Surfaces**

The first major task in the study is to create an interface covered with hair-like structure. The diameter of hairs on water-repellent creatures or leaves is generally located at micrometer range while their length can be up to a millimeter, which means the target aspect-ratio of the pillars could be as high as 100.<sup>13</sup> Making structure at such high aspect ratio is always a great challenge in microfabrication. Moreover, direct machining on soft materials is another concern, so making hair-like structure by means of top-down route is not considered as an option. Hence two different approaches used here to develop the hairy structure are self-assembly and moulding technique. Self-assembly is a process in which the pre-existing disordered substances spontaneously evolve into an ordered structure without applying an external guiding force. The moulding technique, which embosses the surfaces by forcing the materials into the

moulds and commonly used for constructing surface features, is chosen as another major method in this study.

## **Self-Assembly of Hair-Like Structure**

### **Materials Selection**

Carbon nanotubes were selected to create the hair-like structure in self-assembly process. Arc-discharge produced multi-wall carbon nanotubes (MWCNTs) in the form of soot were ordered from Alfa-Aesar, which contains 30-40% of carbon nanotubes, carbon nanoparticles, and fullerenes. All the following materials were obtained from Aldrich and used as received: poly(diallyldimethylammonium chloride) (PDAC, 20 wt% in water, molecular weight 400,000-500,000), sulfuric acid ( $\text{H}_2\text{SO}_4$ , 98%), and nitric acid ( $\text{HNO}_3$ , 70%). Diced Si wafer was used as the substrates for the self-alignment process.

### **Experimental procedure**

The carbon soot contains not only just carbon nanotubes but many other forms of carbon such as, carbon fibers, fullerenes and amorphous carbon. Since most of the impurities are carbon in nature, they can be removed by oxidization with strong acid. Acid treatment also functionalizes the carbon nanotubes in which the carboxylic groups are introduced onto the surface of carbon nanotubes which is essential for the following self-alignment coating process.

The arc-discharged carbon soot was initially ground with alumina molder and pestle to fine powder and then purified by oxidization to remove undesired impurities. The oxidization of ground carbon powder was performed by sonification in nitric acid ( $\text{HNO}_3$ , 70%) for 8 hours and then refluxed in an oil bath at  $140^\circ\text{C}$  for 24 hours. The precipitate was rinsed with the deionized water three times and functionalized by sonication in a mixture of sulfuric acid ( $\text{H}_2\text{SO}_4$ , 98%) and nitric acid ( $\text{HNO}_3$ , 70%)

(volume ratio 3:1) for 8 hours. The functionalized carbon nanotubes were then separated by centrifuging and washed with deionized water three times. After being dried at 100°C for 10 hours, functionalized MWCNTs were dispersed by sonicated in deionized water to form a stable solution. PDAC was dissolved in deionized water at a concentration of 1 mg/mL with 0.01 M NaCl for layer by layer assembly. A Si wafer was diced into pieces and cleaned by sonification in acetone for 30 minutes and then rinsed with methanol and deionized water.

A silicon substrate was immersed in PDAC solution for 10 minutes to form a polycationic surface layer. Functionalized MWCNTs were coated on the silicon substrate by immersing the substrates into the MWCNT solution for 5 to 8 hours. These steps were repeated till desired layers were obtained, and then the substrate was rinsed with deionized water and dried in oven at 120°C. The abstract of experimental procedure is given in Figure 3-1.

### **Characterization**

The colloid property of carbon nanotubes was characterized by Zeta potential. Dilute MWCNTs suspensions (0.01 wt%) at different pH were prepared by adding various amount of HCl and NaOH to the DI water, and their zeta potential was measured by ZetaPlus analyzer (Brookhaven Instruments Co., USA). The surface morphology of MWCNTs coated Si substrate was characterized by SEM (SEM JSM 6335, JEOL co.) with a thin layer of Pt-Au conductive coating.

### **Making Hairy Surfaces via Moulding Techniques**

A variety of template source was considered and tested here, including those making from lithography, natural leaves and commercial porous membranes.

## **Casting with lithographed moulds**

Two different irradiation sources, UV photons and electron beam, for lithography were tried here. Figure 3-2 shows a general procedure of making high-aspect ratio surface structure by means of lithography.

**Photolithography** Silicon wafers were used as the main substrate material here. They were cleaned by sonicating in acetone and isopropyl alcohol for 5-10 minutes, and then dried by a nitrogen gas flow. Thick-film photoresist (AZ 9260, MicroChemical GmbH) was coated onto the substrate by spinner coater and baked at 200°C for 30 minutes. The thickness, depending on the rotation speed, of the photoresist is around 10  $\mu\text{m}$ . The following exposure was carried out at wavelength of 365 nm with intensity at 40  $\text{mW}/\text{cm}^2$  by Karl Suss MA-6 contact mask aligner. After exposure, the surface feature was developed by immersing the substrate into the developer (AZ 400K diluted with deionized water in a 1:3 ratio, MicroChemical GmbH) for 5 minutes. A silicon elastomer PDMS (polydimethyl siloxane, Sylgard-184, Dow Corning Corp.) mixed with curing agent at 10 to 1 ratio was first degassed and then poured on the surface of the developed silicon mould. After curing at 80°C for 2 hours, the silicon mould was separated from the elastomer leaving the transferred pattern on it.

**Electron beam lithography** In order to create the patterns at submicron range, electron-beam (e-beam) lithography was also used. The preparation of substrates is similar to photolithography, but the surface feature is directly written by an energetic electron beam on electron-sensitive resist (950 PMMA, Microchem Nano Inc.). The PMMA resist was spin coated onto a substrate at 3000 rpm for 30 seconds using a spin coater (Model p6700, Specialty Coating Systems). The thickness of the PMMA was

~500 nm. The substrate was then hot baked on a hot plate for 10 minutes at 180°C for curing the PMMA resist. The pattern writing was carried out at 30 KeV by a scanning electron microscope (SEM, Philips XL-40 FEG) equipped with NPGS system (Nano Pattern Generating System, JC Nability Lithography Systems). The typical area dose for exposure is set to 600  $\mu\text{C}/\text{cm}^2$  at working distance 10 cm. After exposure, the written pattern was developed by immersing the substrate in a 1 to 3 solution of methyl-isobutylketone in isopropanol for about 75 seconds, and then rinsed by isopropanol before air dried. The deep reactive ion etching (DRIE) was presumed to be applied on the developed substrates to construct high aspect ratio wells as moulds for casting polymers.

### **Casting with natural leaves**

Leaves from two different plants, *Dicliptera Suberecta* and Lady's Mantle, were used here as the main positive molds. The elastomer PDMS (polydimethyl siloxane, Sylgard-184, Dow Corning corp.) mixed with curing agent (10:1 ratio) was poured onto the leaves. In order to avoid a quick dehydration of the leaves, the cast elastomer was room-temperature cured for at least 24 hours. The leaves were gently peeled off from elastomer leaving it as negative mould for a subsequent casting. (Figure 3-3) Before casting the second layer of elastomer, the moulds were treated with HMDS (Hexamethyl-disilazane,  $[(\text{CH}_3)_3\text{Si}]_2\text{NH}$ , Dow Corning) vapor as a demoulding agent in the desiccators for 10 minutes. The second layer of elastomer was then poured on the negative moulds and cured at 80°C for 2 hours.

### **Casting with commercial porous membrane**

**Membranes** Two types of membranes (Figure 3-2) were used as here:

- (1) Anodic alumina membrane (Anopore®, Whatman), pore size: 0.2 $\mu\text{m}$

- (2) Track-etched polycarbonate membrane (ISOPORE™, Millipore Inc), pore size= 0.6, 1.2 and 3.0 μm

**Materials of substrates** Thermosoftening plastics were used as major substrate materials for membrane casting. Table 3-1 summaries the specification of the substrates used in this study. The PS (polystyrene) and PMMA (Polymethyl methacrylate) films were prepared by drying polymer solutions in which PS and PMMA granules were dissolved (at 15 wt%) in toluene and tetrahydrofuran (THF), respectively.

**Procedure of membrane casting** The liquid silicone elastomer and the curing agent were mixed at 10:1 ratio and degassed to prevent the formation of air bubbles. The degassed silicone elastomer was then spun on a silicon substrate to form a uniform film where a PC or alumina membrane was placed over the coated film afterwards. After curing the film at 80°C for 2 hours, the alumina membrane was then removed by dissolving it in 45% KOH solution for 10 minutes while the PC membrane was dissolved in dichloromethane (CH<sub>2</sub>Cl<sub>2</sub>) for 5 minutes.

For other thermoplastic polymers, the plastic sheets were cut into 1.5 cm square and then sonicated in acetone and DI water for 5 minutes. After dried in air, the substrate and a membrane were placed between two glass slides, where binder clips were applied to hold the pieces together. The casting process was then held by putting the sample set in a vacuum oven (vacuum pressure < 1 kPa, VO914A, Lindberg/Blue M co.) at a certain temperature for 10 minutes. The membranes were dissolved in proper solvents as previously described. The PC membrane can be simply peeled off by finger nails from the substrate. Figures 3-5 and 3-6 show the general procedure of membrane casting for elastomer and thermoplastics.

## **Characterization of surface morphology**

The surface morphology was mainly characterized by scanning electron microscope with the electron beam from conventional tungsten filament (SEM JSM-6400, JEOL co.) or cold field-emission (JEOL-6335F, JEOL co.). All of the cast samples were coated with a thin layer of Au-Pd (thickness ~30 nm) to improve the conductivity prior to the examination, while for samples of natural species (leaves and striders), no conductive coating was deposited in order to reduce the dehydration during the coating process. The accelerating voltage for observing cast samples was at 10-15 KV, and for natural species the value was lowered to 5-10 KV to ease the surface discharging issue.

## **Characterization of thermal properties**

The thermal properties of the thermoplastic substrates were measured by differential scanning calorimetry (DSC Q1000, TA Instruments Inc.) in the Chemistry Department at University of Florida. Materials at around 10 mg were placed in the hermetic alumina pans with lids. The heating profile was carried out as follows: the sample was first cooled down from room temperature to  $-50^{\circ}\text{C}$  and steadily heated to  $200^{\circ}\text{C}$  at a rate of  $10^{\circ}\text{C}$  per minute. After holding temperature for 5 minutes, the sample was immediately quenched to  $-50^{\circ}\text{C}$  and again heated to  $200^{\circ}\text{C}$  at the same ramp. The glass transition temperature ( $T_g$ ) of samples was determined as the middle point between the two intersection points by the three tangent lines on temperature transition slope. (Figure 3-7) The curve was analyzed by the software controlling DSC, from which the point of  $T_g$  was also given. The melting point,  $T_m$ , is determined by the temperature at the maximum in the ( $dH/dT$ ) plot near the transition. The onset of melting is taken as the initial rise of the curve above baseline. The maximum melting temperature at this

heating rate is taken as the final point which deviates from the baseline. All the analyses were conducted at a heating rate of 10°C/min.

### **Characterization of mechanical properties**

The mechanical strength of the substrates was measured by Instron tensile tester (Instron 1122, MTS System Co.) at Dr. Anthony Brennan's lab in University of Florida. The test was performed at room temperature with the smallest 22 *lb* load cell. Specimens in dog-bone shape (Figure 3-8) were first cut from plastic sheets by using a standard cutting die, and then clamped onto the load cell. The tensile test protocol followed the standards ASTM D638.<sup>59</sup> The tensile test was performed at the speed at 1 inch/min where samples' elastic modulus, elongation and ultimate strength (Figure 3-9) are determined from the controlling program.

## **Experimental Results**

### **Making Hairy Surface via Self-Alignment of Carbon Nanotubes**

#### **Colloidal carbon nanotubes**

MWCNTs were functionalized by chemical oxidation in which carboxylic groups were generated on the surface of carbon nanotubes. Figure 3-10 shows the zeta-potential of functionalized and non-functionalized MWCNTs at various pH values. Functionalized MWCNTs have negative surface charge in different pH values with IEP (isoelectrical point) near pH=1 where IEP of non-functionalized MWCNTs was around pH=5.5 which makes non-functionalized MWCNTs unable to form a stable solution in water. Functionalized MWCNTs are well dispersed in water and ethanol without the assistance of surfactants. Carboxylic groups had a strong adhesion force with amine groups in deionized water (pH 6.5).<sup>60</sup> Some studies showed that carbon nanotubes can be aligned on substrates by electrical adsorption.<sup>61,62</sup> This was the main reaction to form

self-aligned MWCNTs on the substrate where the carboxylate anion groups of functionalized MWCNTs absorbed on the oppositely charged polycationic polymer, PDAC, by Coulombic attractions. (Figure 3-1)

After the immersion of PDAC-coated Si substrates in colloidal MWCNT suspensions for 18-24 hours, the substrates showed no visible change. The SEM image of 18hr-immersed Si substrate (Figure 3-11) shows a bare, flat surface where only few pillar-like structures were seen. Similar results were also discovered for those whose immersion time prolonged to 24 hours. The dimensions of these pillars (rods) were relatively large, with the diameter around several hundred nanometers and the length up to few micrometers, indicating these were CNT bangles, formed due to van der Waals attraction between carbon nanotubes. Although previous study conducted under the same procedure showed carbon nanotubes tended to be vertically absorbed onto substrate with the height of the layers ranges from 10 to 80 nm,<sup>63</sup> the current work shows that scanty CNTs were effectively absorbed onto the substrate coated with polycationic polymer.

## **Results and discussion**

Using vertically aligned carbon nanotube arrays to create superhydrophobic surfaces is not rare.<sup>12,64-66</sup> The carbon nanotube arrays, grown from chemical vapor deposition (CVD), create a rough surface where air can be trapped under these heterogeneous structures resulting in the Cassie-Baxter (CB) regime. The areal density of CNTs on the CVD-grown samples can be as high as  $10 \mu\text{m}^{-2}$ . Despite this density difference, the idea of using carbon nanotubes may conflict with the main objective at certain points. First of all, the purpose of this study is to have a surface covered with

hair-like structures that allows us to study the wetting properties. The goal is to mimic the hairy integument of arthropods. The geometry of their hairs is all similar; they taper to a point from the cuticle with most tips curled towards their body, and the length is usually among several to tens of micrometers, sufficient to hold an air layer underneath the liquid.<sup>56</sup> The height of adsorption CNTs is tens of nanometers, which is much shorter than those hairs and may not be able to maintain the liquid interface in CB state. Moreover, the flexibility of hairs on arthropods may play an important role while contacting liquid, although this is not fully understood.<sup>17,56</sup> The hair tends to buckle under Laplace pressure, which, in turn, eases the fluid impregnation. Nevertheless, the CNTs are considered the stiffest material yet discovered, as Young's modulus can be up to 1 TPa, which makes it impossible for them to have deflection while interacting with a liquid interface.<sup>67</sup> Last, but not least, the CVD-grown CNT arrays are not intrinsically superhydrophobic; they usually require a coating with a low surface tension chemical compound (i.e. polytetrafluoroethylene, PTFE).<sup>12,64-66</sup> This indicates that the surface chemistry here dominates more on liquid repellency. This also shows that the functionalized CNTs of the current study will need an extra modification since the surface carboxylic groups makes CNTs more hydrophilic, even if they were to be attached on the substrate. Overall, this technique originally intended to align CNTs vertically on the surface through a direct, simple self-assembly process, but due to low adsorption of CNTs and other inherent issues, the experiment could not use this technique as the main fabrication method.

## **Making Hairy Surfaces via Moulding Technique**

### **Casting with lithographed moulds**

Lithography is by far the most successful technology in micro-fabrication area, and has been used in semiconductor industry since the late of 50s.<sup>68</sup> Typically, an irradiation source and a photosensitive polymer material are used to perform the pattern transfer. It is referred as a top-down approach where a pattern is transferred onto a substrate and followed by an etching process to construct the surface features. Figure 3-12a shows an SEM image of the surface of a cast elastomer. The height of the surface structure was around 10  $\mu\text{m}$  with the edge length of 10  $\mu\text{m}$  showing the geometry was able to be precisely duplicated from the moulds. One of the great advantages of this technique is that the lateral structure can be well defined via pre-designed patterns from a photomask, while this may also restricts the freedom of having different dimensions. More sophisticated equipment as well as the operation skill is usually required here.

Electron-beam (E-beam) lithography is considered as a maskless lithography to create a very small structure, submicron to nanometer range, on an electron-sensitive resist coated surface. The pattern can be designed by CAD software, and then transferred it to the pattern-writing system. This makes e-beam lithography a great tool in nanofabrication for research and development purpose. Figure 3-12b shows a dot array of 1  $\mu\text{m}$  in diameter and 1  $\mu\text{m}$  in spacing created by e-beam lithography. The deep reactive ion etching (DRIE) was planned to be applied to create high-aspect-ratio wells as a mould for casting polymers. The major limitation of e-beam lithography is throughput: an extremely long exposure time is required for making a larger area sample. Taking current experimental parameters, the minimum time (t) required to make

an array shown in Figure 3-6 on a 1×1 square inch substrate can be estimated by the following formula:

$$\text{Dose} \times \text{Exposed area} = \text{Beam current} \times \text{Exposed time}$$

$$600 \text{ (mC/cm}^2\text{)} \times 1.61 \text{ (cm}^2\text{)} = 0.4 \text{ (pA)} \times t$$

$$t = 1.9 \times 10^6 \text{ sec} \approx 22 \text{ days}$$

It will require 22 days to finish writing this dot array, and this does not include time for the stage to move and possible time for beam corrections or adjustments. This is apparently not a practicable method for making a mould for casting hairy structure surfaces.

### **Casting with natural leaves**

The surface features from natural species provided an alternate source of moulds. Using species, such as water striders, as master moulds for duplicating the hairy structure has been reported. Only samples, however, with small area (few square millimeters) could effectively be prepared so far, which makes the subsequent characterization very challenging.<sup>22</sup> Therefore the current work started with hairy leaves as moulds so that it may provide an acceptable sample size, and, more importantly, to avoid the involvement of living creatures.

Figure 3-13a shows the surface structure of a *Dicliptera Suberecta*'s leaf where its hairs (trichomes) are around 50 $\mu$ m wide with the height up to several hundred micrometers. Rugged trichomes along with lower packing density made *Dicliptera Suberecta*'s leaves a proper mould. The cast elastomer is shown in Figure 3-14a and b where the hairy structure was able to be duplicated from *Dicliptera Suberecta*. On the other hand, Lady's Mantle was severely dehydrated after curing at oven for two hours

(Figure 3-15), which made the leaf vulnerably brittle. In addition, Lady's Mantle has trichomes with a diameter much smaller ( $\sim 1 \mu\text{m}$ ) and at a much higher areal density leading lady's mental unable to be a negative mould, since most of the trichomes remained inside the elastomer while being peeled off from the leaves (Figure 3-16a). Figure 3-16b shows the pore density was significantly lower ( $1.6 \times 10^3 \text{ cm}^{-2}$  vs  $6.5 \times 10^3 \text{ cm}^{-2}$ ) than the negative mould. Smaller pore size also inhibits the elastomer from filling up the entire pores with only capillary action. All these make direct leaf casting an impractical way of making hairy structure. The wetting property is mainly studied on the leaf itself, rather than cast surface, and is presented in Chapter 4.

### **Making Hairy Surfaces via Moulding with Commercial Membranes**

#### **Membrane casting on elastomer**

Two commercial membranes, anodic alumina (AAO) and track-etched polycarbonate (PC), were applied as moulds for casting. Both membranes provide uniform, disconnected pores which are appropriate for creating the surface patterns by filling the pores. Membranes were first placed onto the silicone elastomer coated substrates, and then dissolved by proper solvents. Figure 3-17 shows the surface of silicone elastomer after immersing into dichloromethane. The elastomer was not able to fill the pores ( $\phi = 0.6 \mu\text{m}$ ), and the surface was roughened after dissolving PC membrane. Similar results were found for using AAO membrane ( $\phi = 0.2 \mu\text{m}$ ), while the substrate remained smooth after etching process. Wetting difference between the elastomer and the membrane is the important factor that hinders the elastomer to flow into the pores. The silicone elastomer is considered as hydrophobic ( $\theta_c \sim 97^\circ$ ), while PC and AAO membranes are more hydrophilic ( $\theta_c \sim 80^\circ$  and  $\sim 40^\circ$  for PC and AAO,

respectively). An external assistance, rather than just by capillary action, is required to force the viscous elastomer to wet the membranes and fill the pores.

Alternatively, the elastomer was poured onto the PC membranes ( $\phi = 0.6, 1.2,$  and  $3.0 \mu\text{m}$ ), and then cured in a vacuum oven. The membranes were peeled off after the curing process. Figure 3-18a to c show the elastomer surface cast with different pore size membranes. The surface feature becomes appreciable with the increase of the pore size, protruding from tiny spots ( $\phi = 0.6 \mu\text{m}$ ) to posts ( $\phi = 3.0 \mu\text{m}$ ). The height of the protruding posts is around  $10 \mu\text{m}$ , and they were more randomly oriented on the surface rather than vertically standing.

The use of silicone elastomer on the fabrication of surface microstructure has become widespread in the past decade. It is usually attributed to its chemical stability, non-toxicity and a wide range of working temperature. Moreover, the surface is easy to functionalize by silane-based chemicals rendering surface hydrophobic or hydrophilic. The silicone elastomer is considered to have a relatively low stiffness (with Young's modulus below  $1\text{MPa}$ )<sup>69,70</sup> making the stability of the patterned structures as one of the main concerns, especially the one with high aspect ratio where buckling and collapse of the structures may occur. Depending on the geometrical shape, diameter and the elasticity, the critical aspect ratio is usually under  $10$ .<sup>69</sup> This makes silicone elastomer not to be a suitable material for the preparation of high aspect ratio hair-like structure.

### **Membrane casting on thermoplastic polymers**

Thermoplastic is a polymer that can be melted to a liquid when heated and frozen to a solid, glass-like state when cooled. The process is reversible, which makes thermoplastic recyclable. This also allows their surfaces to be easily embossed with a

particular pattern, since they can be remelted and remoulded to create surface features. The ultimate goal is always aiming to develop a method that not only makes hairy structures, but is also cost-effective and time-efficient, so more effort can be devoted to the wetting study. The previous result on silicone elastomer denoted a promising way of creating surface pillars via membrane casting. Therefore, I applied a similar procedure to common thermoplastics so it could be easily assessed on a daily basis.

### **Polypropylene (PP)**

Polypropylene (PP) is a commercially available polymer and is used widely in a variety of applications due to its fair mechanical strength and superior resistance to many solvents.<sup>71</sup> The PP substrate in the experiment was a general file jacket (No. 85781, SMEAD co.) purchased directly from Office Depot. The DSC analysis showed it had a melting temperature of 165°C (Figure 3-26). The casting process was performed in a vacuum oven where PP substrates and membranes were pressurized together between two glass slides, as described in the first section.

The PP substrate was cast with an AAO membrane ( $\phi = 0.2 \mu\text{m}$ ) at 190°C for 10 minutes; the AAO was then dissolved in KOH. Figure 3-19 shows the surface morphology after dissolving the membrane. The protruded structure formed a grass-like surface where hundreds of submicron-sized vertical fibers clumped together and curled randomly. The diameter of the fibers was in good agreement with the pore size, but due to the high pore density ( $10^8$ - $10^9 \text{ cm}^{-2}$ ) the mean distance between pores was only ~50 nm, resulting in clumps of fibers rather than individual strands (Figure 3-19c).

The substrate was also cast with polycarbonate (PC) membranes ( $\phi = 0.6, 1.2$  and  $3.0 \mu\text{m}$ ). After the membrane was dissolved in dichloromethane, the microstructure

of the cast surface was shown in Figure 3-20. For 3.0 and 1.2 $\mu\text{m}$ -cast surfaces (Figures 3-19a and b), the protruded structure formed cylindrical posts with an average height of around 20  $\mu\text{m}$ . The smooth base also indicated that the PP substrate did not react with the solvent. The pore of the PC membrane was made by the irradiation of high energy particles, so, unlike the AAO membrane, the pore distribution on the PC membrane was disordered and not all perpendicular to the surface (Figure 3-4a). This made the cast structure randomly distributed with some of them inclined towards the surface (Figure 3-20a). The surface cast with the 0.6  $\mu\text{m}$  membrane (Figure 3-20c) showed height variation at the posts, and some of the taller ones clumped together on the upper region. Close examination of top-viewed pictures (Figure 3-21) revealed that the structure formed hollow cylinders as the diameter became smaller. The posts almost formed tube structures for the 0.6 $\mu\text{m}$ -cast surface (Figure 3-21c), although it was difficult to estimate the depth of the tube (or the height of the filled portion). More casting time is needed to fill up the pores with a higher aspect ratio. This is not a rare occurrence in the moulding process, as people use this casting technique to make nanotubes out of various materials.<sup>72,73</sup>

The PC membrane could also be mechanically removed by simply peeling the membrane off from the substrate. The morphology of the peeled-off structure heavily depended on the pore size, shown in Figure 3-22. The posts on the 3.0 $\mu\text{m}$ -cast surfaces were somewhat stretched, with the tips angled towards the direction in which they were peeled. The structures on the 1.2 $\mu\text{m}$ -cast surfaces were much more disordered, where some of the posts were significantly elongated and randomly curled up to over 50  $\mu\text{m}$ . As for the 0.6 $\mu\text{m}$ -cast surface, the surface structure was completely

different from the membrane-dissolved surface. After the peeling, the density of the remaining structure was about  $7 \times 10^5 \text{ cm}^{-2}$ , almost two orders of magnitude lower than the membrane ( $\sim 4 \times 10^7 \text{ cm}^{-2}$ ); this indicated that most of the posts were ripped off during the peeling process. The structure of the  $0.6 \mu\text{m}$ -peeled surface featured a very unique geometry; it had a low areal packing density and curled structures with various lengths and seemed to be randomly oriented. Their configuration appeared to be a *de facto* hair structure, similar to those in the natural biological system. More detail is presented in the section of general discussion.

### **Low-Density Polyethylene (LDPE)**

The casting-peeling process was applied on other thermoplastics to create the hair-like surface structure. LDPE is one of the most widely-used thermoplastics for making containers, wrapping films, and, the most common, plastic bags. Compared to PP, the LDPE substrate was softer, and had a lower melting temperature at  $109^\circ\text{C}$  (Figure 3-27). The LDPE substrate was cast with a PC membrane at  $140^\circ\text{C}$  for about 6 to 8 minutes, and the membrane was removed afterward by the peeling process only. The surfaces of the cast LDPE turned from translucent into opaque. The force needed to peel the membrane off from the LDPE substrate was less than that from the PP substrate. The SEM pictures in Figure 3-23 show that after the peeling process, the pore-filled structures were greatly stretched to several hundred micrometers all over the surface, much longer than the PP cast. The prolonged fibers were randomly oriented and entangled with one another, making the surface morphology more like a fiber mat. With the decrease in diameter, the fiber length was elongated more, but the overall surface structure remained similar.

## Polyvinylidene Fluoride (PVDF)

PVDF is from the fluoropolymer family and has a relatively lower melting point. The one used in the experiment had a melting point of around 168°C (Figure 3-28). PVDF is commonly used in insulation, tubing, or high-valued paint due to its flexibility, light weight, and resistance to chemicals.<sup>74</sup> Following the same casting process, the PVDF substrate was cast at 190°C with a PC membrane and then peeled off. More force was generally needed for peeling the membrane off from the PVDF substrate. The microstructure of the cast PVDF surface was shown in Figure 3-24. For the 3.0µm-cast surface, samples with adequate area were not able to be obtained, as the membrane was strongly stuck to the substrate. Only a very small portion of the membrane, mostly around the sample edge, could be peeled. Its peeled-off structure (Figures 3-24a and b), however, was very different from the LDPE or PP substrates. The diameters of the posts were not tapered towards the tip as those in the PP substrate. Instead, the heads became slightly larger than the body of the posts, making their shape similar to tulip. This may be attributed to the neck forming while the posts were being pulled. Although the contact angle measurement was not able to be performed on the small sample area, this particular structure may have an appealing property on adhesion. Their shape appeared to be like the setae of a gecko foot, which had more contact area and Van der Waal interaction with the surface than the fibers should have.<sup>75</sup>

The structure of the 1.2µm-cast surface was similar but more curled with a thinner fiber diameter (Figure 3-24d). For the 0.6µm-cast surfaces, the posts were generally stretched into fibers but with a much shorter length than the LDPE. The fiber curled

randomly and a large portion of them were ripped off during the peeling process (Figure 3-24f).

### **Other Thermoplastics**

The casting was also tried on a few other common thermoplastics to exam the possibility of making hairy features. Polyethylene terephthalate (PET) was cast at 230°C (due to the limit of the vacuum oven and PC membranes), and the film showed no sign of casting (the surface remained transparent and glossy after removing the membrane). Polystyrene (PS) and polymethyl methacrylate (PMMA) films were prepared by dissolving the granules in proper solvents and then air drying them. The PS film was later cast at 200°C while the PMMA was cast at a lower temperature, 160°C; membranes were peeled off for both substrates. As shown in Figures 3-25a and c, when cast with a 0.6µm membrane, both substrates had small bulges, rather than posts, stuck on the surface. For the 3.0µm-cast surface (Figures 3-25b and d), the structure became more obvious, although the height was still much shorter when compared with the other thermoplastics.

### **Issues of the current membrane casting**

#### **Substrate Materials**

During moulding, the polymeric substrates were partially melted or softened and then pressurized into the pores. This filling process was usually slow since the polymers needed to flow long distances to fill up the cavities and, more importantly, because the polymers had a high viscosity. This was a consequence of the filling mechanism driven by the wetting properties of the polymer/mould system.<sup>73</sup> In this work, high aspect ratio surface structures were successfully made on several thermoplastic materials, including

PP, LDPE and PVDF, although not all of them showed a vertical, pillar-form structure. These materials had distinct melting points (Figures 3-26 to 28), and the processing temperatures were set higher than their melting points (Table 3-2).

For semi-crystalline polymers, the viscosity greatly dropped if the temperature was above the melting point.<sup>76</sup> The casting could therefore be effectively achieved within a few minutes at this elevated temperature, and the vacuum could also facilitate the filling process. On the other hand, amorphous substrates, like PS and PMMA, hardly exhibited a sign of filling the pores even though the temperature was raised above the glass transition temperature to almost 80°C. The viscosity was not low enough for the materials to flow into the pores. More importantly, the hair structure was greatly affected by plastic deformation while peeling off the membrane at ambient temperature. Table 3-3 summarizes the mechanical properties of the substrate materials used for making hairy structure. This plastic deformation, however, was not available for PS or PMMA as the ambient temperature was below 80% of their glass temperatures ( $T_g$ ) making them brittle and likely to fracture.<sup>76</sup> The pore-filled structure would be easily broken during the peeling process. Tensile tests on the PS and PMMA substrates could not be performed since the substrates were too brittle to be cut into dog-bone shaped specimens with the standard cutting die.

### **Restrictions**

The two types of commercial membranes used as moulds for casting, polycarbonate and anodic alumina, greatly reduced the time and complexity for the sample preparation. However, they also limited the control of the experiments, such as pore density, distribution, and thickness, especially for the PC membrane whose pores were

not only randomly distributed, but occasionally intersected with others. The range of the casting temperature was also restricted by the membrane. PC membranes, for example, were suggested by the manufacturer to be used below 200°C. The peeling process of the membrane prevented the ceramic AAO membrane from even being considered. Therefore it was quite challenging to test polymers with temperatures above 200°C, which included most of the thermoplastics in the fluorocarbon family,<sup>77</sup> whose low surface energy may have been more preferable for creating a *super*-hydrophobic or -oleophobic surface.

The majority of the membranes were removed by a direct peeling process without tools, but with fingernails. This was a very quick, effective, and zero-cost process of removing the moulds. Some PC moulds could even be reused for another casting, although all the PC membranes curled severely into rolls after being peeled. As mentioned above, peeling at ambient temperatures hindered the use of thermoplastics whose  $T_g$  were above room temperature. Additionally, it was very difficult to keep the process under a consistent condition, such as the speed and force of peeling. This may have had a great impact on the thermoplastic substrates, as the mechanical properties of polymers are strongly related to the strain rate. The main goal of this study was not to reveal the detailed parameters of the process, but to seek a feasible way of making the hairy structure. Therefore, the whole process was performed as consistently as possible throughout the entire fabrication. The later characterization was performed and discussed based on the surfaces created.

## General Discussion

### The Artificial Hairy Surfaces

The surface structure varied with the thermoplastics after peeling the membrane. Pillars on the PP substrate easily formed hollow structures (tubes), especially with narrow-pore membranes, due to its low surface tension and the ability to wet well.<sup>71</sup> These tubes were not able to mechanically withstand the peeling force, and therefore the majority of them were ripped off with the membrane. The LDPE substrate had the lowest yield strength and could be stretched to several times the original under a limited pulling force; this made the LDPE surface turn into a fiber-mat covered structure. PVDF, however, had the highest mechanical strength, and the pillars were not significantly stretched, with most of them still remaining on the surface after being peeled off the membrane. Among these surfaces, the membrane-peeled ( $\phi=0.6\mu\text{m}$ ) structure on the PP substrate specifically proved to be of importance.

As shown previously in Figure 3-22f, the density of the remaining structure on this particular surface was almost two orders of magnitude lower than the membrane. These remaining pillars were curled at various lengths and were to be oriented in a certain direction. A close-up image in Figure 3-32a revealed that the peeled structure of an individual post was similar to natural hairs. They tapered to a point from a base with a pore-size diameter while the length varied from less than a micron to about 10 microns. Longer hairs were tilted around  $30^\circ$  to  $45^\circ$  with their tips curled. Some hairs were also curled towards or parallel to the substrate. Interestingly, this kind of arrangement happens to be easily found in many arthropods that have the capability of water-walking or underwater breathing.<sup>17,18,56</sup> Figure 3-28c shows the microstructure of a water

strider's integument, where two different sets of hairs are easily seen. The longer and shorter hairs on their abdomen are around 30  $\mu\text{m}$  and 5  $\mu\text{m}$  long, respectively. Longer hairs are inclined at a 30° angle with the tips roughly towards or parallel to the body surface. Shorter hairs are usually thinner (diameter~ 500 nm) and more randomly oriented. The densities of longer and shorter hairs are  $\sim 5 \times 10^5 \text{ cm}^{-2}$  and  $\sim 8 \times 10^7 \text{ cm}^{-2}$ , respectively. While the density varies along the body and species, the overall geometry is similar to the PP cast surface. This particular structure enables the certain species to maintain and control the air-water interface adjacent to their skin, which is vital to them for daily activity. For example, Figure 2-8b shows a thin layer of air trapped by a submerged fisher spider, enabling the spider to constantly perform respiration under water. Similar air-trapping behaviors are also found on the artificial hairy surface as shown in Figure 3-33b. Moreover, the artificial hairy surfaces showed superior water repellency; water drops dripped on the surface immediately bounced back and then rolled off the surface effortlessly. Their hydrophobicity, along with other cast structures, is studied in the following chapter.

### **The Scope of the Casting Process**

One of the main objectives in this work was to obtain an effective method to make a surface covered with hair-like structures. A great challenge was to make a surface feature with such a high aspect ratio ( $>10$ ) with the diameter just a micrometer, not to mention that the ratio could also be in the hundreds for some natural hairs. Although high aspect ratio vertical posts or fibers, such as carbon nanotube forests,<sup>64</sup> ZnO,<sup>78</sup> or BN<sup>83</sup> nanofibers, have been well prepared via vapor phase condensation, it was not adopted here due to their complexity. Direct machining or the top-down route was also

not considered as a main approach. Despite the aspect ratio, as mentioned before, the shape and the conformation of the hairs needed to be arranged in a certain way.

Therefore, even though there are plentiful works on mimicking natural superhydrophobic surfaces, reports specifically aimed at creating the structure of hairs are still very limited. All of the previous studies duplicated the hair structure from living species by a two-step moulding process, similar to leaf casting. The first report came out in 2005,<sup>22</sup> in which a leaf of Lady's Mantle served as the first mould. Another report duplicated the hairy surface from a strider's abdomen.<sup>23</sup> The hair structure was successfully duplicated from the master moulds. However, both of these works had the same defect, inadequate sample size, which resulted in difficulty for the characterization of wetting property.

The main manufacturing technique used in this research, moulding with commercial membranes, had been previously utilized for making arrays of pillars,<sup>80</sup> fibers,<sup>81</sup> and nanotubes,<sup>72</sup> was not a novel approach. The technique that specifically involved polypropylene and the PC membrane was largely reported in research mimicking the gecko foot,<sup>82-84</sup> in which an array of millions of high aspect ratio microfibers was created to imitate the gecko adhesive. Their strong adhesive and shear force are attributed to millions of micro-spatulae, which result in enormous Van der Waals interactions with the surface where the geckos' feet contact. The major difference between this work and previous research is the way of removing the membrane. The membranes are normally dissolved in a proper solvent, which is  $\text{CH}_2\text{Cl}_2$  for PC membrane, to preserve the high areal density of fibers. In my experiment, I simply peeled the membrane off. Because of the force of pulling the membrane away, most of the material extruded into the pores was removed. The remaining columns were

elongated and oriented with the peeling process, leaving the surface structure exactly as the microhairs discovered in many arthropods. This work turned out to be the first to create the hair structure on polymeric substrates with a feasible sample area.

Many methods have been proposed to render surfaces superhydrophobic, although very few of them have shown a promising way for large scale production. This current process is relatively simple and effective. It may be able to expand to the fabrication of large-area superhydrophobic surfaces, since the surface morphology is only physically modified; it requires neither chemical reactions nor multiple steps. With the proper facilities, superhydrophobic sheets scaled-up to several meters should be able to be prepared in a continuous process. A similar idea had been explored by Guo et al.<sup>85</sup> where a so-called “template rolling process” was employed to imprint nanopillars on polycarbonate substrates with a tubular porous anodic alumina template. The generated pattern significantly increased the contact angle from 85° to 141°, yet the contact angle hysteresis and sample size were reported.

### **Durability of the Cast Structure**

The casted surfaces are able to withstand the impact from fluid somewhat well, i.e. compressed air blowing or droplets striking. However, since this high aspect ratio structure was made by soft polymers, the mechanical strength of the structure is not robust. The hairy structure may be damaged if the surface is abraded by solid matter, and consequently loses their superhydrophobicity. Figure 3-34 shows the hair structure on PP and PVDF substrates were demolished after being rubbed by fingers. While the durability is a general challenge among all superhydrophobic surfaces, publications

which address this issue are rare.<sup>86,87</sup> Moreover, no such study has ever been carried out on superhydrophobic surfaces consisting of high-aspect-ratio structures.

### **Summary**

To fulfill the first task, seeking a practicable method of creating surfaces covered with hair-like structures, various possible methods were explored and presented. Two major techniques were employed: self-assembling and mould casting. Self-assembling was carried out by immersing polycationic-polymer coated substrates into colloidal carbon nanotubes. Neither the experimental results nor the fundamental aspects supported the possibility of forming a vertical, self-aligned surface structure. The effort then shifted to the moulding technique where different moulds and substrates were tested.

Making moulds out of lithography was complicated and extremely time-consuming. Using of natural species as master moulds was also very challenging with the increase of aspect ratio. Therefore commercial membranes were chosen as the main moulds. This, however, limited the control of the experimental parameters. High aspect ratio vertical structures were prepared by casting thermoplastics with commercial membranes. A hairy surface was successfully achieved on polypropylene substrates; after peeling off the PC membrane, the surface was covered with  $\Gamma$ -shaped structures analogous to the natural hairs on many arthropods. The experimental parameters were restricted by the membrane, oven, and demoulding techniques here. Additionally, the durability of the cast structure was another concern. Nevertheless, the current process of making hairy structures is straight-forward and relatively accessible, and it has the possibility to be scaled up for the production of large-area superhydrophobic surfaces.

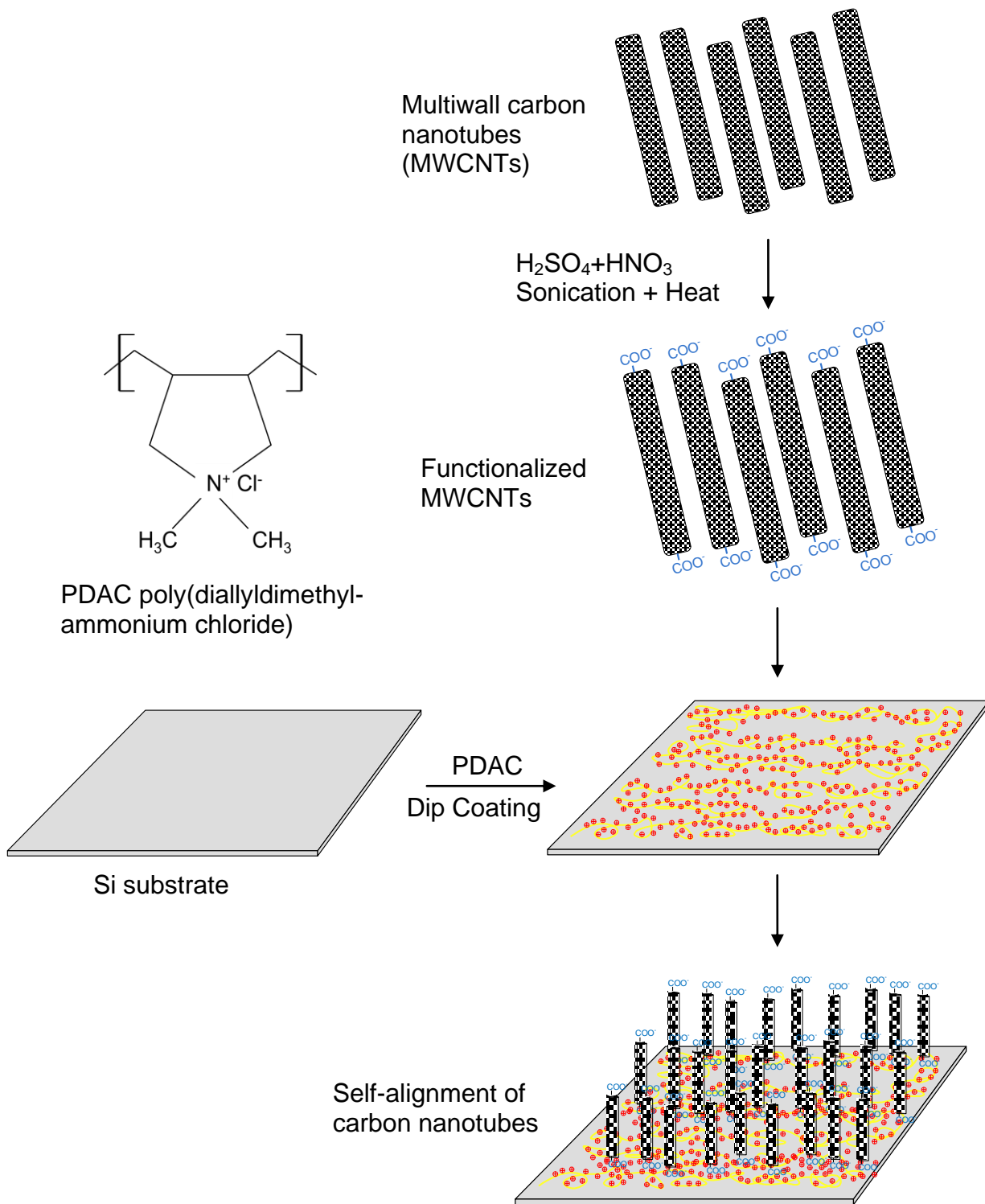
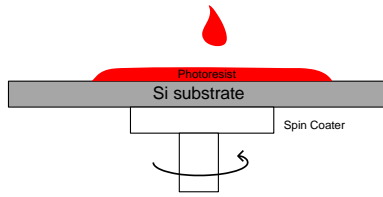


Figure 3-1. Schematic procedure of self-alignment of functionalized carbon nanotubes with polyelectrolytes.

**(1) Spin coating of the photoresist**



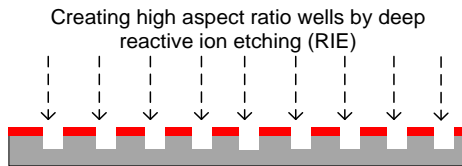
**(2) Exposure**



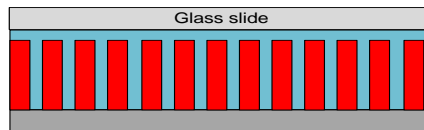
**(3) Development**



**(4) Etching**



**(5) Casting of elastomer**



**(6) Stripping of elastomer**

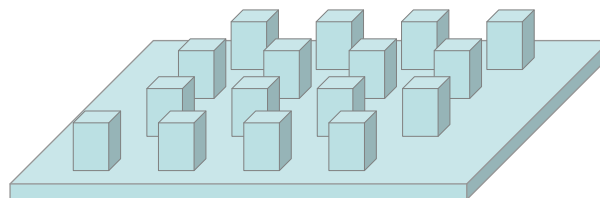


Figure 3-2. The procedure of high-aspect-ratio surface structure by photolithography and e-beam lithography.

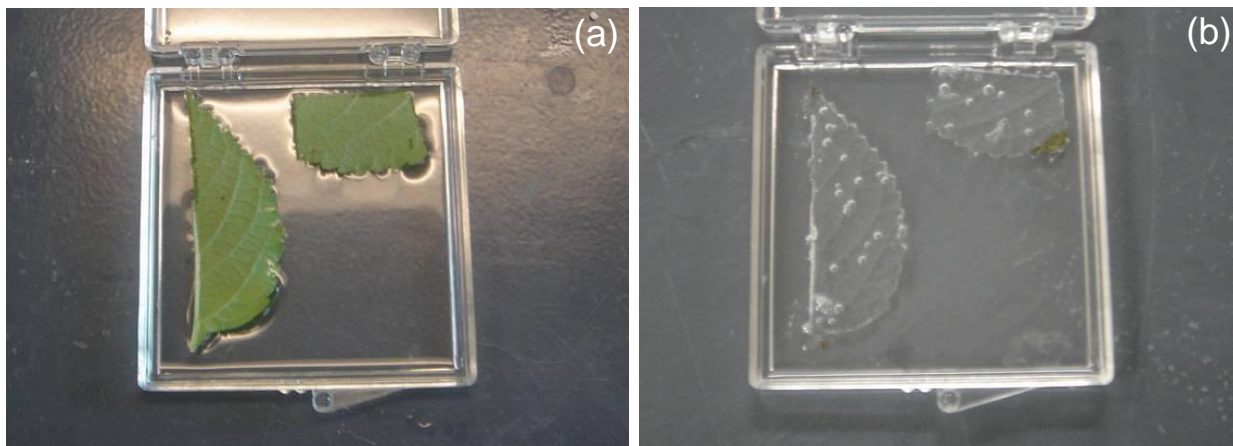


Figure 3-3. (a) Creating negative PDMS elastomer mould by using leaf *Diclptera Suberecta* as a positive mould, (b) Cured negative elastomer moulds after leaves were peeled off.

Table 3-1. List of materials for casting hairy surfaces in this study

Polymers	Approximate Thickness ( $\mu\text{m}$ )	Surface Tension ( $20^\circ\text{C}$ ) <sup>58</sup>		Sources
		( $\gamma_{LV}$ mN/m) <sup>a</sup>	( $\gamma_c$ mN/m) <sup>b</sup>	
Silicone Elastomer	-	21.3	21.7	Sylgard-184 Dow Corning corp.
PP (Polypropylene)	190	29.4	28.6	File jacket No. 85781, SMEAD co.
PVDF (Polyvinylidene fluoride)	760	-	23.2	Kynar <sup>®</sup> sheet Westlake Chemical Inc.
LDPE (Low-density polyethylene )	760	34.3	32.0	HIS-070335-G-01 Small Parts Inc.
PET (Polyethylene terephthalate)	150	-	46	PES-19900-F-01 Small Parts Inc.
PS (Polystyrene)	200	40.7	41.4	Lab prepared
PMMA (Polymethyl methacrylate)	200	41.1	35.9	Lab prepared

a. Liquid surface tensions  $\gamma_{LV}$  of solid polymers are from extrapolation from higher temperature studies of polymer melts.

b. Zisman critical surface tension  $\gamma_c$  is obtained from contact angle measurement with series of liquids of surface tension.

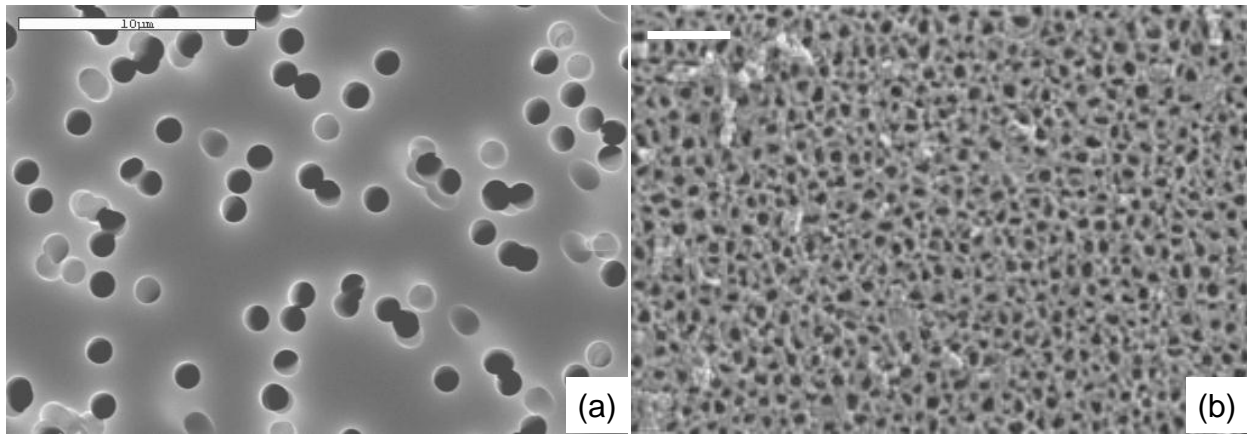
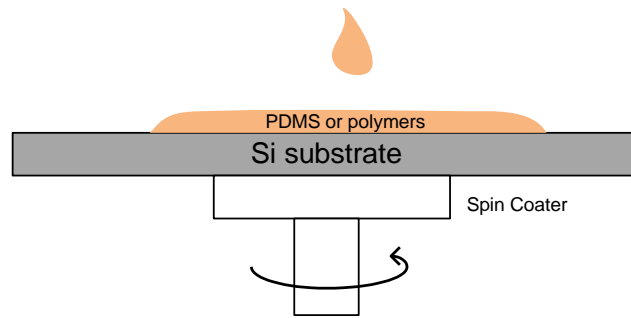
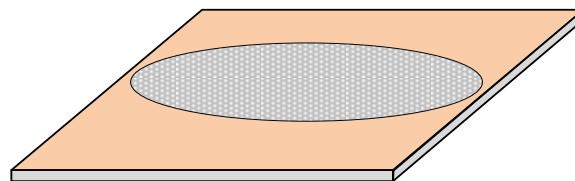
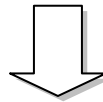


Figure 3-4. Two commercial membranes used for casting here (a) Track-etched polycarbonate membranes. (b) Anodic alumina membrane, the bar is  $1\mu m$ .

**(1) Deposition of elastomer**



**(2) Placing of the membranes**



**(3) Dissolving of the membranes**

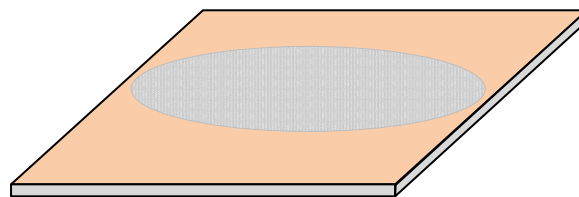
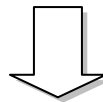


Figure 3-5. The procedure of casting PDMS elastomer with polycarbonate and alumina membranes.

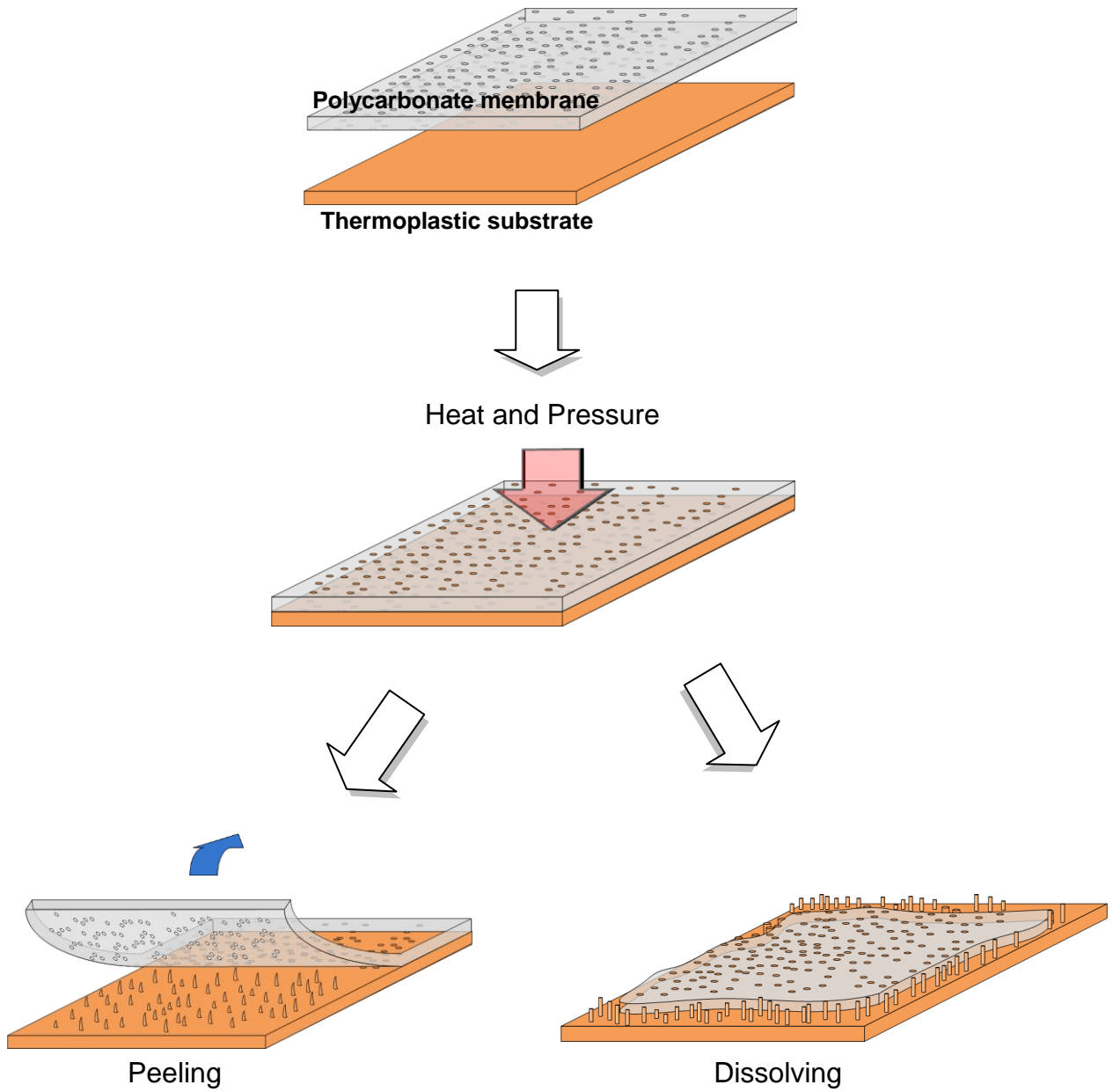


Figure 3-6. The procedure of casting thermoplastics substrate with polycarbonate membrane. The membrane is removed by either direct peeling or dissolving.

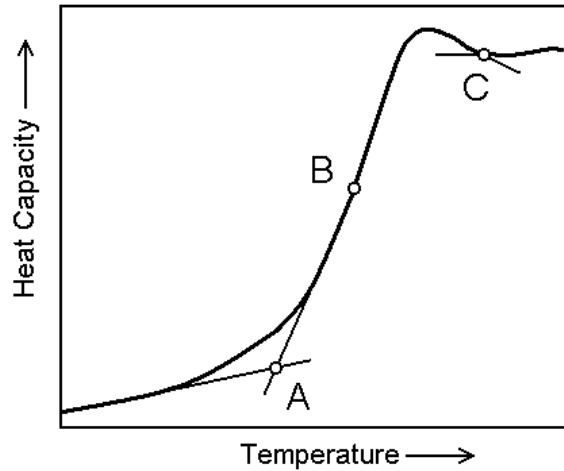


Figure 3-7.  $T_g$  is determined by the midterm point B from curve obtained by DSC analysis.

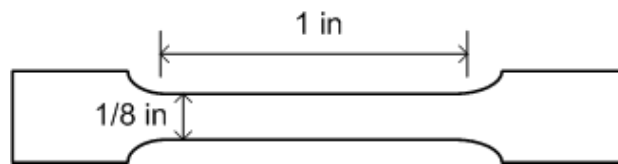


Figure 3-8. Standard dog-bone shaped samples for ultimate tensile test.

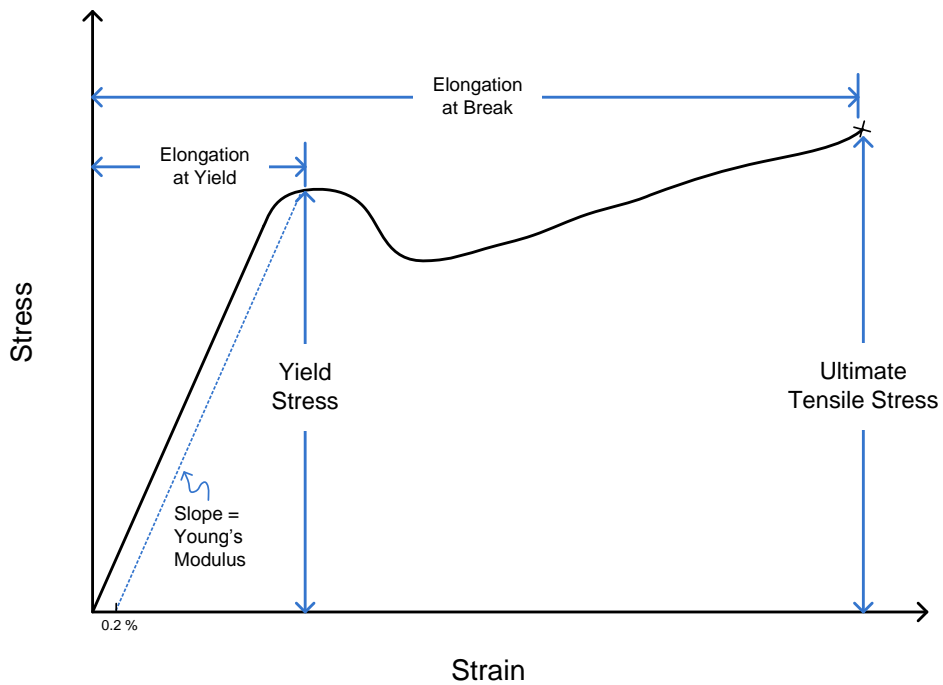


Figure 3-9. A typical tensile stress-strain curve and the represented properties for polymeric materials.

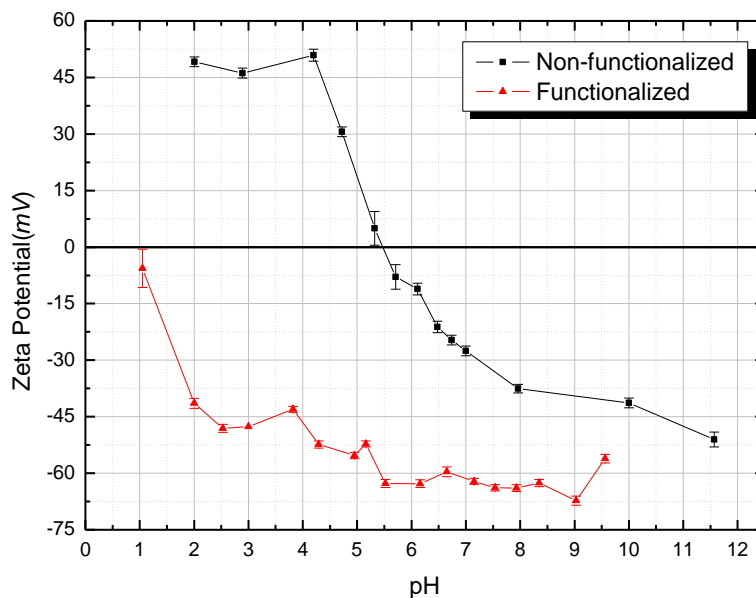


Figure 3-10. Zeta-potential of functionalized and non-functionalized carbon nanotubes showing the shift of the IEP (isoelectrical point).

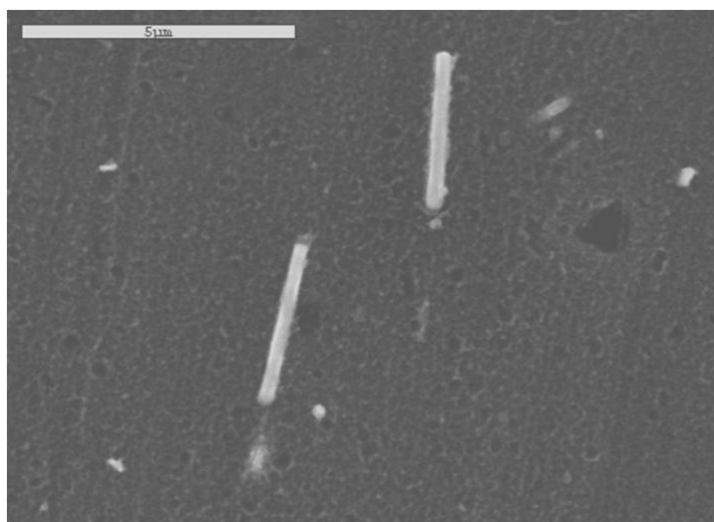


Figure 3-11. SEM picture of Si substrate after immersed into colloidal CNTs suspension for 18 hours. Two possible CNT bundles can be seen on the surface.

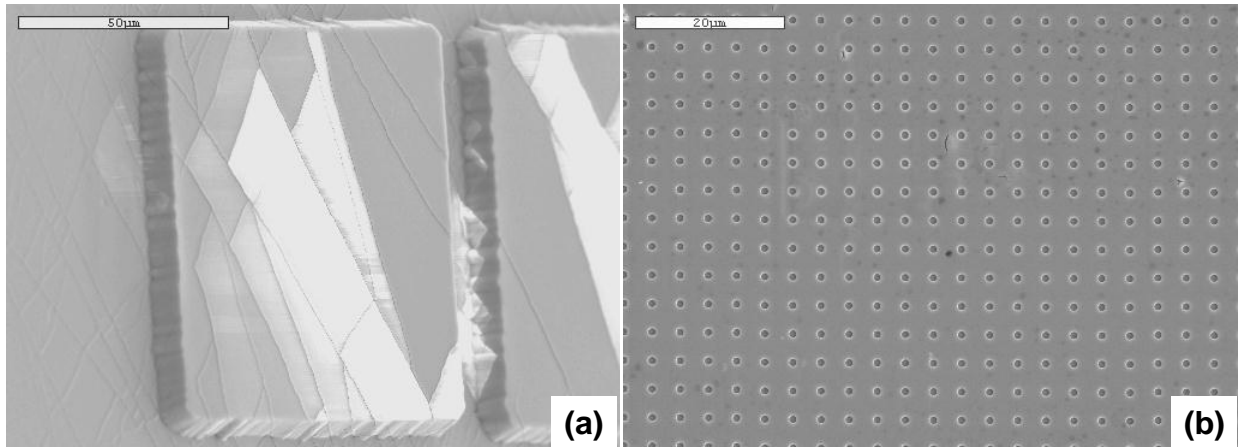


Figure 3-12. (a) The surface structure of cast PDMS elastomer from moulds developed by photolithography, (b) dot array created by electron beam lithography on PMMA electron-sensitive resist.

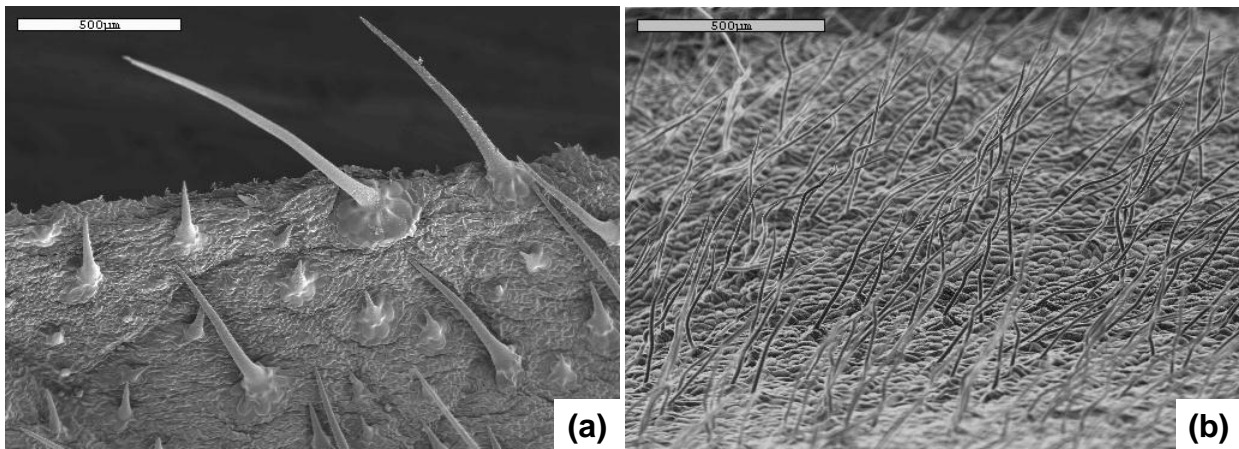


Figure 3-13. SEM pictures showed the structures of hairs (trichomes) of two different leaves. (a) Dicliptera Suberecta and (b) Lady's Mantle.

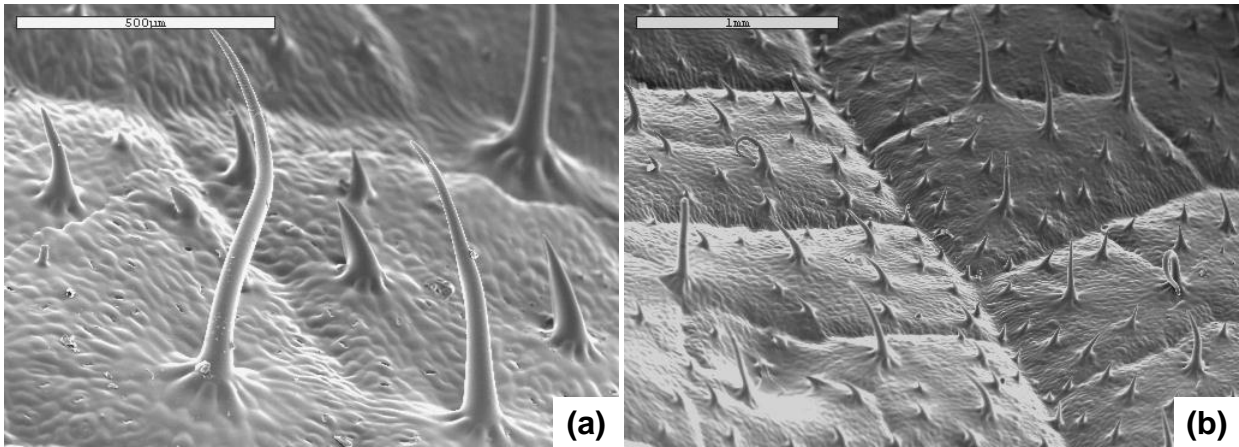


Figure 3-14. (a) The surface morphology of cast PDMS elastomer by using *Dicliptera Suberecta* as master moulds, (b) a close-up view.

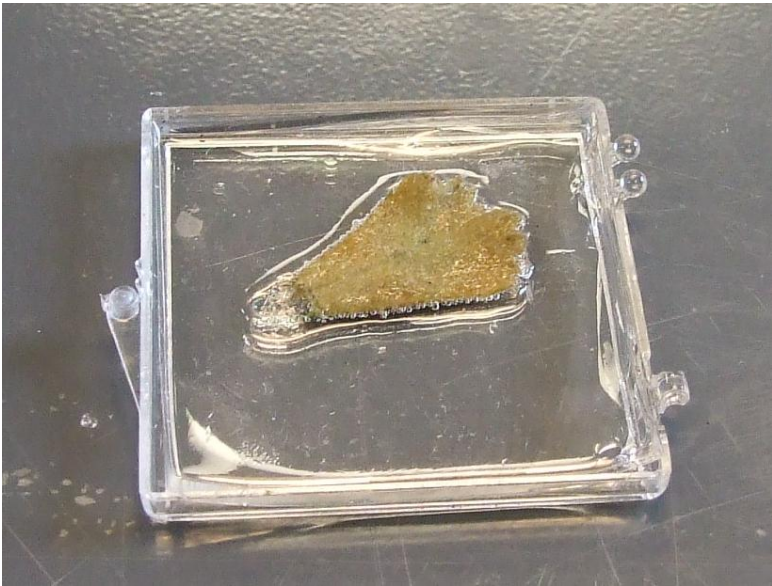


Figure 3-15. Lady's Mantle was dehydrated after curing process making it very difficult to be removed from the PDMS elastomer.

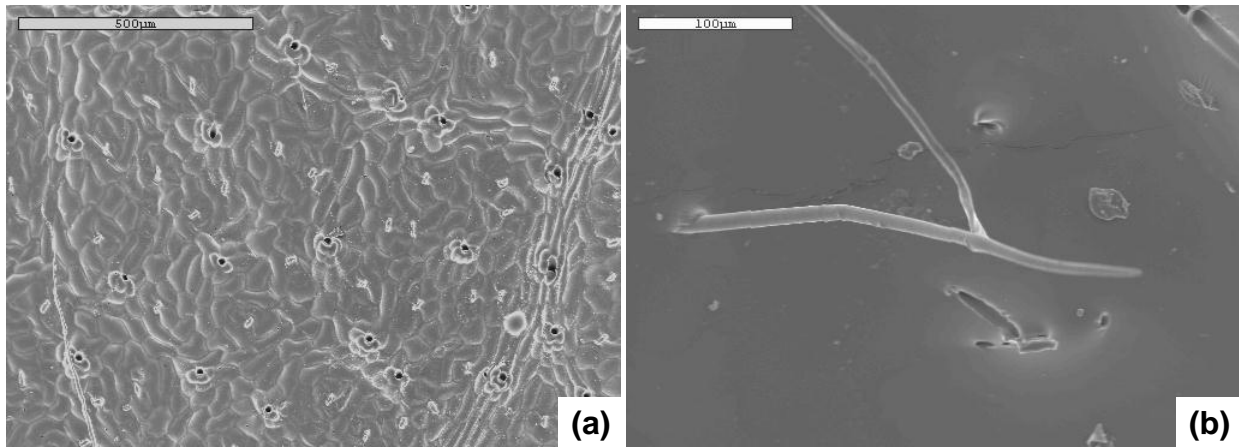


Figure 3-16. (a) A negative PDMS mould after peeling off the leaf of Lady's Mantle, where the packing density of pores were significant lower than the original hair density, (b) leaf hairs were ripped off and remained inside the PDMS moulds.

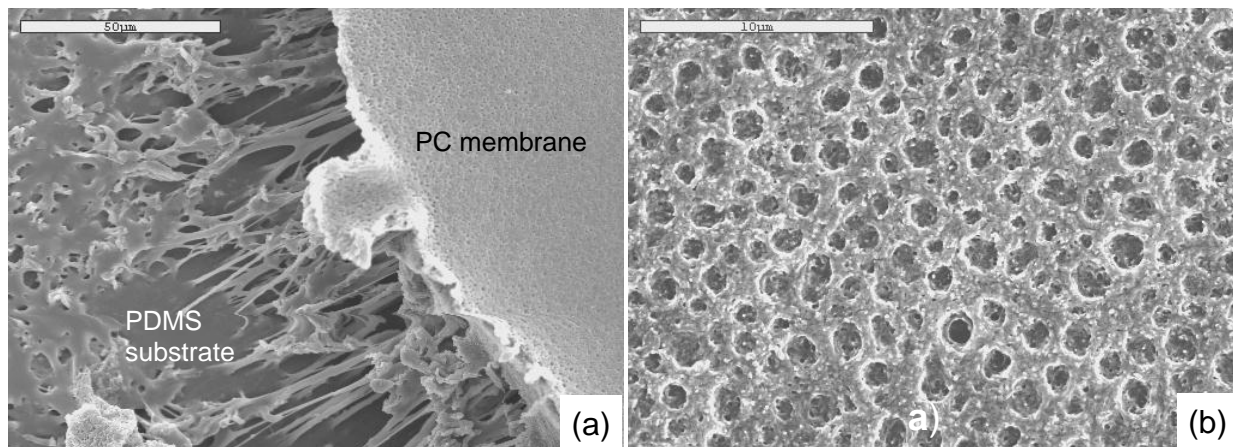


Figure 3-17. (a) The interface of PDMS substrate cast by PC membrane (pore size= 0.6  $\mu\text{m}$ ), where the membrane was partially dissolved in  $\text{CH}_2\text{Cl}_2$ . (b) PDMS surface was roughened after dissolving PC membrane.

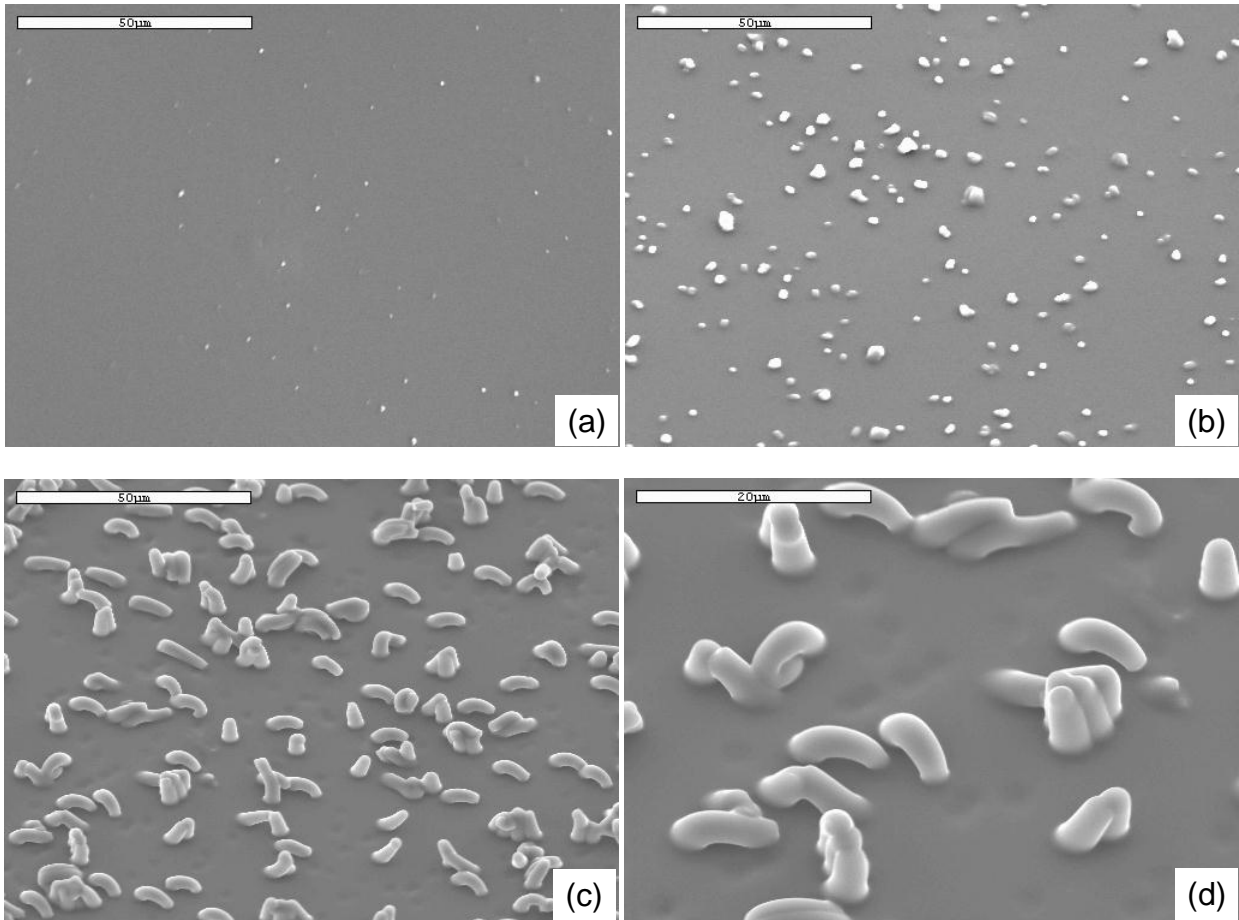


Figure 3-18. PDMS substrate cast with different pore size PC membrane. The membrane was removed by peeling. (a) 0.6  $\mu\text{m}$  (b) 1.2  $\mu\text{m}$  (c) 3.0  $\mu\text{m}$  and (d) a close-view of the 3.0  $\mu\text{m}$  posts.

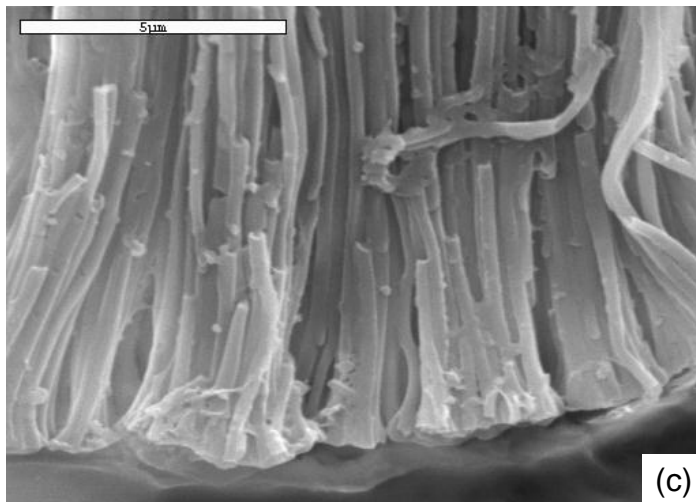
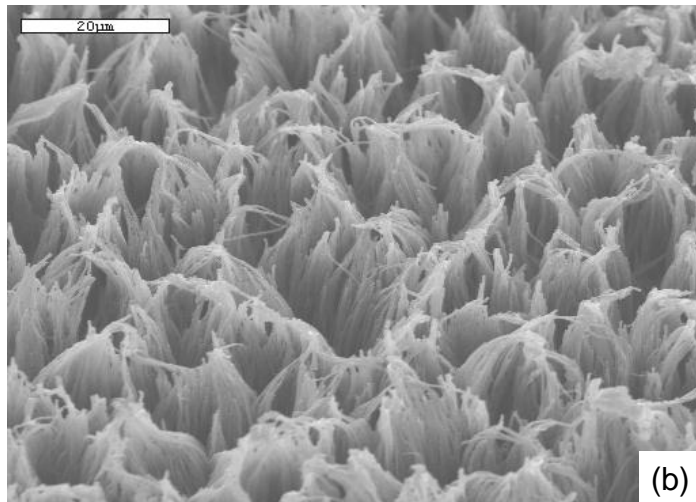
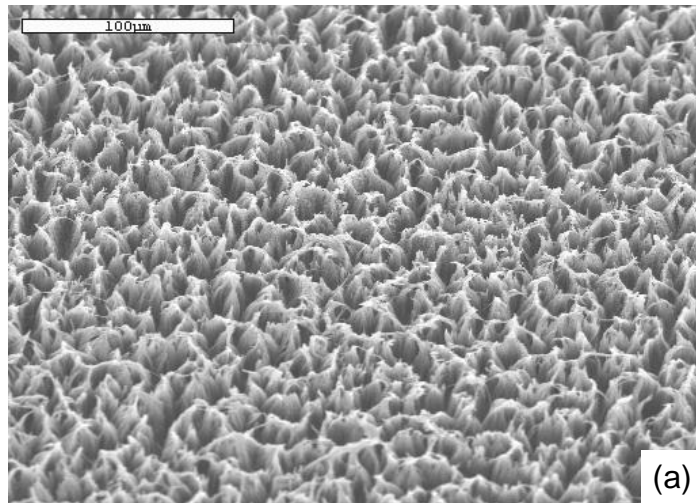


Figure 3-19. The microstructure of PP substrate cast with AAO membrane ( $\phi=0.2\mu\text{m}$ ). (a) and (b) High areal density causing hundreds of submicron-sized fibers clumped together and curled randomly. (c) Tube-like structure can be seen.

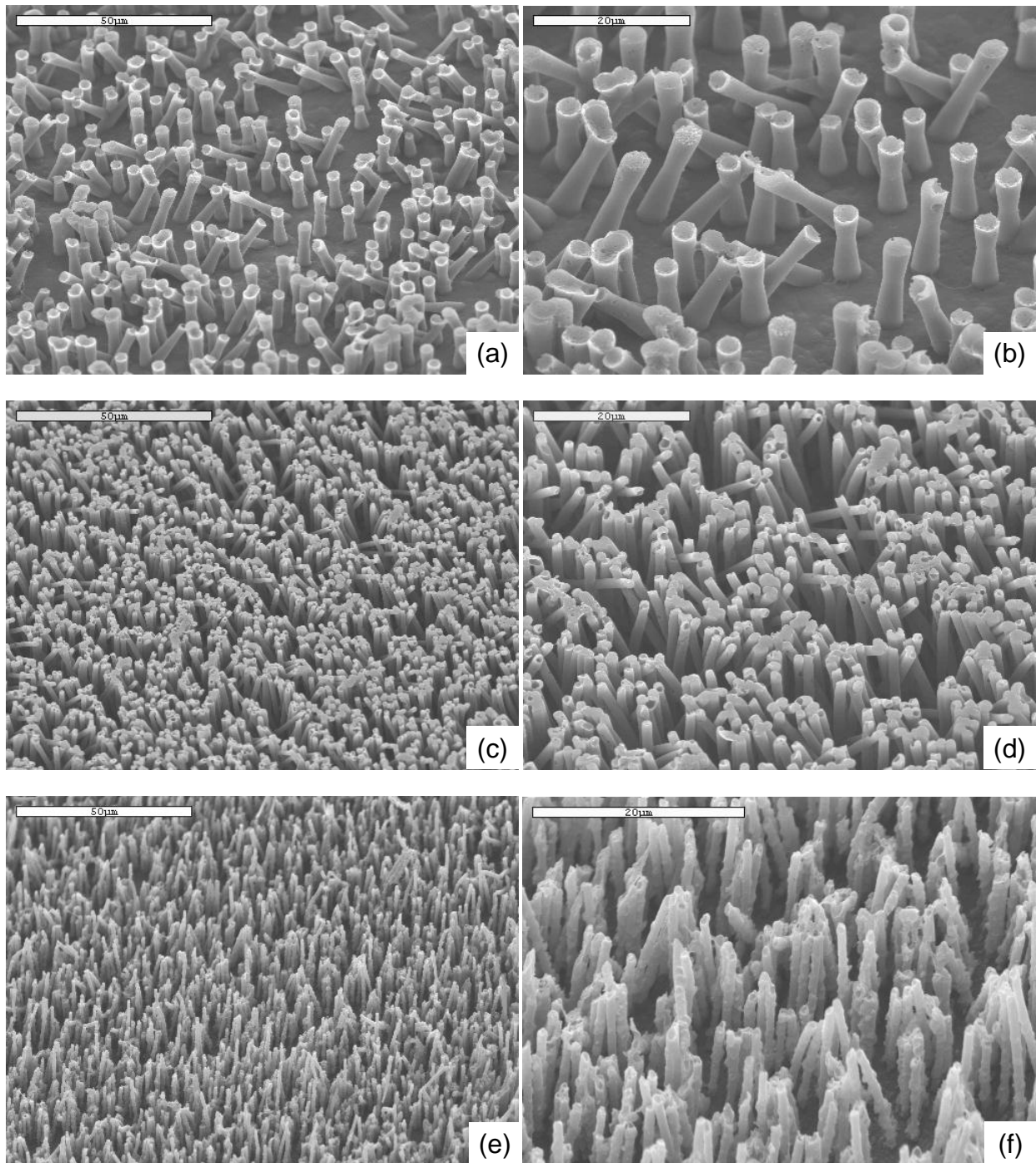


Figure 3-20. PP substrate cast with different pore size PC membrane. The membrane was dissolved after casting. (a) and (b)  $\phi=3.0\mu\text{m}$ , (c) and (d)  $\phi=1.2\mu\text{m}$ . (e) and (f)  $\phi=0.6\mu\text{m}$ .

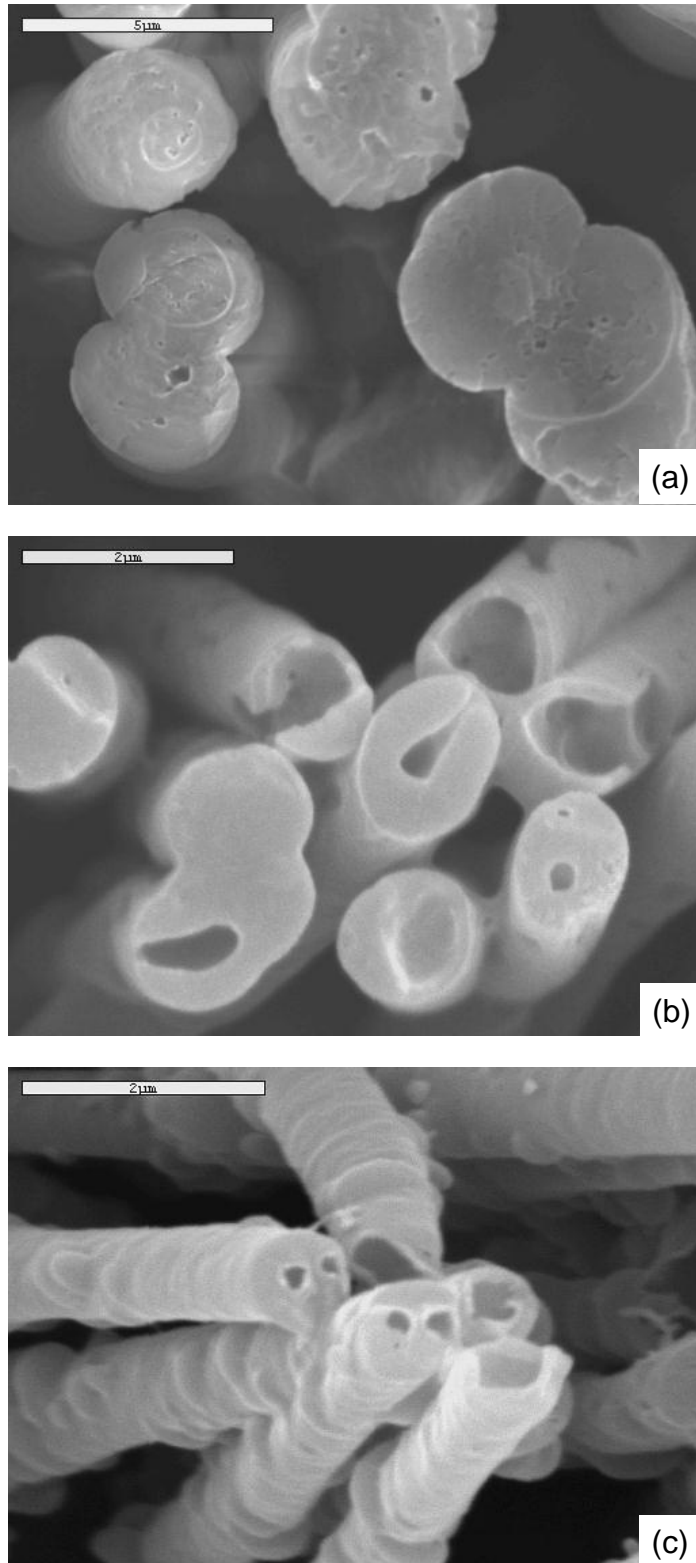


Figure 3-21. Top-viewed post structure of cast PP substrate after dissolving the membrane. (a)  $\phi=3.0\mu m$  (b)  $\phi=1.2\mu m$  and (c)  $\phi=0.6\mu m$ . The tube structure is formed with the decrease of pore size.

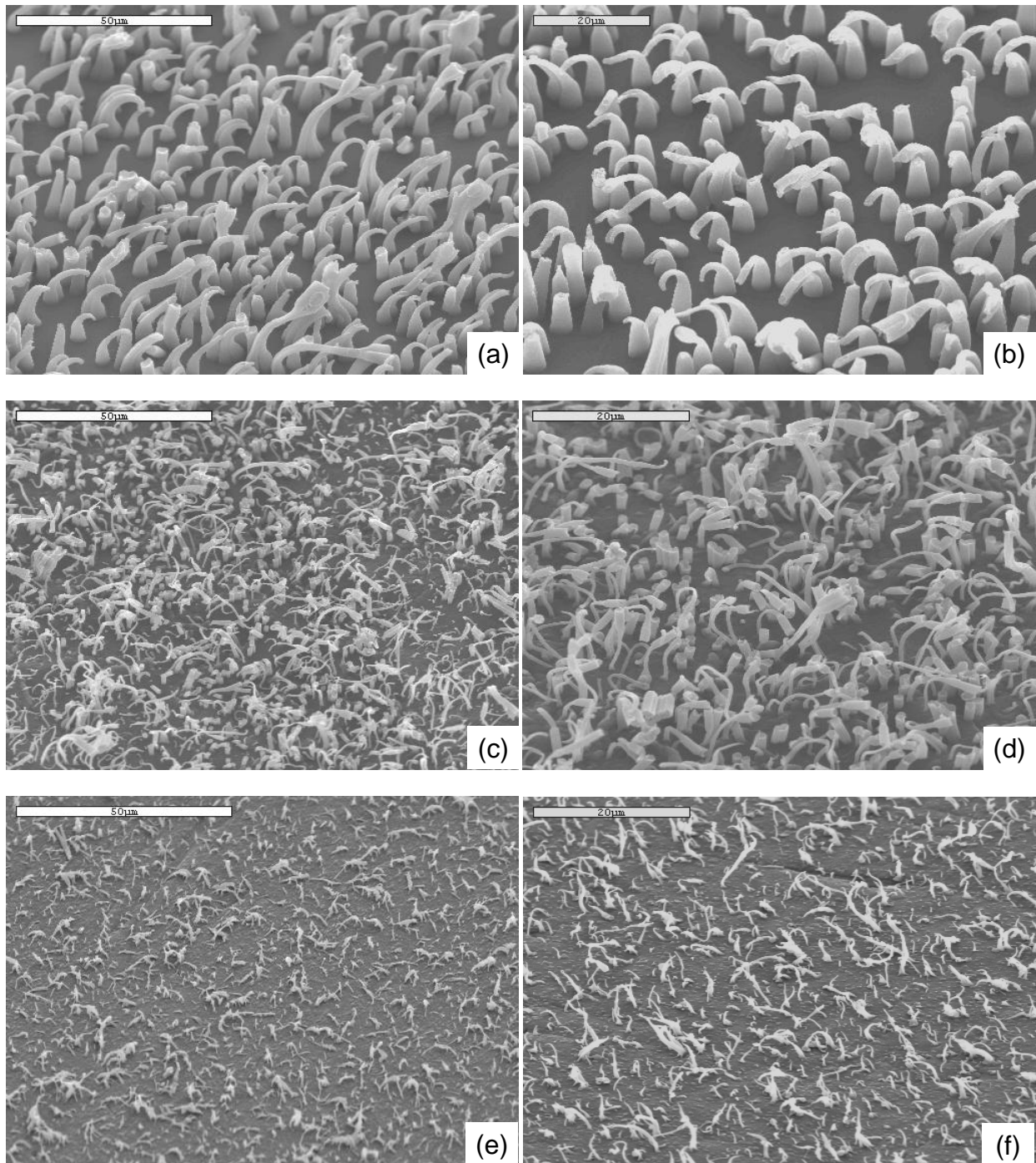


Figure 3-22. PP substrate cast with different pore size PC membranes. The membrane was peeled off after casting. (a) and (b)  $\phi=3.0\mu\text{m}$ , (c) and (d)  $\phi=1.2\mu\text{m}$ . (e) and (f)  $\phi=0.6\mu\text{m}$ .

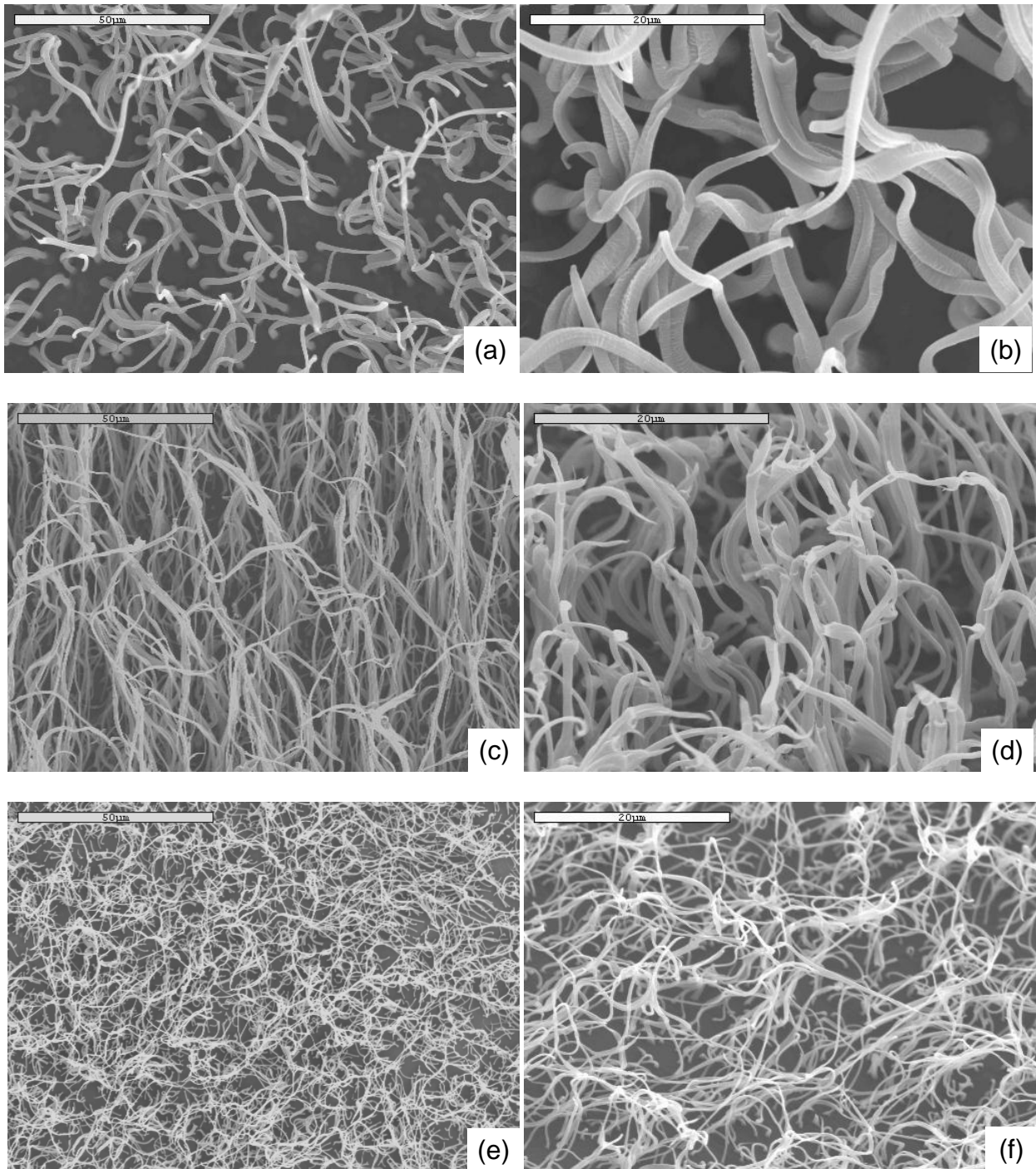


Figure 3-23. LDPE substrate cast with different pore size PC membranes. The membrane was dissolved after casting. (a) and (b)  $\phi=3.0\mu\text{m}$ , (c) and (d)  $\phi=1.2\mu\text{m}$ . (e) and (f)  $\phi=0.6\mu\text{m}$ .

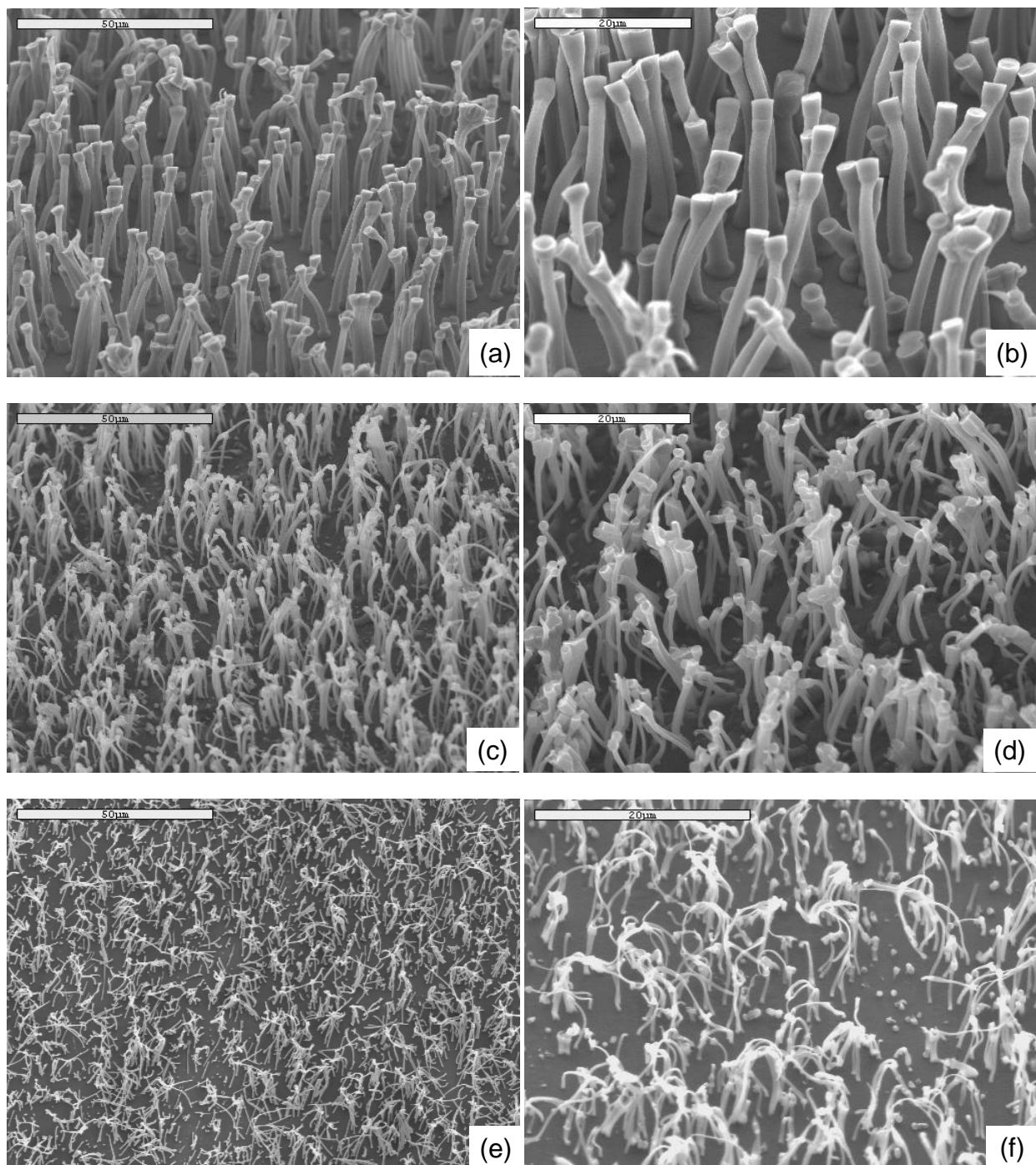


Figure 3-24. PVDF substrate cast with different pore size PC membranes. The membrane was dissolved after casting. (a) and (b)  $\phi=3.0\mu\text{m}$ , (c) and (d)  $\phi=1.2\mu\text{m}$ , (e) and (f)  $\phi=0.6\mu\text{m}$ .

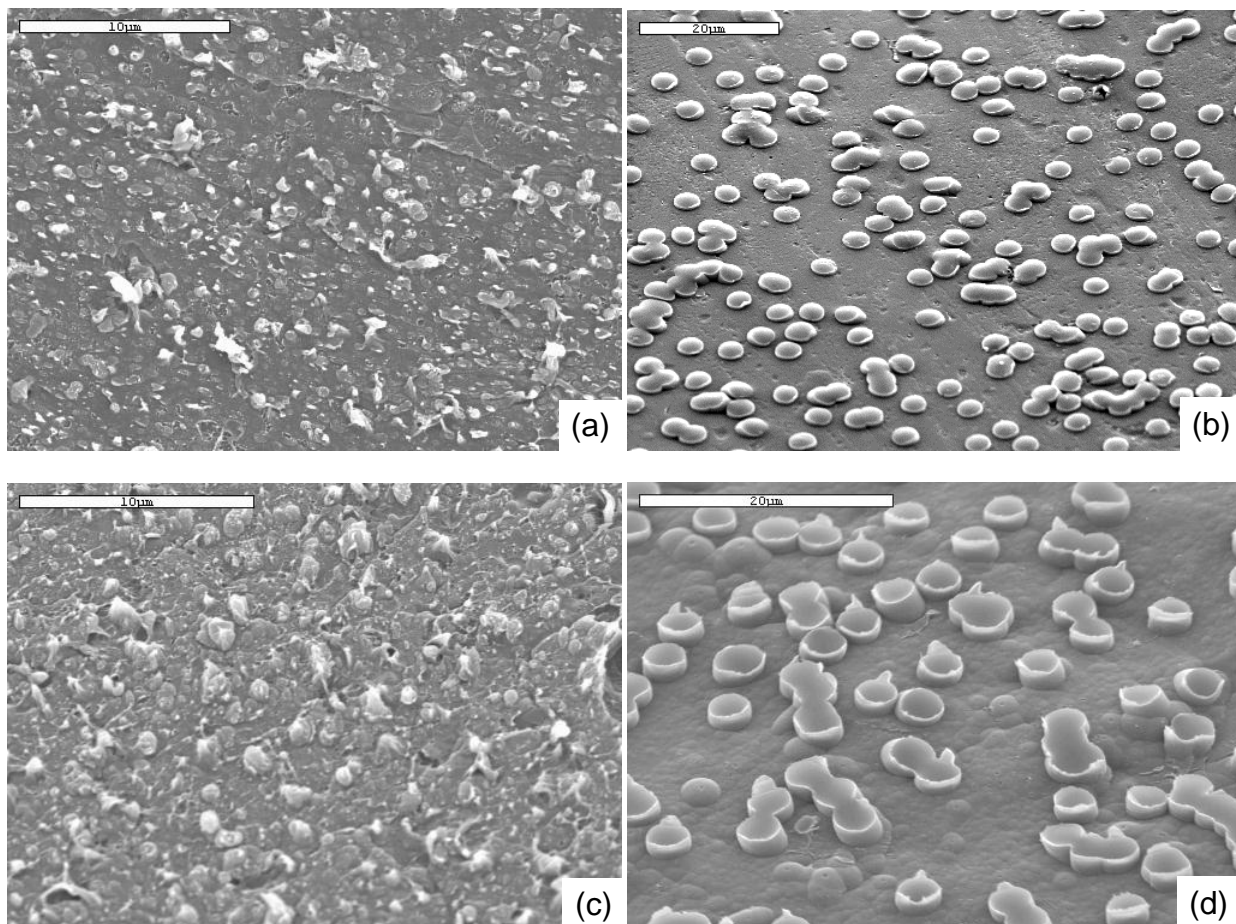


Figure 3-25. (a) and (b) are PS substrates cast with  $\phi=0.6\mu\text{m}$  and  $1.2\mu\text{m}$  PC membrane, respectively. (c) and (d) are PMMA substrates cast with  $\phi=0.6\mu\text{m}$  and  $1.2\mu\text{m}$  PC membrane, respectively.

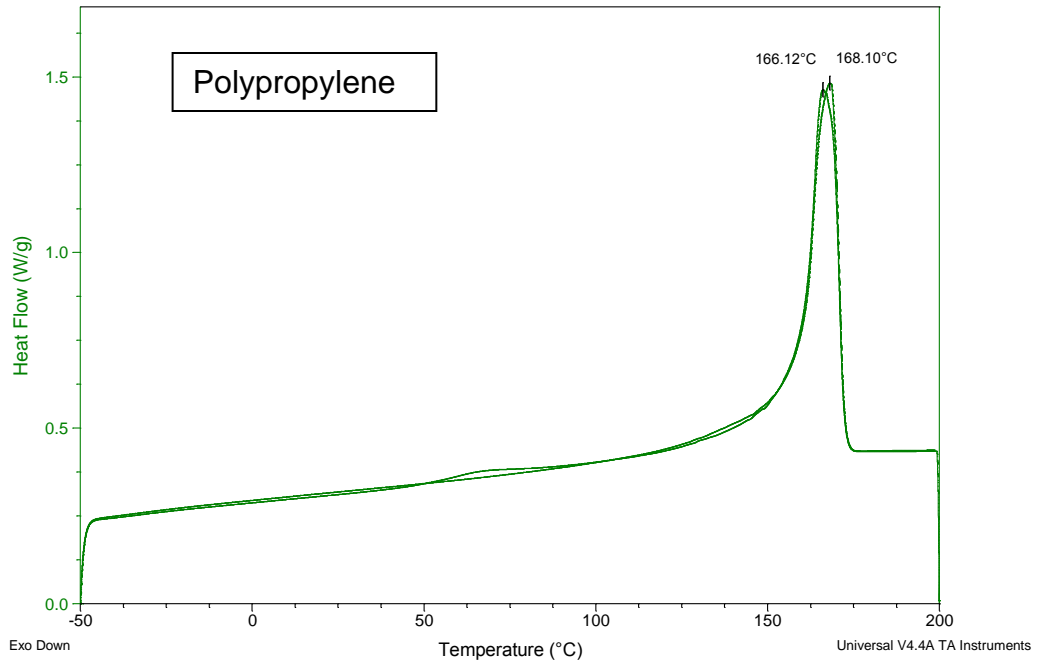


Figure 3-26. DSC analysis curve of PP substrate shows a melting temperature at around 168°C.

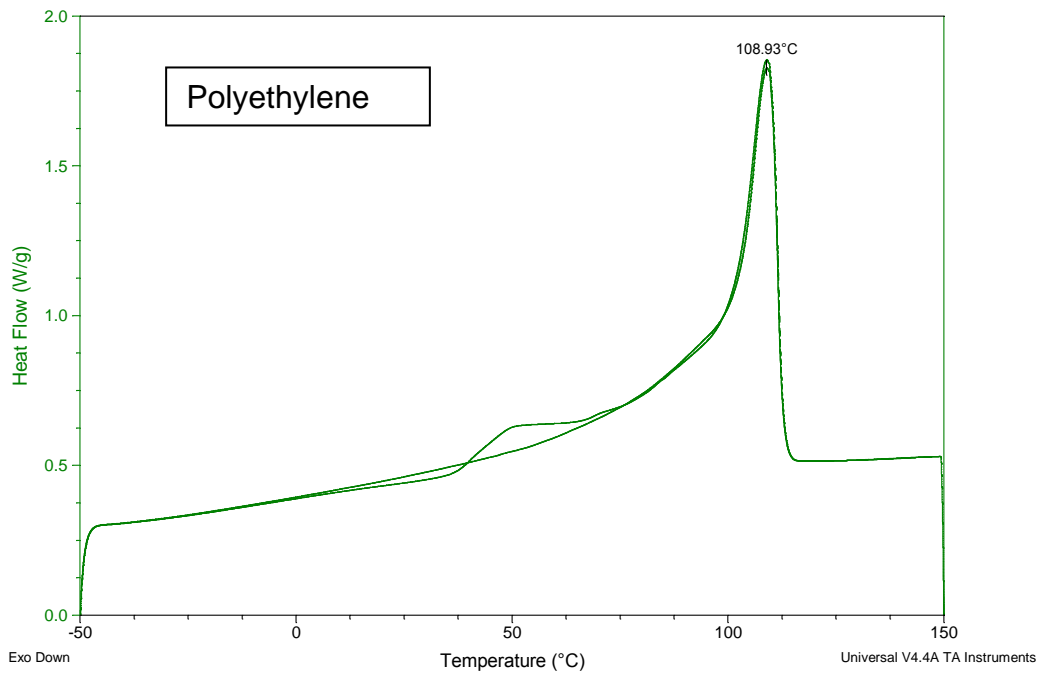


Figure 3-27. DSC analysis curve of LDPE substrate shows a melting temperature at around 109°C.

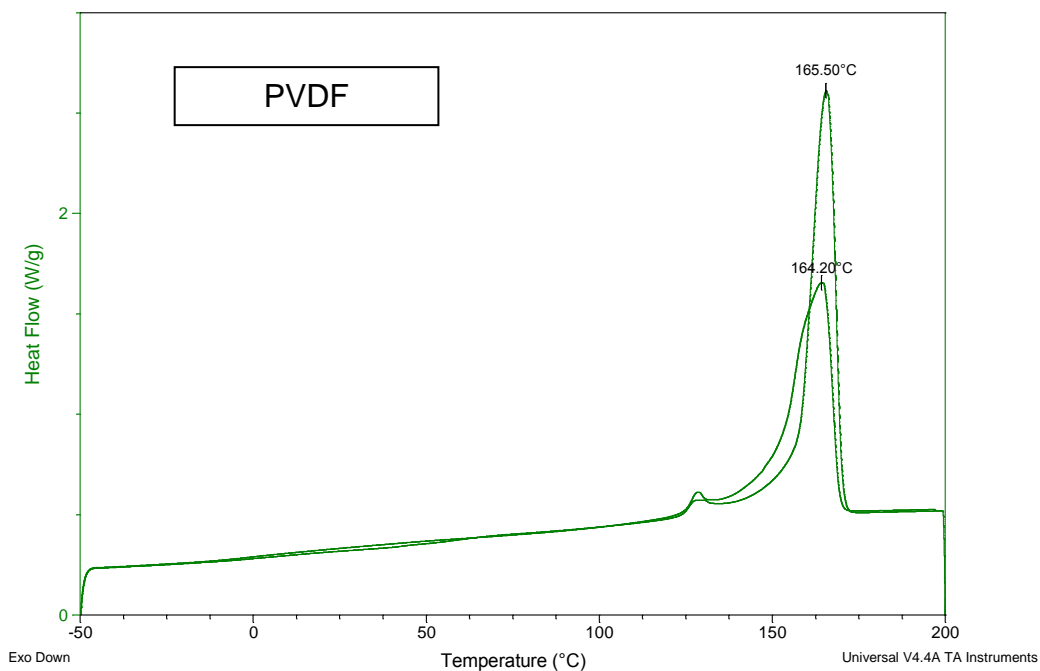


Figure 3-28. DSC analysis curve of PVDF substrate shows a melting temperature at around 165°C.

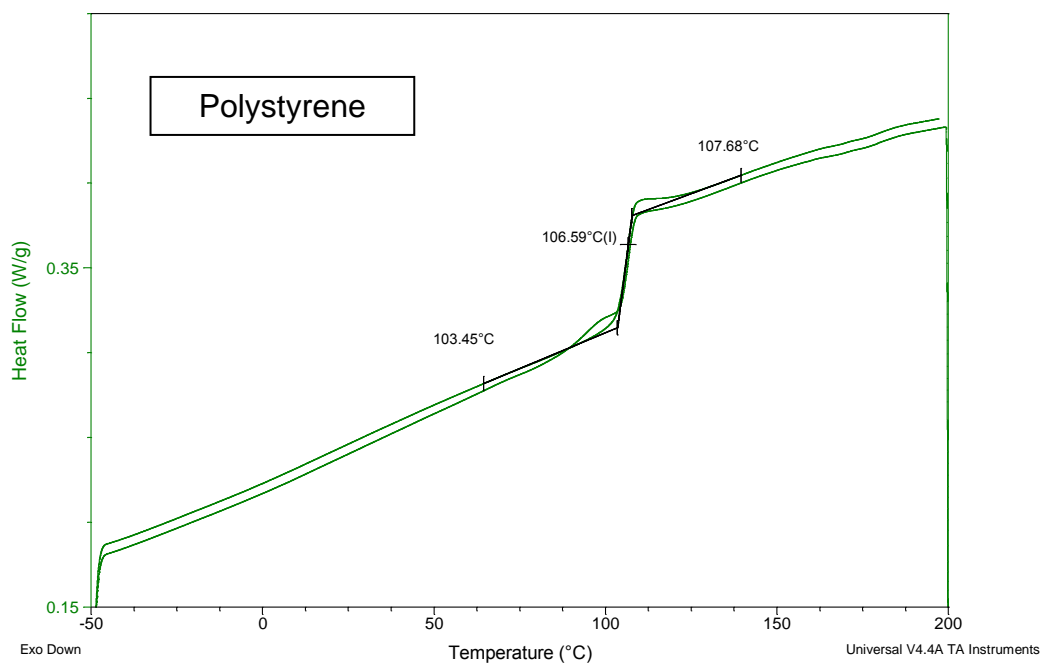


Figure 3-29. DSC analysis curve of PS substrate shows a glass transitional range between 103°C and 107°C.

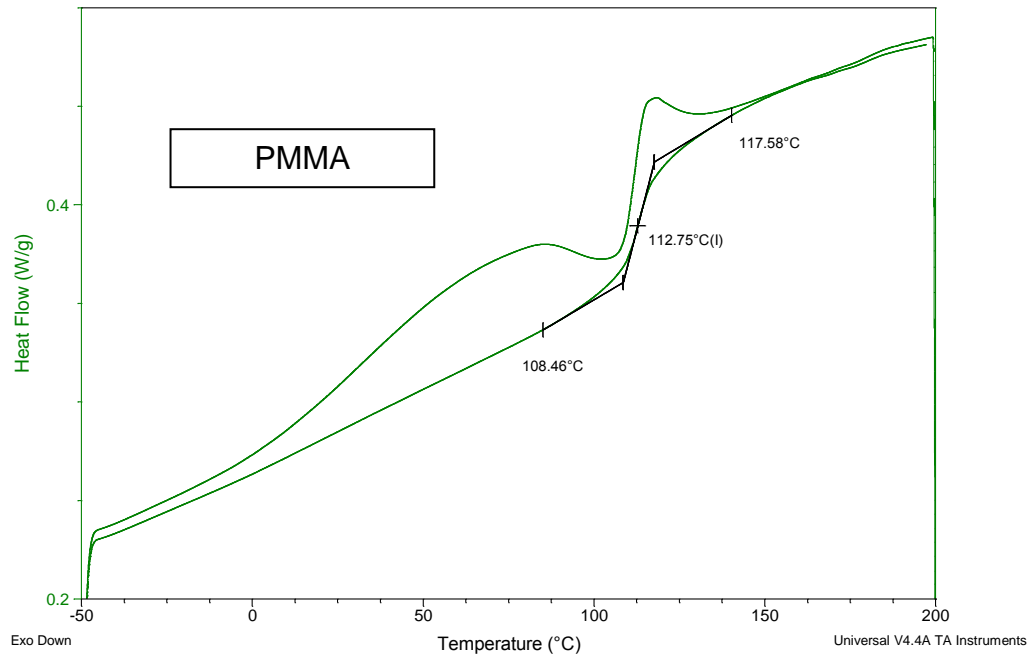


Figure 3-30. DSC analysis curve of PMMA substrate shows a glass transitional range between 108°C and 117°C.

Table 3-2. Casting temperature, glass transition temperature ( $T_g$ ) and melting point ( $T_m$ ) of the thermoplastic substrates used in this work. The data was measured and given by DSC.

Thermoplastics	Hair-Like Structure	Casting Temperature (°C)	Glass Transition Temperature ( $T_g$ , °C)	Melting Temperature ( $T_m$ , °C)
PP (Polypropylene)	yes	140	-	168.1
LDPE (Low-density polyethylene )	yes	190	-	108.9
PVDF (Polyvinylidene fluoride)	yes	190	-	164.2
PS (Polystyrene)	N/A	200	106.6	-
PMMA (Polymethyl methacrylate)	N/A	160	112.7	-

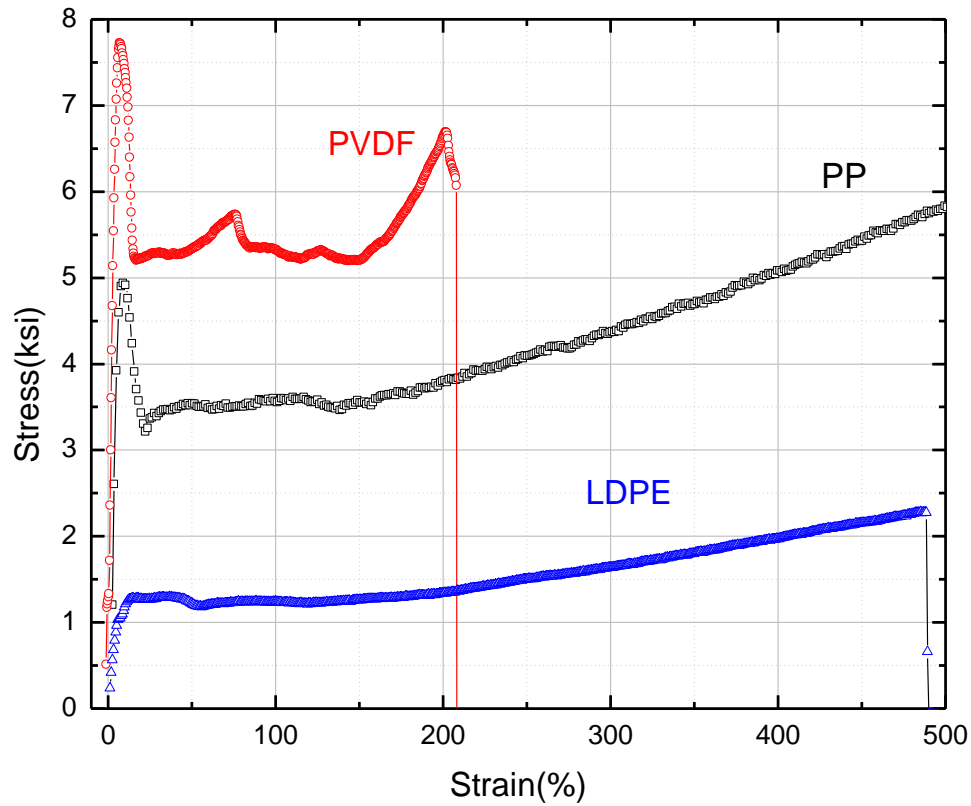


Figure 3-31. Stress-strain curve of the thermoplastics used in mould casting.

Table 3-3. Mechanical properties of the thermoplastics used in mould casting.

Thermoplastics	Young's modulus (GPa)	Yield strength (MPa)	Tensile strength (Mpa)	Elongation at break (%)
PP (Polypropylene)	0.62	34.0	15.8	630
LDPE (Low-density polyethylene)	0.14	6.1	51.7	485
PVDF (Polyvinylidene fluoride)	1.23	51.7	46.1	180

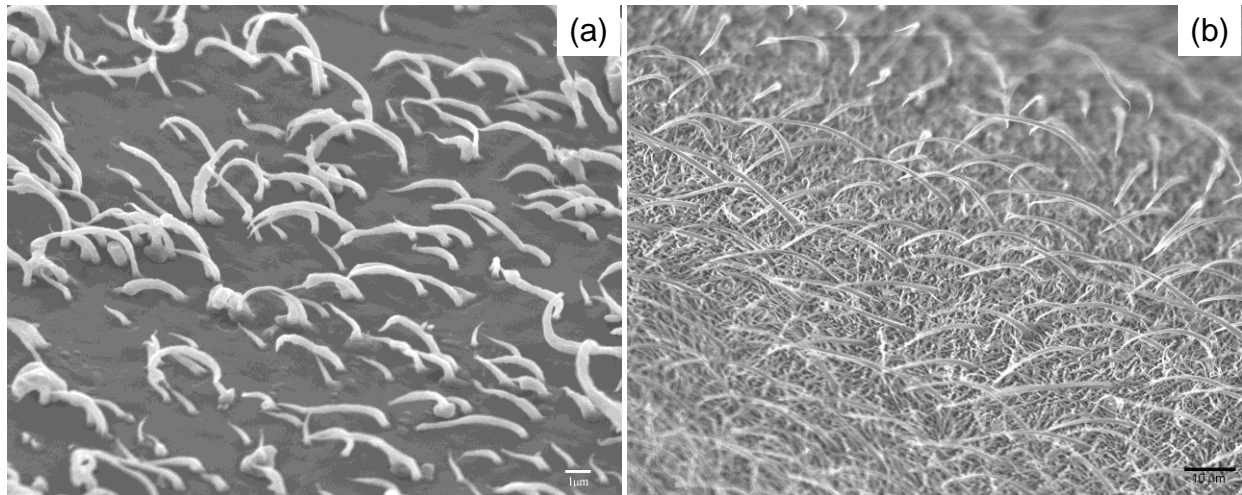


Figure 3-32. (a) The surface microstructure on PP substrate after peeling off the PC membrane. (b) The microstructure of water strider's abdomen. Note that there are two different sets of hairs on water strider. Longer hairs are bent inwards towards the body, which hinder the piercing the water surface.

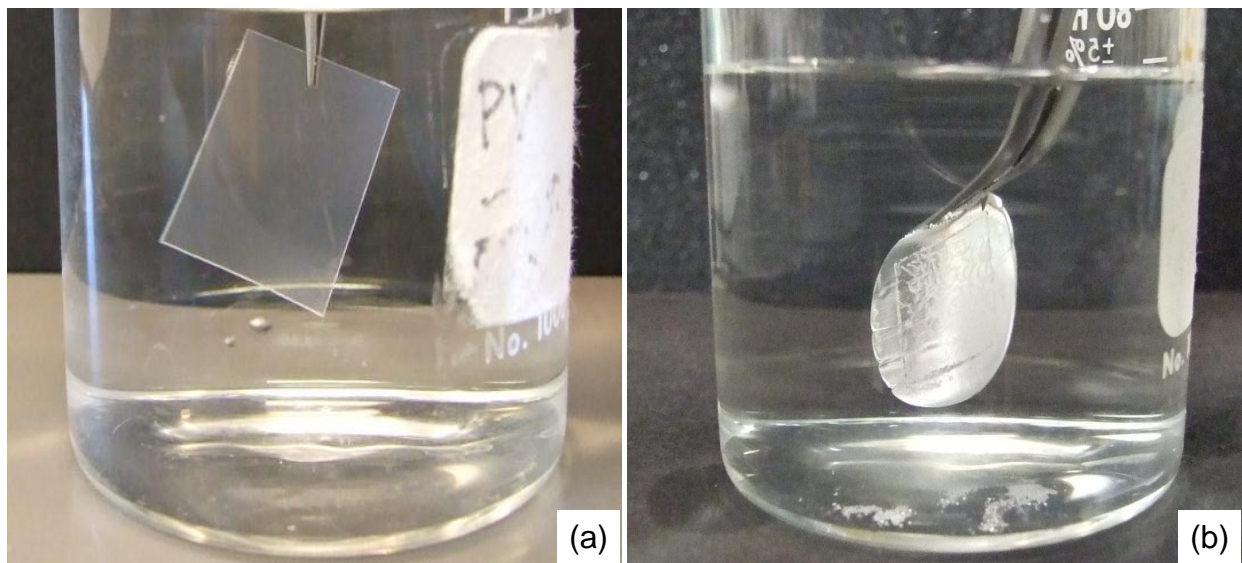


Figure 3-33. (a) Immersed PP sheet without any particular surface structure. (b) Immersed PP sheet with artificial hairy structure on it. The silver look comes from the total reflection from thin air layer trapped on the substrate surface.

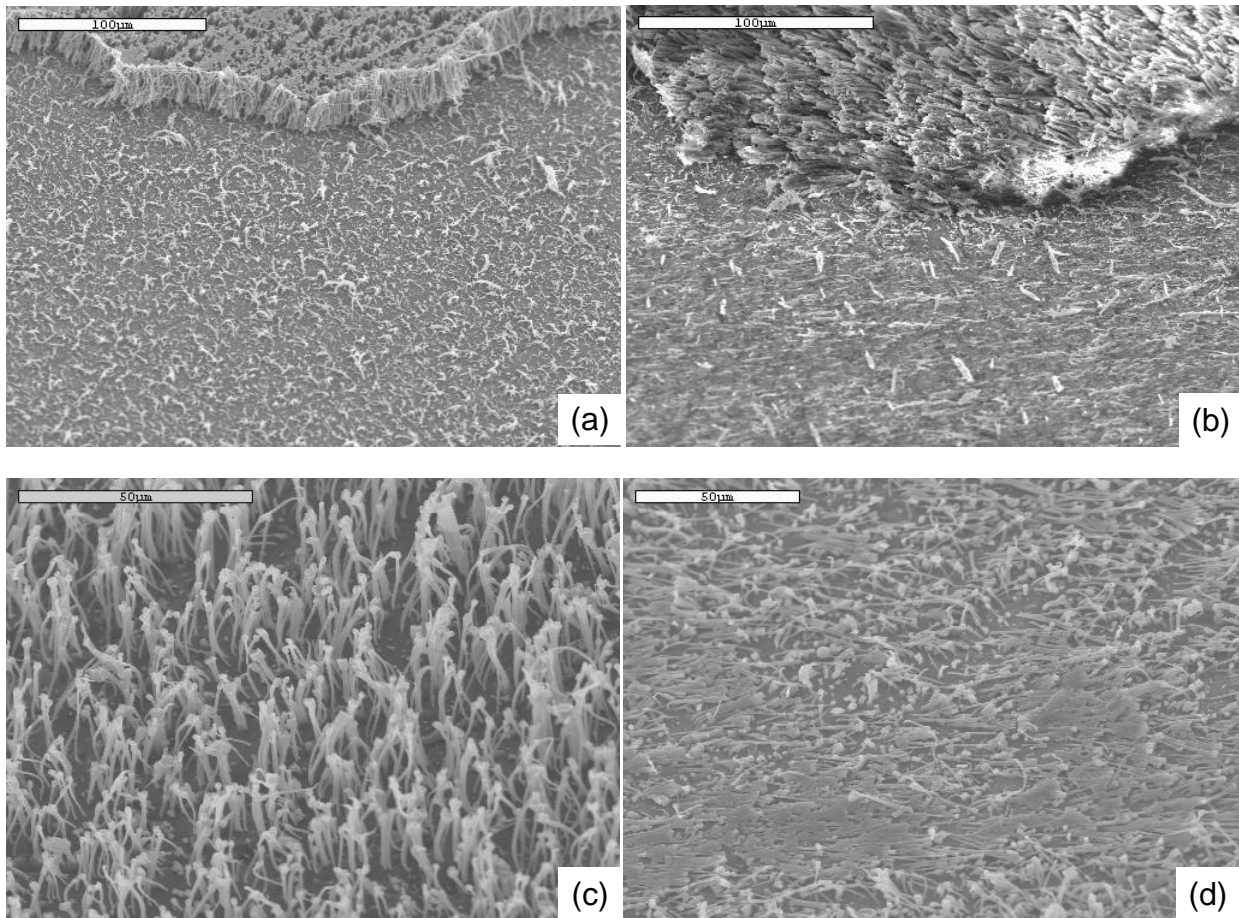


Figure 3-34. (a) and (c) are microstructure of cast PP ( $\phi=0.6\mu\text{m}$ ) and PVDF ( $\phi=1.2\mu\text{m}$ ) substrate. (b) and (d) are the microstructure after being rubbed by fingers.

## CHAPTER 4 WETTABILITY OF HAIRY SURFACES

The central property, wettability or hydrophobicity, of different surfaces, including natural and artificial hairy structure, is presented in this chapter. The wettability was evaluated by contact angle measurement via image based technique. Due to superior water repellency on some of the artificial surfaces, an alternative video assessment was also used here. The concerns and experimental work regarding the determination of contact angles are given in the first section. The results of the surfaces created in this work are described in the following section, where natural hairy surfaces are also included. The final part is to associate the wetting properties with the surface structure, and to draw a conclusion towards making optimal superhydrophobic interfaces with hairy structure.

### **Contact Angle Measurement**

The contact angle is the angle at which three different phases meet one another and is not limited to liquid/vapor on solid surfaces. The case people are specifically interested in is how the liquid droplets act on solid surfaces. Hydrophobicity is often characterized by the static contact angle measurement of water. The general principles are to assume:<sup>88</sup>

- (1) The drop is symmetric about a central vertical axis, which indicates that the drop shape is irrelevant from which direction it is viewed.
- (2) The drop shape is only determined by the balance of interfacial forces and the gravity. Their viscosity or inertia of the liquid does not shape the drop.

Typically, contact angle measurements are carried out by acquiring images of resting drops on a surface through a specific apparatus, a goniometer. The image is

then analyzed by fitting a mathematical expression to the shape of the drop where the slope of the tangent to the drop at the liquid-solid-vapor interface line will be calculated.

### **Concerns of Contact Angle Measurement**

The concept of interpreting contact angles has been developed over 150 years;<sup>1</sup> however, a recognized standard protocol of measuring contact angles is not yet established, although contact angle is widely measured and used in academia and industry nowadays. Therefore, even within the same system, the value of angles may vary if the measurements are performed differently. The purpose of this section is to present a few general concerns in contact angle measurement from the practical perspective, especially for samples showing extreme hydrophobicity, and, in addition, to specify some details of the measurements taken.

- (1) **Drop size:** If the drop is too large, the shape will be distorted because of the gravity. Too small of a drop, however, will be difficult to place on the surface, especially for the surfaces showing superior hydrophobicity. Small drops may also cause a state transition from the CB state to Wenzel state,<sup>29</sup> leading to an entirely false angle. There is no definitive volume of drops for contact angle measurement. The value is generally below 10  $\mu\text{l}$  for each drop, and most reports have their volume around 5  $\mu\text{l}$ . Using the same volume of drops throughout the entire measurement is essential.
- (2) **Drop placement:** All superhydrophobicity is located in the meta-stable Cassie-Baxter regime, which means it may turn to a more stable Wenzel state if an external force applied. Therefore, the drops should be placed on the surface with as small a force as possible. In other words, rather than just falling upon the surface, the drops should touch the surface by either raising the sample stage or lowering the syringe until the drop touches the sample surface. This will minimize the kinetic energy as well as the drop spreading before taking the images.
- (3) **Syringe size:** Ideally, the diameter of the syringe tip should be infinitesimal when compared with the drop size. For a surface with moderate hydrophobicity, this may not be a major issue, since the syringe is not in contact with the drop during the measurement. However, when dealing with an extremely hydrophobic surface, due to the low adhesion between the surface and drops, the drops will stay on the tip of the syringe resulting in a possible distortion of the drop shape (Figure 4-1a). Thus, for the experiment, the plastic tip of the syringe equipped on the goniometer

was replaced with a 30-gauge needle (Figure 4-1b, OD: 0.260 mm, ID: 0.159 mm) to reduce the influence.

- (4) **Image quality:** Acquiring a clear image is probably the most crucial part, since the modern contact angle determination merely relies on mathematical analysis of the drop's contour. Regarding the image, the contrast of an image should be high enough to have a clear, distinguishable profile, especially for the bottom portion where the drop is in contact with the substrate. This is usually a challenge when dealing with the superhydrophobic surfaces ( $\theta_c > 150^\circ$ ) since the drop has a very limited contact area with the substrate. An auxiliary light source is sometimes needed to obtain a clear image. Constantly adjusting the stage, focus, aperture, and lighting from sample to sample is always necessary for optimizing image quality.
- (5) **Fitting model:** As stated above, the contact angle was analyzed by fitting it to a mathematical model, and consequently, the value significantly varies with the model applied. Unfortunately, not every previous work specified the fitting model used when reporting their results. Zhang et al.<sup>4</sup> reported that even for the same image, the angle value could vary from  $150^\circ$  to almost  $180^\circ$  if different fitting models were applied. (Figure 4-2) This variation is related to the mathematical expression and also to the deformation of the water droplet caused by gravity. Therefore, in dealing with superhydrophobic surfaces, the value of contact angles above  $150^\circ$  may not exactly reflect the real situation of surface wetting, if the fitting mode is not clearly mentioned.

All of the above are important issues that should be taken into consideration in contact angle measurement. The key is to perform the measurement under the same condition, and report it clearly. Since no standard protocol to date has been built for the measurement, a direct comparison between different values may not be sound without specifying the detailed setting.

### **Fitting Model of Contact Angle Measurement**

Various methods of drop shape fitting exist, but the commercial software designated for contact angle analysis is still very limited. They are often accompanied with particular facilities and may not be reliable if used under other conditions. Because of this, the direct measurement of a drop by using a goniometer with a telescoped protractor is still used nowadays, even with a major drawback coming from the

subjectivity. The fitting method used in this experiment was based on a so-called B-spline snakes that was developed by Stalder et al.<sup>89</sup> for measuring high-accuracy contact angles. Snakes were originally defined as a spline energy minimization under internal and external forces,<sup>90</sup> and are now widely used in computer-assisted tools for segmentation, such as medical image analysis or feature tracking in video sequences.

The whole model has been programmed as a Java plug-in, named *DropSnake*, for the *ImageJ* image processing software.<sup>91</sup> The program uses not only the whole drop contour to provide global information but the local polynomial-fitting as well in order to extract the value of contact angles. Presenting its detailed mathematics is far beyond the scope of this dissertation. This approach generally improved some drawbacks from only using polynomial-fitting models and ADSA (axisymmetric drop shape analysis), in which the assumption of axisymmetrical drops is not actually fulfilled in many cases. This is extremely important for my system since the surfaces observed are mostly with non-uniformly distributed micro-features that usually result in a non-axial-symmetrical drop. From a user's perspective, the program is a plug-in for the freeware *ImageJ*, which is very cost-effective and allows for the analysis of images independently without sticking to a particular goniometer. The following results of contact angles were all measured by this program. More detailed information and the program itself can be found from their website.<sup>92</sup>

## **Experimental Work of Wettability Evaluation**

### **Static Contact Angle Measurement**

All the contact angle measurements were carried out at ambient temperature (~23°C) with a goniometer, Ramé-Hart Model 100, equipped with an automated dispensing system and a 30 gauge flat-tipped needle. Figure 4-3 shows the equipment

of goniometer, which consists of a CCD camera, light source and an automated syringe pump. The images were recorded by its operation software. Water purified through Milli-Q system ( $\rho > 18 \text{ M}\Omega\text{-cm}$ , Millipore Inc.) was used as the main probe fluid, while water-methanol mixtures and other organic solvents were also used as a low-surface probe liquid. (Table 4-1)

For sessile drop test, images were photographed by putting  $4 \mu\text{l}$  of water droplet onto at least 5 different areas of the sample. The needle was lowered towards the sample to carefully place drops on the surface, and then the needle was removed away from the drop. For surfaces with extreme hydrophobicity, the drops may not be able to be placed on the surface, and the needle was kept within the drop during the measurement. The captured images were analyzed by *DropSnake* program, a plug-in for the *ImageJ* software. (Figure 4-4) The mean value of the water contact angle and its standard deviation were reported as contact angle ( $\theta_c$ ).

### **Contact Angle Hysteresis Measurement**

Advancing angle and receding angle were also measured by goniometer. Images for advancing angle were recorded as follows: fluid was gradually added into the droplet, typically  $0.05 \mu\text{l}$  at a time, and images were captured after the fluid introduced each time. The advancing angle was determined specifically from the image frame before the advance of the liquid interface was observed. Receding angle determination was performed by the same process but withdrawing the fluid from the droplet instead. The receding angle was determined specifically from the image frame before the retreat of the liquid interface was observed. The measurement was carried out on three

different places for each sample. The value of angles was also analyzed by *DropSnake* analysis program.

### **Video Assessment of the Surface Hydrophobicity**

For extremely hydrophobic surfaces, the degree difference between advancing angle and receding angle may be too small to be measured. I employed a video based assessment, a so-called contact/compress/release test, to examine the degree of hydrophobicity or water adhesion of the surface. Without using sophisticated equipment, the whole activity on the computer screen was directly recorded using “desktop casting” software while performing the experiment. The test did not provide quantitative numbers but a qualitative evaluation. The test was conducted by using a supported water droplet on an upper side, typically supported by a plastic syringe or a substrate. The supported droplet was slightly compressed on the surface with the advancement of the syringe, and then the syringe was slowly withdrawn from the surface. The key frame was the one right before the droplet detached from the surface. The interface distortion during the detachment (Figure 4-5) represented the degree of the surface hydrophobicity. During the droplet compression, the sample stage could also be moved to examine the surface uniformity.

### **Surface Tension Determination**

The surface tension of the liquid used for contact angle measurement was measured by the Wilhelmy plate method. The method consists of a thin platinum plate hanging under a microbalance via a thin metal wire. The platinum surface was roughened, along with its high surface energy, to ensure complete wetting ( $\theta \sim 0^\circ$ ). Before the measurement, the platinum plate was fired by a gas burner, and then rinsed with acetone and DI water to thoroughly remove any substances on the surface. The

plate was immersed into the liquid and then the container was gradually lowered away from the plate. The force on the plate due to wetting was showed on the microbalance. The surface tension ( $\gamma$ ) of the liquid can be calculated by using the Wilhelmy equation:

$$\gamma = \frac{F}{L \cdot \cos \theta} \quad (4-1)$$

where  $L$  is the wetted perimeter ( $2w + 2l$ ) of the Wilhelmy plate and  $\theta$  is the contact angle between the liquid phase and the plate (Figure 4-6). In practice the contact angle is rarely measured, complete wetting ( $\cos \theta = 1$ ) is usually assumed for the calculation.

### **Contact Area and Theoretical Contact Angle Interpretation**

Theoretical contact angles,  $\theta_{CB}$ , were calculated by using the Cassie-Baxter equation (2-9):

$$\cos \theta_{CB} = f_s (\cos \theta_c + 1) - 1 \quad (2-9)$$

where  $\theta_c$  is the contact angle measured on the uncast, original substrate, and  $f_s$  is the area fraction of the droplet in contact with cast structure. The cast structure is generally not regular, so it is a great challenge to estimate the actual fraction of contact area. This number was estimated through analyzing the top-viewed SEM pictures by *ImageJ*. (Figure 4-7) Since the emission of secondary electrons is higher at the tips, it is assumed that the brightest regions showing on the SEM picture are those in contact with the droplet. Therefore by adjusting the threshold, a range of the contact area fraction can be determined by the software.

## **Wetting Property of Hairy Plants**

### **Observations on Hairy Leaves**

Observing nature, as a fundamental step in the scientific method, is always stimulating. This research is inspired by the hairy exterior of natural species that show

water repellency. As mentioned in Chapter 2, a number of examples have been found in both the animal and plant kingdom. Since the hairy integument from the animal kingdom is usually just few millimeters, observing hairy plants is a more feasible option.

However, even though water repellency on hairy plants has been broadly acknowledged, they have not all been extensively studied. For example, the Lotus Effect has been extensively studied, while research on the Lady's Mantle is very sparse. Observations for some hairy plants, along with the latest experimental work from other studies, have been presented to provide a better understanding on this phenomenon.

The hairy plants, Tomato (*Solanum lycopersicum*), Hummingbird Plant (*Dicliptera Suberecta*) and Lady's Mantle (*Alchemilla vulgaris* L.), were used to observe the wetting behavior. The emblem of superhydrophobicity, the Lotus leaf, was also included. Most of the analysis was performed on the leaves of Lady's Mantle. Because the dense hairs blocked the view from the base of the droplets, contact angle measurement was unable to be performed precisely on these hairy plants. Due to a lack of a CCD camera mounted microscope, the interaction between the droplets and the hairs was mainly investigated under a stereo optical microscope (Olympus SZ-40), and the images were directly captured simply by placing a commercial digital camera (Sony DSC T-33) on the lens. The images were restricted at certain angles, but they allowed us to perform a qualitative study. Other observations were also filmed by digital camera. The morphology and the areal density of the hairs were studied by SEM without a conductive coating on the leaves.

### **Droplets on Hairy Plants**

Water deposited on these hairy plants all exhibited a similar response; they formed spherical droplets and slipped quickly off the leaves or to a concave spot. From the

goniometer, as shown in Figure 4-8a, the droplet, supported by the hairs (also known as *trichomes*), exhibited the apparent contact angle of exactly 180°. The surface of the leaves remained in a dry state, as these hairs acted like a shield. These hairs had an aspect ratio above 100, a diameter around 10  $\mu\text{m}$ , and a height up to around 1 mm. Electron microscopy confirmed that the cuticle of the Lady's Mantle was covered with cuticular wax crystals, similar to the Lotus leaf.

Figure 4-9a is a typical image taken under the optical microscope showing a droplet ( $\phi \sim 4\text{mm}$ ) resting on the dense hairs of the leaf of Lady's Mantle. The hairs penetrated into the droplet, yet still maintained their original configuration. In order to reveal if the hairs buckled when confronting the interface, a droplet hung on a syringe was slid on the leaf under a microscope. The results showed that the hairs in contact with the droplet penetrated directly into the interface and leaned towards the direction the droplet moved, as shown in Figure 4-9b (due to the limitation of the equipment, the picture quality was not optimum). The hairs neither seriously changed their arrangement, nor did they bend before and after they contacted the droplet. The force exerted from the droplet, including gravity and capillary attraction, did not seem large enough to cause a severe deflection.

Interestingly enough, during the composing this dissertation, a very similar result was reported by Bernardino et al. in their latest publication.<sup>93</sup> With a more modern imaging facility, they confirmed the hairs were fairly hydrophilic and caused a relatively large hysteresis, around 30°. The hairs were hardly bent when they were partially immersed into water. They also observed that the droplets were usually strongly pinned by the hairs and only rolled when the leaves tilted largely. Additionally, a simplified

model to estimate the total energy of the system was proposed by them. The model was based on three terms: the wetting energy, the capillary interaction between the hairs, and the elastic energy of bending the hairs. They found the existence of a local energy minimum could hardly be fulfilled. Both the hair length and the distance between them would need to be unusually large to have bending and clustering. Together with my observations, it is clear that the hairs are too stiff to be bent by the capillary interactions, and the hydrophobic behavior of the leaf is simply coming from the strong pinning of contact lines. Due to a large contact angle hysteresis, the hairs penetrating into the droplet hinder the motion of the interface and prevent the droplet from coming down to fully wet the hairs and substrate. As a result, droplets on the leaves with a lower hair density moved downwards more easily and got in contact with the substrate (Figure 4-10b).

### **Wetting Property of Artificial Hairy Surfaces**

The wetting properties of the various cast surfaces are presented in this section. The main characterization was based on contact angle measurement. A video assessment was also used to provide a qualitative evaluation of the hydrophobicity.

#### **Contact Angles of Cast PDMS Surface**

The PDMS silicone elastomer was cast with different moulds, including PC membranes and natural leaves. Their morphology and the resulting contact angles are shown in Figure 4-11. The cured PDMS elastomer was intrinsically hydrophobic with the contact angle at  $97^\circ$ . The surface structure duplicated from natural leaves was able to slightly increase the contact angle to  $102^\circ$ . After the PDMS elastomer surface was roughened by dissolving the PC membrane, the contact angle on the roughened

surface increased to 137°. For the membrane-peeled surface (pore size=3.0  $\mu\text{m}$ ), due to its smaller fraction of contact area, the contact angle had been significantly increased to the superhydrophobic region of 153°.

The PDMS has low surface energy (21.3 mN/m) and exhibits a hydrophobic property. The contact angle increases with increasing surface roughness. The leaf structure was successfully duplicated because of its low areal density of the hairs, and it was not able to hold the droplet in a Cassie state. As a result, the contact angle was increased slightly,  $\sim 120^\circ$ , but was still lower than the leaf itself. This may be caused by a lack of the cuticular wax crystals, which commonly exist all over the leaves and enhance the hydrophobicity. For the membrane-dissolved surface, the surface was left with small cavities that enabled air to be trapped underneath and resulted in a high contact angle. From the image analysis, the fraction of contact area was estimated from 45% to 50%, and the consequent theoretical contact angle based on Cassie-Baxter equation was  $127^\circ$  to  $124^\circ$ . The smaller contact area from membrane-peeled surface causes a contact angle larger than  $150^\circ$ .

### **Contact Angles of Cast Thermoplastic Surface**

The pictures of the sessile drops from contact angle measurement and their associated microstructures have been brought together to illustrate the wetting behavior. In order to elucidate the results, the values of contact angles, advancing angles, and receding angles, along with their estimated contact areas and theoretical contact angles, of all the surfaces are listed in Table 4-2.

## Polypropylene substrate

The polypropylene sheets were cast with two types of membrane, polycarbonate (PC) and anodic alumina (AAO). Due to the small sample size of AAO-cast surfaces, the following contact angle measurements were conducted on the PC-cast surfaces only. Since most of the membrane-peeled samples were somewhat curved, the samples were taped onto glass slides to have a larger flat region for contact angle measurement.

The original PP sheet was relatively hydrophobic and had a contact angle slightly larger than  $90^\circ$  (Figure 4-12a). The images of sessile drop measurement on membrane cast PP surfaces are shown in Figures 4-12 and 4-13a - e. The contact angles on these surfaces were around  $150^\circ$  or above, significantly increased over the original PP sheet ( $94 \pm 0.7^\circ$ ). The high contact angle denoted that the droplet was in a Cassie-Baxter state, where a fair amount of air pockets were trapped underneath the water interface. Regarding the contact angles, the values were increased with the decrease of pore size, and they could be estimated by the Cassie-Baxter equation:  $\cos\theta_{CB} = f_s (\cos\theta_c + 1) - 1$ , where  $\theta_c$  was the intrinsic contact angle on the polypropylene sheet, and  $f_s$  was the fraction of solid area in contact with the droplet. This equation simply indicates that the less solid the droplet contacts with (or the more air the droplet contacts with), the higher the contact angle will be. It was the main reason why membrane-peeled surfaces had higher contact angles than membrane-dissolved surfaces, as a considerable number of pillars were torn down ( $\phi = 0.6$  and  $1.2 \mu\text{m}$ ) lowering the contact area. Smaller contact angle hysteresis (difference between advancing and receding angles) for membrane-peeled surfaces was also attributed to this factor, where fewer pinning sites existed to

impede the movement of contact lines. Thus, due to the high areal density of pillars for membrane-dissolved surfaces, the contact angle hysteresis was fairly large on these surfaces. This sticky effect had been previously reported on surfaces with high density nanotubes, where a strong adhesion force was generated by Van der Waals interaction between the water molecules, as with the mechanism in a gecko's foot.<sup>66</sup> This phenomenon has raised an interesting question on how to determine the superhydrophobic state. To address this, the role of contact angle hysteresis should be taken into account as the main factor. Unfortunately, the behavior of dynamic contact angle is a lot more complicated, and, unlike the Cassie-Baxter equation, a general mathematical expression has yet to be established to estimate the value.<sup>94</sup>

Despite the angle difference, the macroscopic wetting behavior of these surfaces were similar overall: water drops ( $\sim 50 \mu\text{l}$ ) falling from several centimeters easily rolled off the tilted surface ( $>10^\circ$ ) leaving the surface unwetted. The force from falling was large enough to overcome the pinning force from the pillar structure. Generally, the cast PP surfaces are considered having reasonable water repellency. For surfaces with smaller angle hysteresis ( $< 20^\circ$ ), drops bounced back after impacting the surfaces. The bouncing height increased with the increase of the hydrophobicity as less kinetic energy was transferred to the wetting surface area.<sup>95</sup>

As shown in the Chapter 3, the casting structure on  $0.6\mu\text{m}$ -peeled PP surface had a configuration very close to the hairs appearing on arthropods. This cast surface also featured exceptional hydrophobicity. Owing to the ultralow adhesion between the surface and water, the droplets were not able to be deposited on the surface during the measurement (Figure 4-13c). Furthermore, while changing the volume of the drop, no

visible difference between advancing and receding angles was found, making the determination of the hysteresis extremely difficult. As a result, another technique through captured videos was used to assess the hydrophobicity. The results and related issues are presented in the section regarding perfectly hydrophobic response.

If the cast temperature was not high enough, the lower viscosity may have hindered the filling process, making the height of the protrusions not tall enough to maintain the droplets in the Cassie-Baxter state. As shown in Figure 4-13d, a PP substrate was subjected the same casting process but at a lower temperature, 170°C. This membrane was easily peeled off, but left small bumps on the surface afterwards. Droplets on the surface were basically stuck, showing no sign of repelling water. By casting at a higher temperature, the materials flowed into the pores easily, resulting in better mechanical strength to withstand the peeling force. Some of the pillars were able to be stretched to over 50  $\mu\text{m}$  long (Figure 4-13e) and increased the contact area, which, in turn, lowered the contact angle and its hysteresis. To compare with other PP structures, I followed a renowned work published in *Science*,<sup>96</sup> where superhydrophobic surfaces were made by casting dissolved PP onto the substrate. Isotactic-PP granules were first dissolved in p-xylene at 130°C; the solution was then dip coated onto silicon substrates. The resolidified PP solution formed a porous network structure (Figure 4-13f) raising the contact angle to around 150° with contact angle hysteresis at 27°. This comparison simply showed that my current work with the high aspect ratio structure clearly was not only easier to prepare but also had better hydrophobicity.

### **LDPE substrate**

Similar to the PP substrate, the LDPE sheet had a contact angle around  $90^\circ$  (Figure 4-14a), but rather than forming high aspect ratio pillars, due to low yield strength and high percentage in elongation, the peeling process turned the LDPE surfaces into soft, thick layers of fiber-mat. Measuring contact angles of this structure also required extra care as the drops sank slightly into the mat, blurring the view of the bottom. In contrast to PP or PVDF, high density protruding structures on the  $0.6\mu\text{m}$ -peeled surface were not ripped off, but stretched to highly entangled fibers; this greatly increased the fraction of contact area and resulted in the lower contact angle of  $134^\circ$  and the higher hysteresis ( $\sim 23^\circ$ ). The  $1.2\mu\text{m}$  and  $3.0\mu\text{m}$ -peeled surfaces showed higher contact angles ( $>140^\circ$ ) and more importantly, had a low contact angle hysteresis ( $\sim 5^\circ$ ) making the surfaces extremely water repellent.

### **PVDF substrate**

The contact angle on the PVDF sheet was below  $90^\circ$  ( $\sim 81^\circ$ , Figure 4-15a), and was considered to be hydrophilic. After casting, the contact angles were increased to around  $150^\circ$ , converting the surface from hydrophilic to superhydrophobic. The contact angles were almost the same, while the contact angle hysteresis of  $1.2\mu\text{m}$ -peeled surface was 15 degrees higher than that of the  $0.6\mu\text{m}$ -peeled. The value was also higher than the PP and LDPE of  $1.2\mu\text{m}$ -peeled surfaces, which was attributed to its lower hydrophobicity nature and higher contact area of the pillar structure.

### **Perfectly Hydrophobic Response**

The contact angle was determined based on the two-dimensional image generated from a three-dimensional droplet. With the increase of hydrophobicity, the

contact area between the droplet and the substrate became smaller, making the contact angle measurement on the ultrahigh hydrophobic surfaces very challenging. Among all the cast samples, exceptional water repellency was found on the 0.6 $\mu$ m-peeled PP surfaces. The droplet could not be placed onto this hairy substrate during the measurement due to the low adhesion to water. After the droplet volume was varied and the contact angle hysteresis analyzed, the captured images revealed that the advancing and receding angles were indistinguishable in these images. Figures 4-16a and b are the images of a steel ball and a drop on the hairy surface acquired from the goniometer. The comparison showed that the contact angle of the drop was not smaller than a real sphere. This also indicated that a contact angle above 170° may not represent the actual wetting property. Gao et al.<sup>97,98</sup> have even pointed out that contact angles may not be measured accurately in the range of extreme hydrophobicity ( $\theta_c > 176^\circ$ ) if the conventional image-captured analysis is used. Alternatively, they videotaped the response of water droplets being compressed onto and decompressed from the substrate. A similar strategy was adopted here, but instead of using videotaping, the video was captured directly from the computer screen during the operation of the goniometer. It was a cost-effective method to avoid using an extra telescoped video capturing system. Figure 4-17 shows the sequential images from the contact/compress/release test of the 0.6 $\mu$ m-peeled hairy PP surface. During the test, a hung 2 $\mu$ l droplet was slightly compressed onto the surface with the advancement of the syringe, and then the syringe was slowly withdrawn from the surface. The droplet leaves the surface with no visible distortion (Figures 4-17g and h), which represents a very limited adhesion to this surface. Gao et al.<sup>97</sup> concluded that their organosilane coated

surface, named Lichao's surface, comprised of a network of 40 nm fibers, was "perfectly hydrophobic" ( $\theta_{adv}=\theta_{rec}=180^\circ$ ) based on the very similar response shown here. This process has been reproduced multiple times to establish statistical significance of the interaction between the suspended droplet and the surface. Figure 4-18 is the set of sequential images from the same test but performed on the cast PP surface having a higher contact hysteresis ( $\Delta\theta\sim 10^\circ$ ). The last two frames showed that the surface adhesion made by the droplet leaving the substrate caused a visible distortion and was clearly not a perfectly hydrophobic surface.

Another test is shown in Figure 4-19 where a water droplet was being pumped out through a metal needle. The droplet slid aside after touching the surface. The stage supporting the hairy PP film was then gently moved horizontally. Although not shown in the figure, the shape and contact interface of the droplet remained, and no change was discovered throughout the entire movement. This is ascribed to the ultralow adhesion of the hairy surface. The frames confirmed that the adhesion between the surface and the droplet was of very limited range. All these pointed out that the hairy surface created here was by far one of the best superhydrophobic surfaces within the non-chemically treated surfaces. Thus, it is believed that the current work appears to be the first report to have such extreme hydrophobicity with only structural modifications from the original substrate. The original videos can be accessed elsewhere on the Internet.<sup>99</sup>

Contact angle measurement via image analysis is generally considered to have an error range around  $\pm 3^\circ$ ,<sup>89</sup> and it can also be very subjective depending on the operator. To precisely evaluate the differences of hydrophobicity is therefore difficult when dealing with surfaces having high contact angles ( $\theta_c > 170^\circ$ ). The video assessment provides a

relatively simple solution through the investigation of interface responses. Although this technique only has a qualitative result, rather than quantitative numbers, the idea can be expanded to measure the actual adhesive force between the droplet and surface. This concept has been demonstrated to measure the force required for taking a droplet away from the surface of polystyrene nanotubes.<sup>100</sup> A droplet was suspended by a metal ring hung in a high-sensitivity microelectromechanical balance, and the force around the micron-Newton range was measured. Compared with contact angles, the amount of force measured should more accurately represent the degree of hydrophobicity.

### **Self-Cleaning Ability**

The most astonishing effect of the superhydrophobic surfaces is their self-cleaning ability, in which water droplets pick up the dirt and remove it while rolling off from the surface. This is also usually termed the *Lotus Effect* as the superhydrophobic nature of their leaves allows surface dirt to be washed off by rain or morning dew easily. Figure 4-20 schematically depicts the motion of a drop on an inclined ordinary surface and superhydrophobic surface. It is believed that dirt particles have less adhesion to topologically structured superhydrophobic surfaces and tend to adhere to the liquid interface as droplets roll off the surface (Figure 4-20b).<sup>11</sup>

Figure 4-21 is the set of sequential images showing a dirt-contaminated (carbon powder) uncast PP substrate where a few drops slid down from the surface with a very limited portion of particles being carried away. Moreover, the droplets slide very slowly and usually requires external assistance, either a largely tilted surface or a mechanical shaking. In contrast, dirt particles on superhydrophobic hairy PP surfaces were easier to be picked up and washed off by rolling beads of water (Figure 4-22). Droplets dripping

onto the contaminated surface immediately turned into black beads (Figures 4-22b and e), as dirt particles adhered to the liquid interface. Even though the dirt particles formed a thick layer on the hairy surface (Figure 4-21a vs. 4-22a), the whole cleaning process only took a few seconds with very little mechanical force involved. Although this self-cleaning has been a subject of considerable scientific interest for over a decade, compared to the efforts in making surfaces superhydrophobic, insightful studies on understanding this effect are still very rare. Important factors or relationships, such as particle size, particle hydrophobicity, and contact angle hysteresis vs. cleaning efficiency, have yet to be extensively addressed. The cast hairy surface may provide good media for the study as samples with different morphology and hydrophobicity are easy to be prepared. The samples also have adequate surface area to perform the test.

### **General Discussion**

This section aims to rationalize the hydrophobic response of the cast artificial hairy surfaces. Given a limited knowledge in fluid mechanics, I focused on delivering a qualitative explanation with a semi-quantitative expression for the liquid repellency of hairy surfaces based on my results and the findings of others.

The cuticle of water-repellent species consists of a waxy or oily substance that makes the surface contact angle above  $90^\circ$ , and the additional surface roughness enhances the hydrophobicity further to superhydrophobicity where liquid on the cuticle remains in a Cassie–Baxter rather than Wenzel state. From the animal kingdom, most water-repellent arthropods present a rough integument comprising of a thick, dense layer of microhairs. Surface roughness arises from the arrangement of hairs, while the

form and location of hair varies from species to species. Therefore many arthropods possessing hairy integument are reported to have contact angles reaching over 160°. <sup>19</sup>

The high contact angles on the 0.6 $\mu$ m-peeled PP hairy surfaces arise mainly from the small contact area with the droplet and can be easily interpreted by the Cassie-Baxter Theory (Eq. 2-9 and Table 4-2). Strong water repellency, as well as the self-cleaning feature, however, depends not so much on the high contact angle, but more on the small contact angle hysteresis. While a low interfacial area is the main criteria in water repellency, the arrangement of this artificial hairy structure seems to be another important factor for the occurrence of the ultralow adhesion observed here. The hairs created were generally a series of “I” shapes. This shape appears in almost all water-repellent arthropods having a hairy exterior. Although the size and density of the hairs vary among different species, this geometry may benefit the water repellency in some ways.

First, all the natural hairs of water-repellent arthropods are inclined at a certain angle to their cuticle (~30° of strider’s leg and ~30°- 45° of our cast surface). Assuming a droplet on a uniform array of pillars maintains a CB state, then the contact angle hysteresis can be simply expressed as: <sup>38</sup>

$$\Delta\theta = \lambda_p (\Delta\theta_0 + \omega) \quad (4-2)$$

where  $\lambda_p$  is the linear fraction of the contact line and can be treated as a size to spacing ratio (=d/L, Figure 4-23a);  $\omega$  is the inclined angle to the substrate of the individual pillars, and  $\theta_0$  is the intrinsic contact angle hysteresis of the pillars’ materials. According to the equation, the contact angle hysteresis is decreased by decreasing the size to spacing ratio of the pillars, but increased with the increase of the tilted angle. This may increase

the retention force of the contact line and generate more thrust for water-walking species.<sup>16</sup> It may, however, increase the difficulty of shedding droplets as well. Note that the model assumes the contact line migrates on the top, flat area of the pillars, which is far from the case for hair tips.

On the other hand, when the layer of hair comes in contact with a liquid, the liquid interface is suspended by the hairs with a pressure difference. The pressure required (impregnation pressure) to force liquid through various arrangements of pillars has been calculated.<sup>51,65</sup> The calculation revealed that the required pressure is increased by decreasing the spacing of the array ( $L$ ). In addition, the results showed that the array of tilted pillars increased the impregnation pressures since the free space between the pillars was reduced, making tilted pillars favorable to resisting water. A horizontal array of cylindrical pillars was also considered (Figure 4-23b), and it was concluded that such an arrangement may provide greater water resistance. Liquid that penetrated between the horizontal pillars needed to wet the maximum surface area and required maximum surface energy. Overall, compared to simple vertical or inclined pillar arrays, it is energetically unfavorable for a liquid to intrude between the pillars parallel to the interface. Most of the hairs of natural species and our cast surfaces are not only inclined but curled with their tips parallel to the bodies, which in turn provides a greater resistance to wetting.

Another crucial role of the hairs is the mechanical response to the liquid interface. This response was previously considered in plastron respiration, in which the submerged insects breathe the oxygen from a layer of air maintained by their hairy integument.<sup>17,18,51</sup> The curvature pressure and the mechanical strength of hairs sustain

the interface, while higher ambient hydraulic pressure may buckle the hairs causing the collapse of the plastron air. Earlier observations found that the collapse for most insects occurred in the pressure between 1 to 5 atm. With newer and better imaging equipment, a calculation, however, estimated that the hairs should be stable at a pressure up to 40 atm,<sup>18</sup> indicating the bald patches of the cuticle may be responsible for the failure. In terms of the dynamic behavior, this has not been extensively studied. A recent study showed the hairs on water-walking insects can be bent during the interaction with the liquid interface. This flexibility associated with the second scale of roughness on the hairs reduced the contact force while performing locomotion.<sup>57</sup> Another newly published work revealed the hierarchical design of the anti-wetting termite wings, in which the longer hairs (~30 $\mu$ m long and 2 $\mu$ m wide) and the shorter star-shaped structure (~5 $\mu$ m high and 5 $\mu$ m wide) serve to repel macro and micro droplets, respectively. Macro droplets are mainly supported by longer hairs causing the hairs to deflect, and transfer the kinetic energy to elastic energy. The mechanism may also contribute to the extremely hydrophobic response of the artificial hairy surfaces.

Considering how a droplet rolls on the hairy structure, the solid-liquid interface would advance and retreat upon the hairs if the energy barriers of interface pinning were overcome (Figures 4-24a and b). The hairs in contact with the liquid may also be deflected. Rather than wetting more surface area, the kinetic energy is transferred into potential energy (Figures 4-24c and d). This interaction with the flexible hairs would prevent the further intrusion of liquid between hairs and allow the contact area fraction to be minimized during the motion of droplets. The adhesion force also remains at the lowest level. The hypothetical mechanism proposed requires further examination, such

as with computational modeling or microscopy techniques, in order to reveal the interaction on the interface. Although studies on the dynamic role of the flexibility of hairs and hydrophobicity are still very limited, the principle may yield a new route for the fabrication of superhydrophobic surfaces.

In addition to the geometrical factor, the surface chemistry should be taken into account. The PP substrate contained a methyl side group, which is considered highly hydrophobic. The nanofiber structure has been shown to enhance hydrophobicity because the hydrophobic portion of the molecule chain tends to be exposed to air, enhancing the surface hydrophobicity.

### **Summary**

The wetting property of natural and cast surfaces was characterized by measuring contact angles. Although contact angle measurement with goniometer has been widely used, few important issues should be taken into careful consideration to lower the subjectivity. Droplets on hairy leaves, Lady's Mantle, showed contact angle at  $180^\circ$  while the contact angle hysteresis was relatively large. The hydrophobicity imply comes from the strong pinning of contact lines rather than elastic response of the hairs. Contact angles of all the cast surfaces were significantly increased over their original flat sheet. The high contact angle denotes the droplet is in Cassie-Baxter state, where a fair amount of air pockets were trapped underneath water interface. The value of contact angles was generally increased with the decrease of membrane pore size, and they can be estimated by Cassie-Baxter equation.

Remarkable water repellency was found on  $0.6\mu m$ -peeled PP hairy surfaces showing no contact angle hysteresis. Video assessment confirmed that the PP hairy

surfaces is perfectly hydrophobic ( $\theta_{adv}=\theta_{rec}=180^\circ$ ), and is by far one of the best super-hydrophobic surfaces within those non-chemically treated surfaces. The confirmation of natural and artificial hairs (inclined and curled with their tips parallel to the bodies) provides a greater resistance to wetting. A possible mechanical response to the liquid interface where hairs are deflected to avoid the further wetting is another important factor lowering the contact angle hysteresis. Related studies addressing the relationship between elastic materials and hydrophobicity are still rare, and the mechanism needs further examination with either computational simulation or imaging technique.

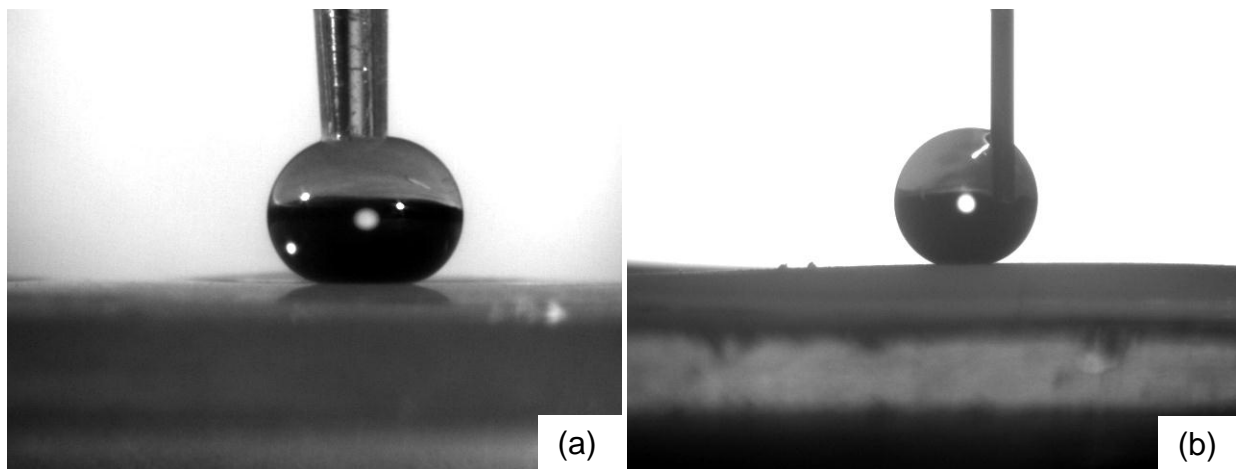


Figure 4-1. Contact angle measurement on a superhydrophobic surface with different diameters of syringe. (a) a larger plastic syringe, and (b) a narrower, 30-gauge, metal needle.

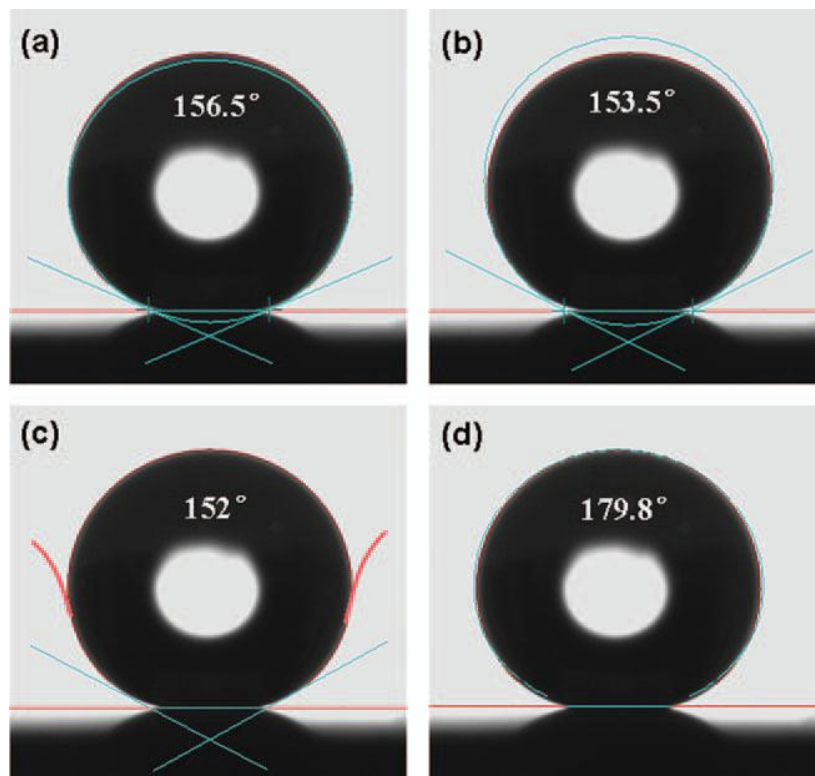


Figure 4-2. Images of the same water droplet on a superhydrophobic surface under different fitting modes of the static contact angle: (a) ellipse fitting; (b) circle fitting; (c) tangent searching; (d) and Laplace-Young fitting. The figures include the simulation lines of the shape of the water droplets and the horizontal baselines. (reproduced by permission of The Royal Society of Chemistry.)

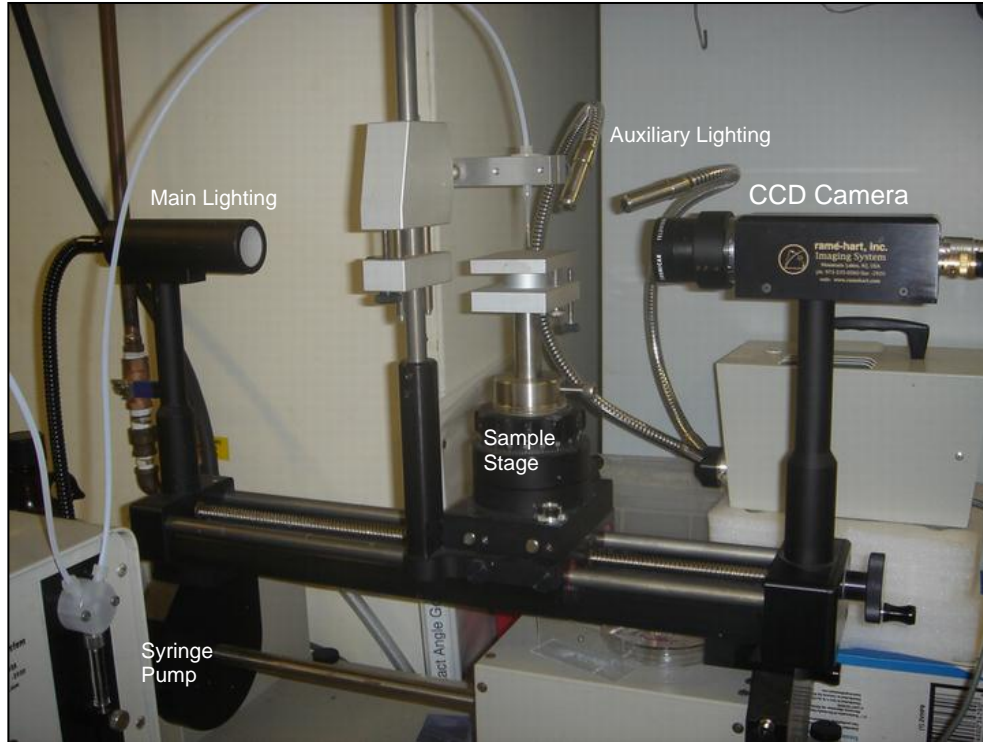


Figure 4-3. The equipment set-up of goniometer, where the droplet was loaded by a syringe pump and placed on the sample surface. The image was later captured by the CCD camera connected to the controlling program.

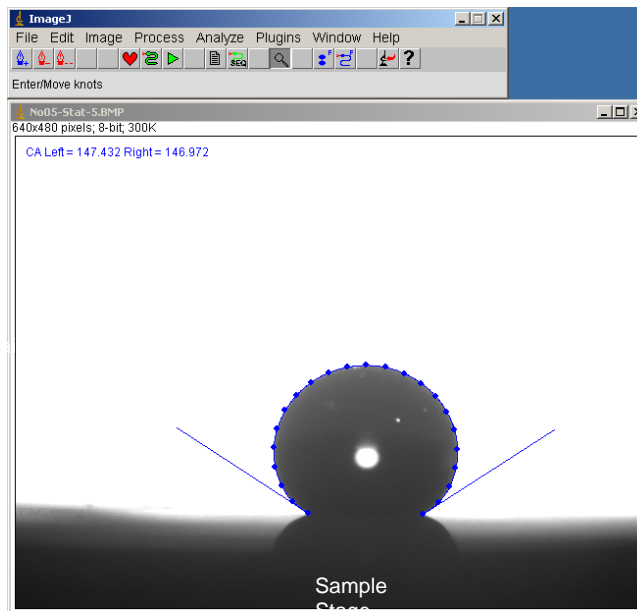


Figure 4-4. The interface of DropSnake program. The value of contact angle was determined by fitting the contour of the whole drop and polynomial-fitting of the interfacing area.

Table 4-1. Measured surface tensions of the liquids used in contact angle measurement.

Liquid	Surface Tension (mN/m)	Liquid	Surface Tension (mN/m)
Water	72.8	Hexdecane	27.6
Oliver oil	34.6	Octane	21.8
Water-Methanol (MeOH vol%)			
0.00	72.8	29.41	44.1
2.24	67.8	35.53	41.4
4.71	62.9	45.45	37.8
6.66	62.5	55.75	34.5
7.39	59.7	65.41	31.8
12.67	55.0	74.83	28.9
17.84	51.3	80.71	25.2
23.81	47.7	100.00	22.3

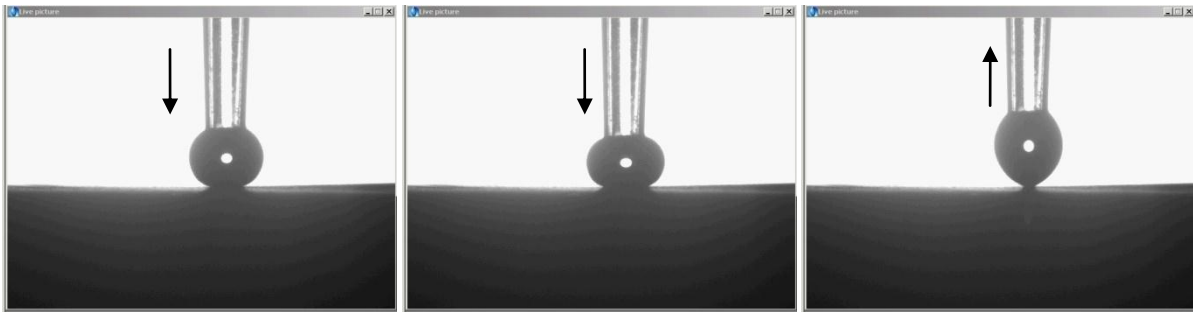


Figure 4-5. Selected sequential images during contact/compression/release test on a superhydrophobic surface. The last frame shows the droplet left the substrate with a visible distortion.

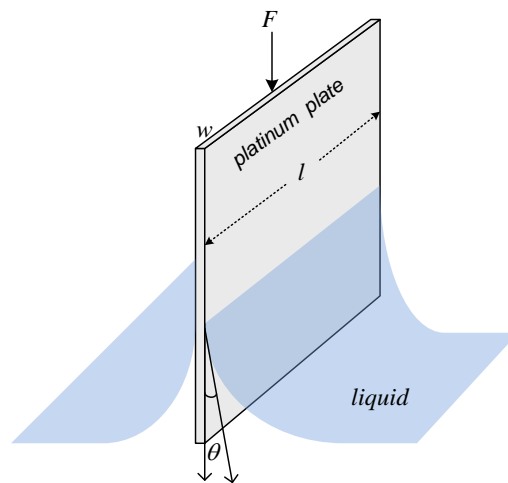


Figure 4-6. Schematic picture of Wilhelmy plate method of measuring liquid surface tension.

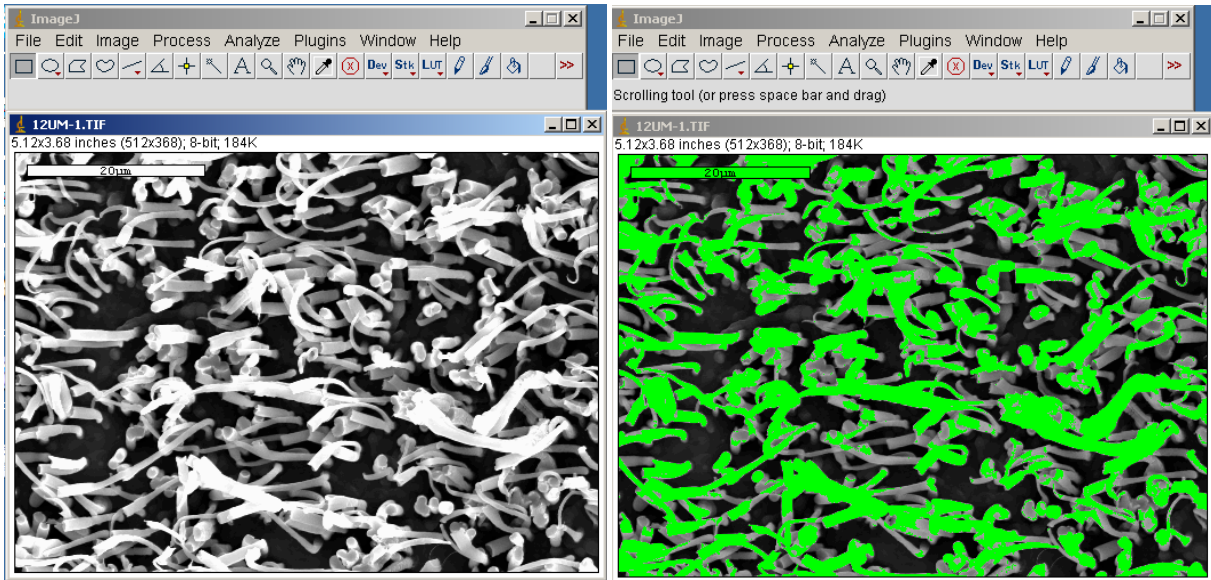


Figure 4-7. The fraction of contact area is estimated by adjusting the threshold of top-view SEM pictures.

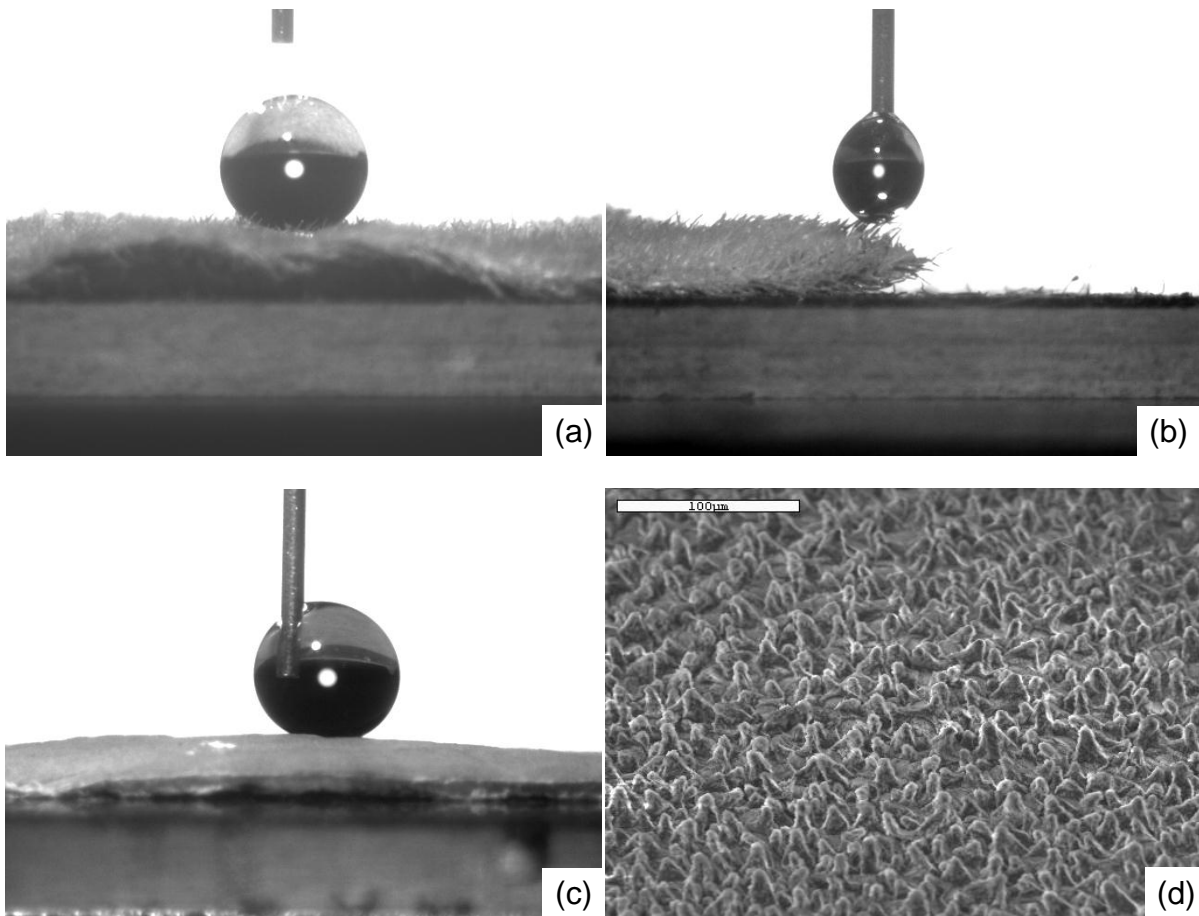


Figure 4-8. (a) Droplet formed a perfect sphere on Lady's Mantle, (b) hairs of lady's mantle impede the droplet being pulled, (c) droplet on the Lotus leaf, and (d) the microstructure of Lotus leaves.

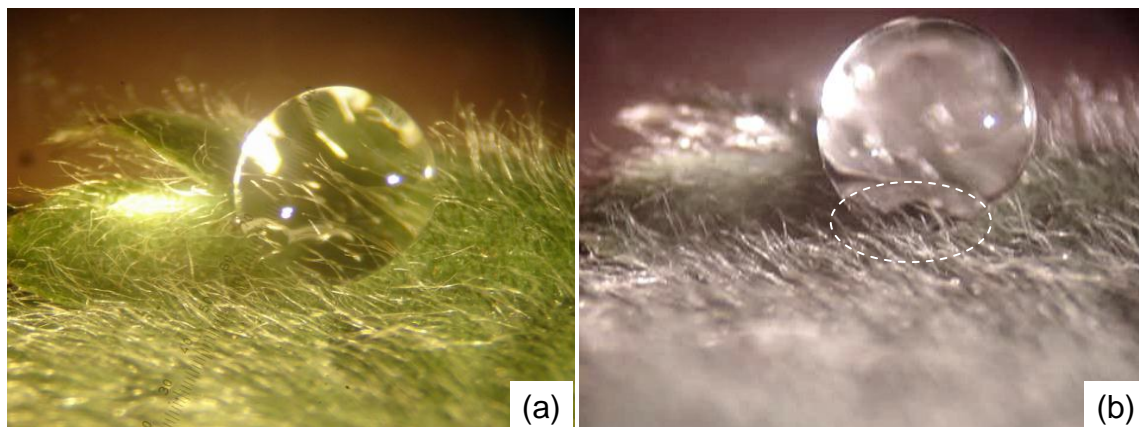


Figure 4-9. Images under stereo microscope. (a) A droplet on Lady's Mantle leaf, and (b) hairs in contact with the droplet are rarely deflected by the interface.

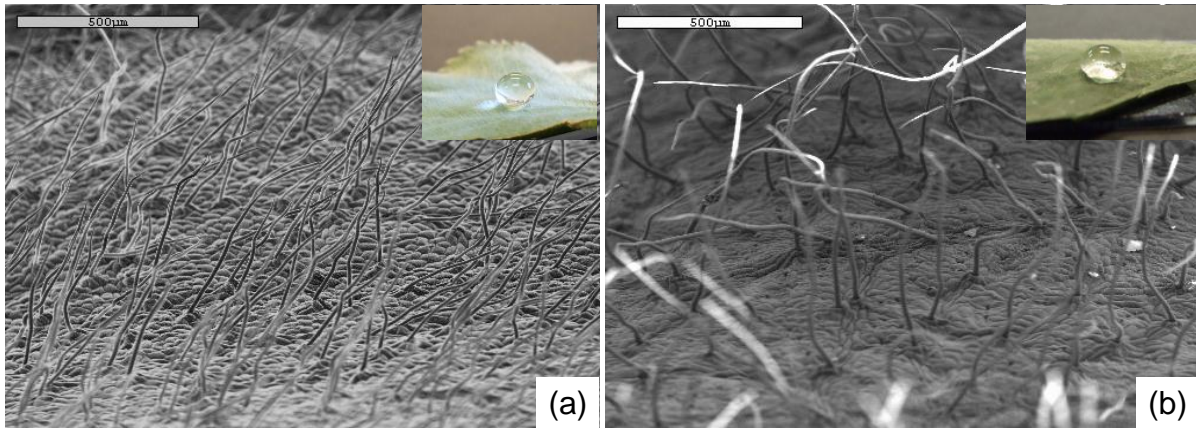


Figure 4-10. Two types of Lady's Mantle leaves. (a) Higher contact angles on dense and ordered hairs. (b) Lower contact angles on random oriented hairs.

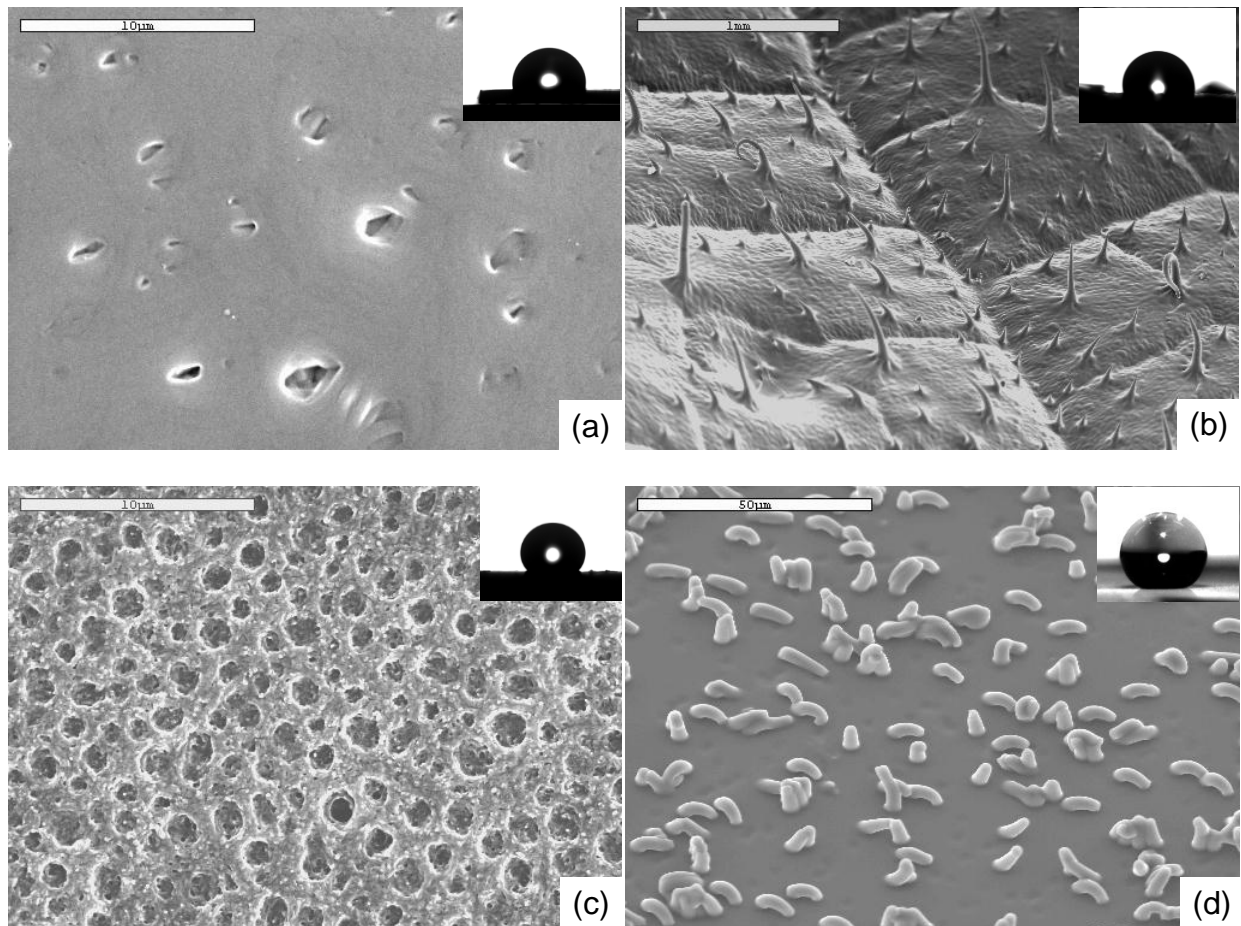


Figure 4-11. Morphology of different cast PDMS surfaces and their contact angles. (a) intrinsic PDMS surface, (b) leaf-cast PDMS surface, (c) membrane-dissolved PDMS surface (pore size= $0.6\mu\text{m}$ ), and (d) membrane-peeled PDMS surface (pore size= $3.0\mu\text{m}$ ). The contact angle is increased with the surface roughness

Table 4-2. Contact angles of all the cast thermoplastic surfaces and the theoretical contact angles calculated from Cassie-Baxter theory. (Eq. 2-9)

PP (Polypropylene)						
Pore Size	Contact Angle ( $\theta_c$ )	Advancing Angle ( $\theta_{adv}$ )	Receding Angle ( $\theta_{rec}$ )	Contact Angle Hysteresis <sup>a</sup> ( $\Delta\theta$ )	Estimated Contact Area Fraction ( $f_s$ )	Cassie-Baxter Contact Angles ( $\theta_{cb}$ )
Original sheet	94 ± 0.7°	98 ± 2.1°	75 ± 2.6°	23°	-	-
Membrane-dissolved						
0.6 $\mu m$	155 ± 3.6°	161 ± 3.7°	147 ± 3.1°	24°	0.11 ± 0.03	154.1° ± 3.7°
1.2 $\mu m$	153 ± 3.6°	159 ± 4.9°	111 ± 3.1°	48°	0.17 ± 0.02	147.8° ± 1.51°
3.0 $\mu m$	147 ± 1.9°	169 ± 1.6°	113 ± 6.3°	56°	0.23 ± 0.01	141.8° ± 0.9°
Membrane-peeled						
0.6 $\mu m$	>170°	>170°	>170°	<1°	0.02 ± 0.01	169.3° ± 2.9°
1.2 $\mu m$	157 ± 3.8°	160 ± 4.3°	152 ± 3.1°	8°	0.15 ± 0.04	150.1° ± 4.3°
3.0 $\mu m$	152 ± 4.0°	162 ± 2.5°	145 ± 4.4°	17°	0.21 ± 0.03	143.6° ± 2.7°
0.6 $\mu m$ membrane-peeled						
170°C cast	134 ± 5.5°	138 ± 6.3°	91 ± 6.4°	47°		
200°C cast	163 ± 4.2°	164 ± 1.8°	154 ± 4.8°	10°		
Dissolved-resolidified	151 ± 4.2°	162 ± 4.7°	135 ± 4.0°	27°		
LDPE (Low-density Polyethylene)						
Pore Size	Contact Angle ( $\theta_c$ )	Advancing Angle ( $\theta_{adv}$ )	Receding Angle ( $\theta_{rec}$ )	Contact Angle Hysteresis <sup>a</sup> ( $\Delta\theta$ )	Estimated Contact Area Fraction ( $f_s$ )	Cassie-Baxter Contact Angles ( $\theta_{cb}$ )
Original sheet	91 ± 2.3°	93 ± 1.3°	70 ± 4.6°	23°	-	-
0.6 $\mu m$	134 ± 4.0°	150 ± 4.2°	127 ± 2.5°	23°	0.36 ± 0.04	130.4° ± 3.0°
1.2 $\mu m$	154 ± 5.7°	159 ± 4.5°	152 ± 2.6°	7°	0.31 ± 0.06	134.3° ± 4.8°
3.0 $\mu m$	141 ± 2.3°	151 ± 3.2°	146 ± 3.5°	5°	0.24 ± 0.04	140.0° ± 3.6°
PVDF (Polyvinylidene Fluoride)						
Pore Size	Contact Angle ( $\theta_c$ )	Advancing Angle ( $\theta_{adv}$ )	Receding Angle ( $\theta_{rec}$ )	Contact Angle Hysteresis <sup>a</sup> ( $\Delta\theta$ )	Estimated Contact Area Fraction ( $f_s$ )	Cassie-Baxter Contact Angles ( $\theta_{cb}$ )
Original sheet	81 ± 1.6°	82 ± 0.5°	42 ± 5.1°	38°	-	-
0.6 $\mu m$	152 ± 2.7°	159 ± 2.9°	133 ± 5.8°	26°	0.13 ± 0.02	148.9° ± 3.2°
1.2 $\mu m$	147 ± 1.8°	153 ± 2.0°	112 ± 5.3°	41°	0.23 ± 0.02	137.8° ± 2.5°

a. This angle was the difference between the mean value of advancing angle and receding angle.

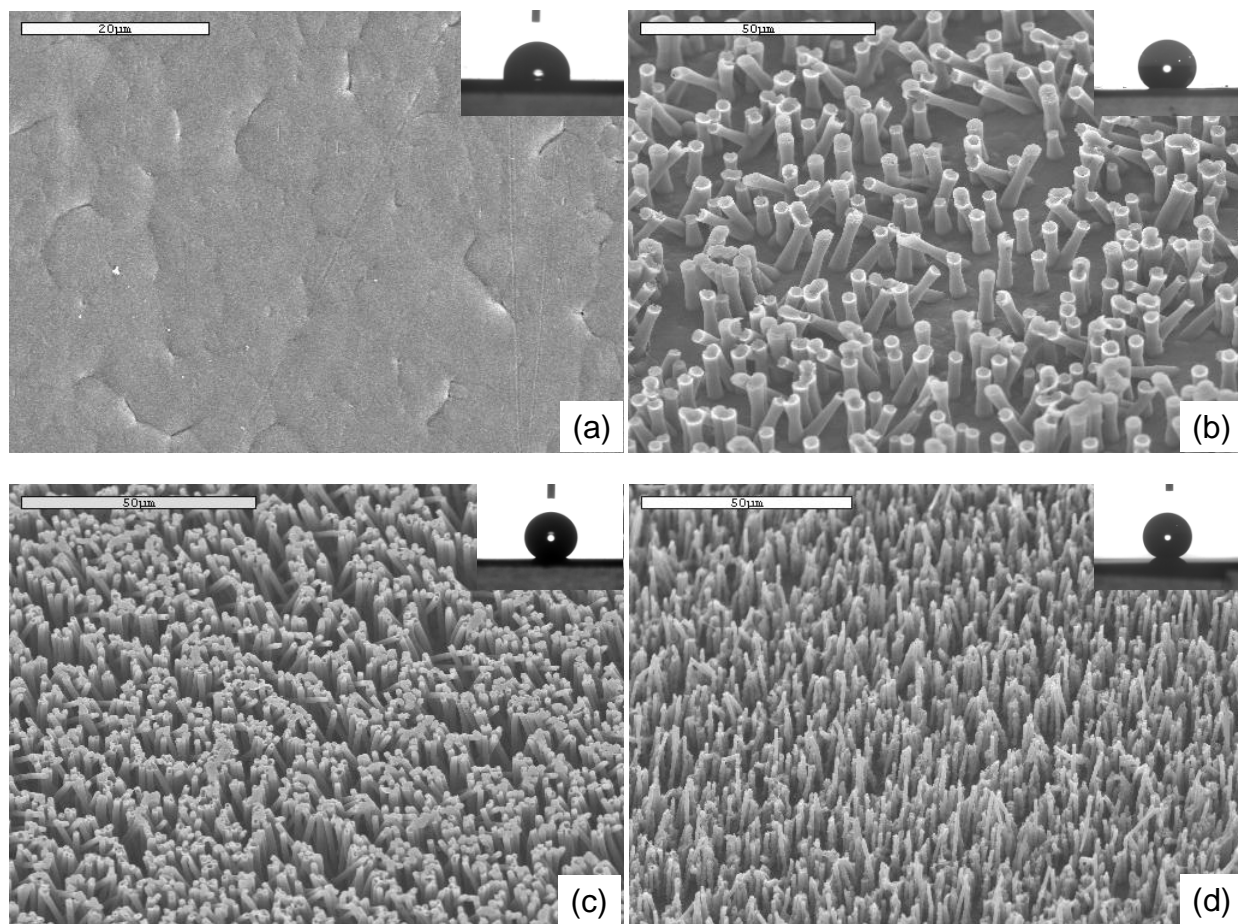


Figure 4-12. The surface morphology of the membrane-dissolved PP surfaces and their sessile drop images. (a) original PP sheet. The membrane pore size is (b)  $3.0 \mu\text{m}$  (c)  $1.2 \mu\text{m}$  and (d)  $0.6 \mu\text{m}$ .

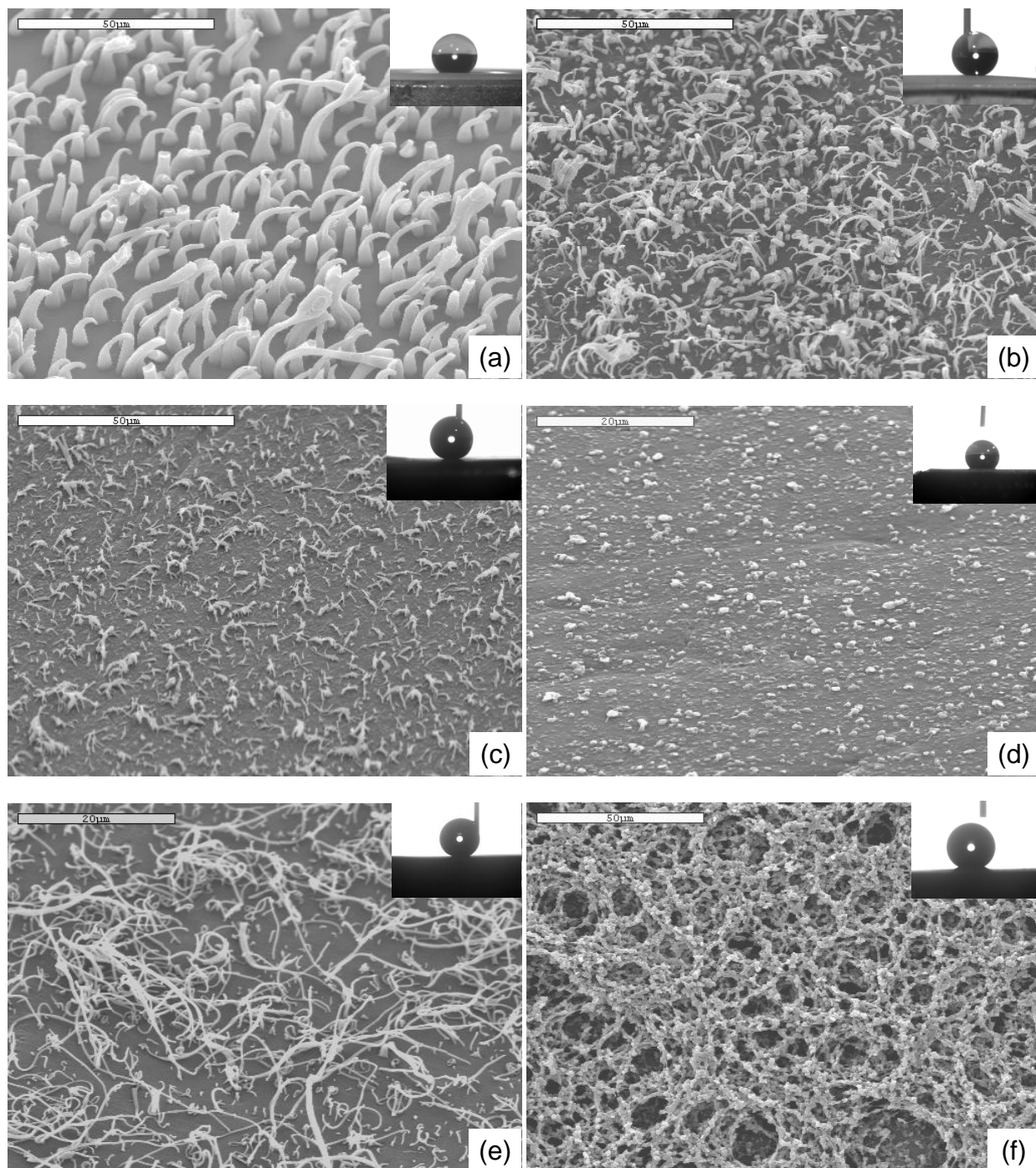


Figure 4-13. The surface morphology of the membrane-peeled PP surfaces and their sessile drop images. The membrane pore size is (b)  $3.0 \mu\text{m}$  (c)  $1.2 \mu\text{m}$  and (d)  $0.6 \mu\text{m}$ . (d) and (e) are  $0.6 \mu\text{m}$ -peeled surface cast at  $170^\circ$  and  $200^\circ$ , respectively. (f) Si substrate dip-coated with i-PP solution.

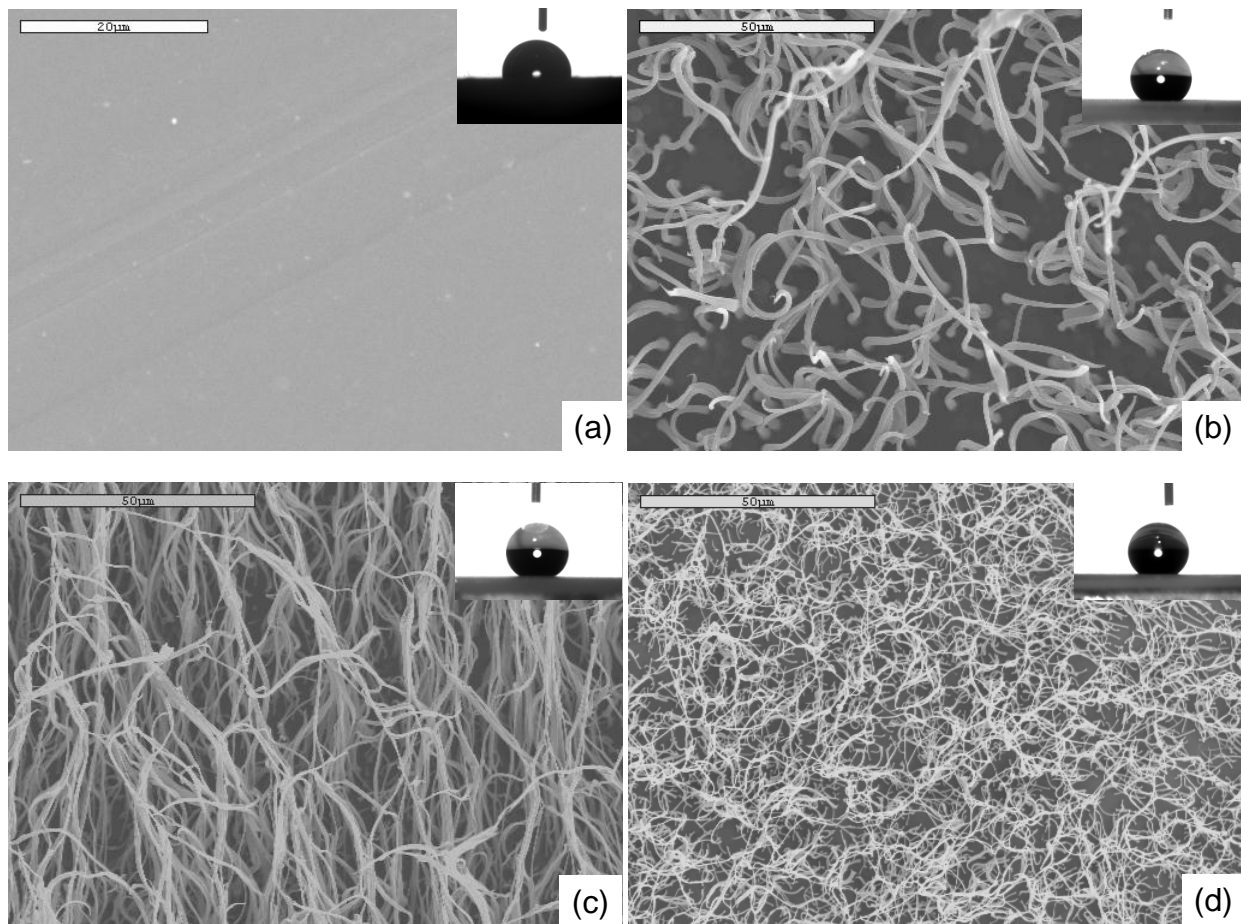


Figure 4-14. The surface morphology of the membrane-peeled LDPE surfaces and their sessile drop images. (a) original LDPE sheet. The membrane pore size is (b)  $3.0 \mu m$  (c)  $1.2 \mu m$  and (d)  $0.6 \mu m$ .

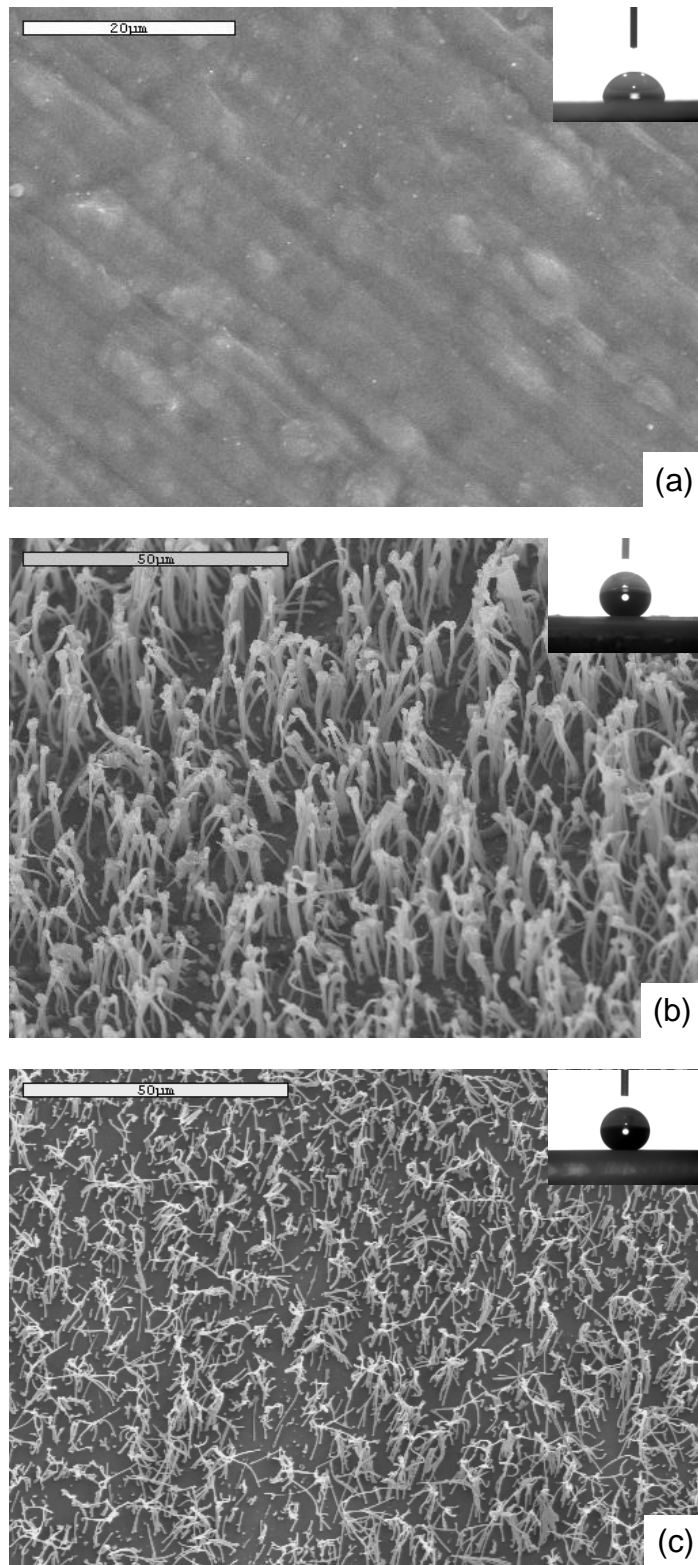


Figure 4-15. The surface morphology of the membrane-peeled PVDF surfaces and their sessile drop images. (a) original PVDF sheet. The membrane pore size is (b)  $1.2 \mu\text{m}$  and (c)  $0.6 \mu\text{m}$ .

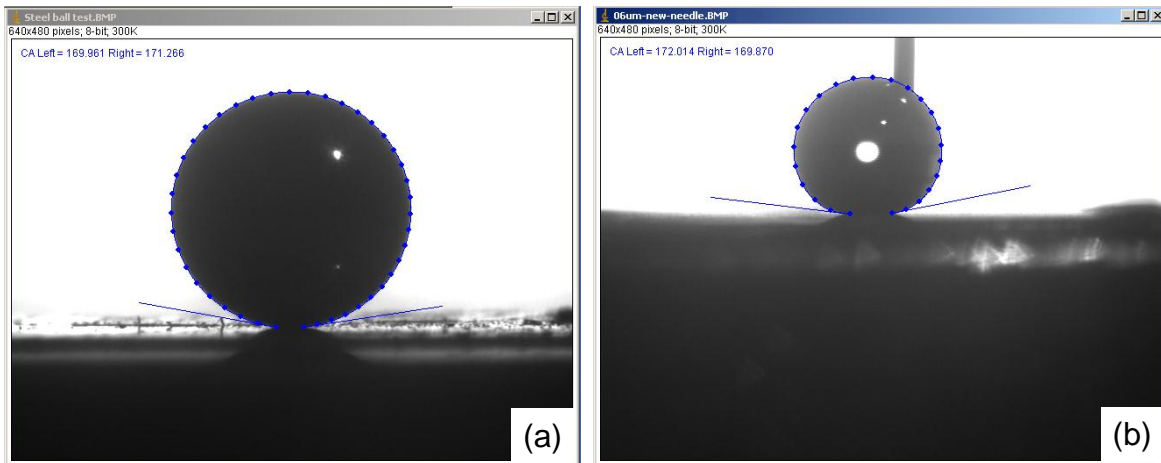


Figure 4-16. The images of contact angle measurement acquiring from goniometer. (a) a steel ball and (b) a droplet on cast PP hairy surface.

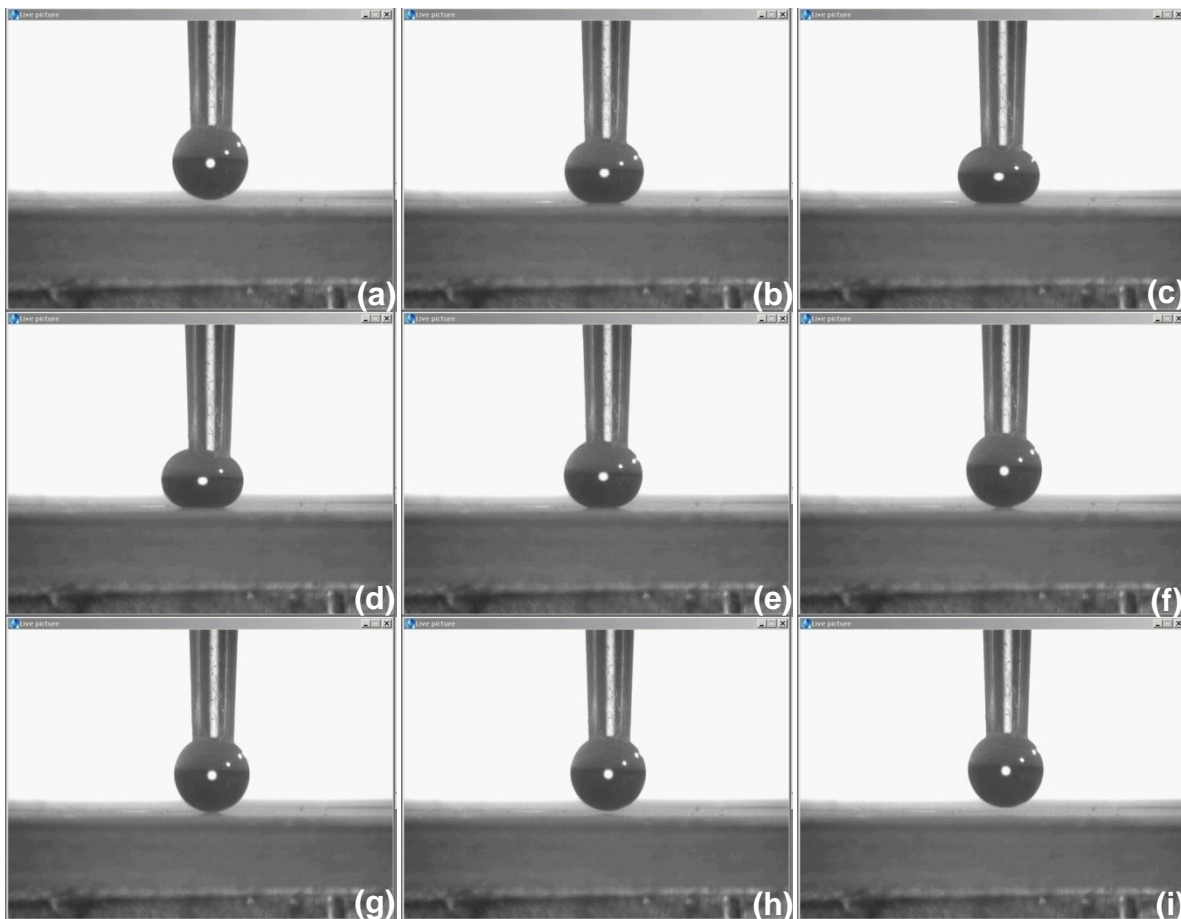


Figure 4-17. Selected images during contact/compression/release test on  $0.6\mu\text{m}$ -peeled hairy PP substrate. The last three frames show the droplet left the substrate without a visible distortion, and the response represents the surface is nearly perfect-hydrophobic.

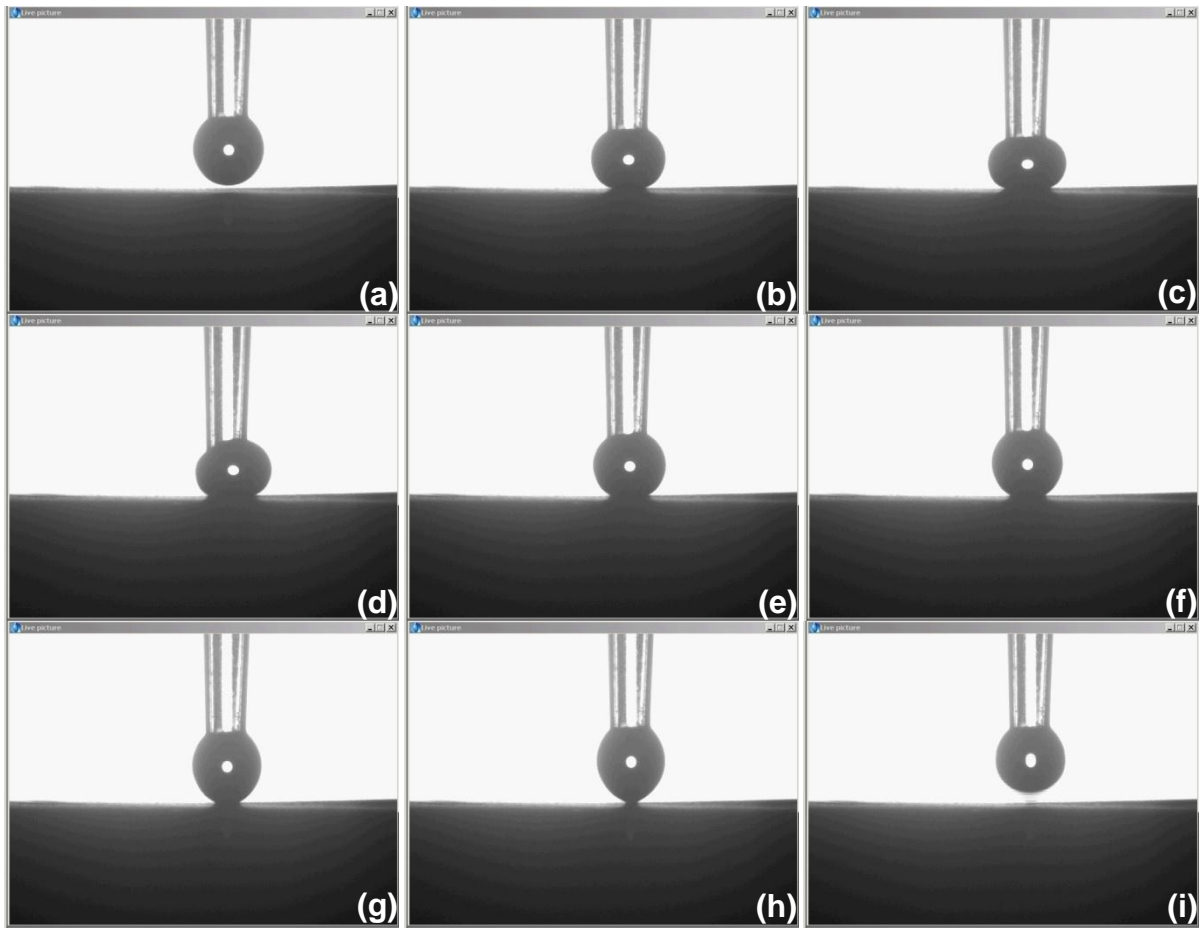


Figure 4-18. Selected images during contact/compression/release test on  $0.6\mu\text{m}$ -peeled PP substrate (cast at  $200^\circ\text{C}$ ). The last two frames show the droplet left the substrate with a visible distortion, and is apparently not a perfectly hydrophobic surface.

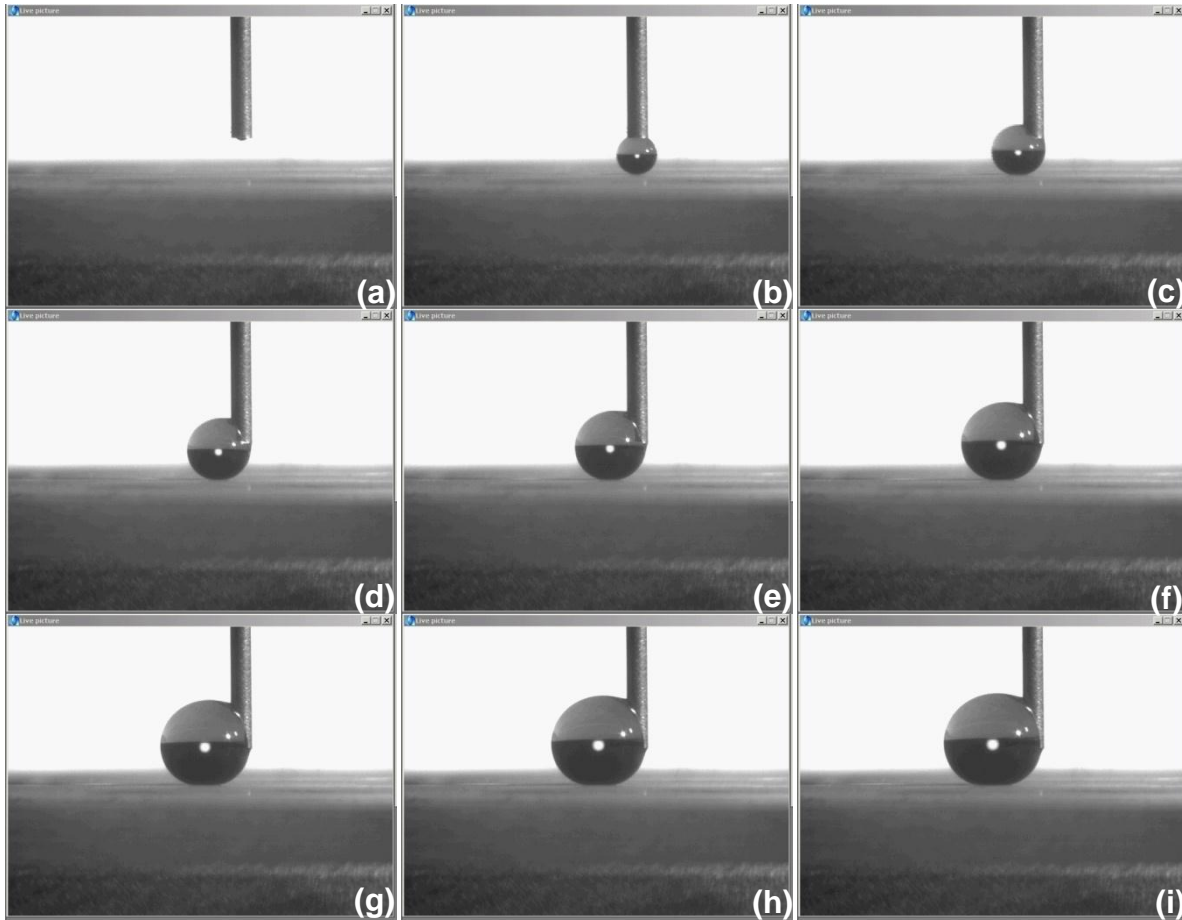


Figure 4-19. Selected images during motion test on  $0.6\mu\text{m}$ -peeled hairy PP substrate. A water droplet slid aside after touching the surface while water was being pumped out through a metal needle. The shape and contact interface of the droplet remained and no change was discovered.

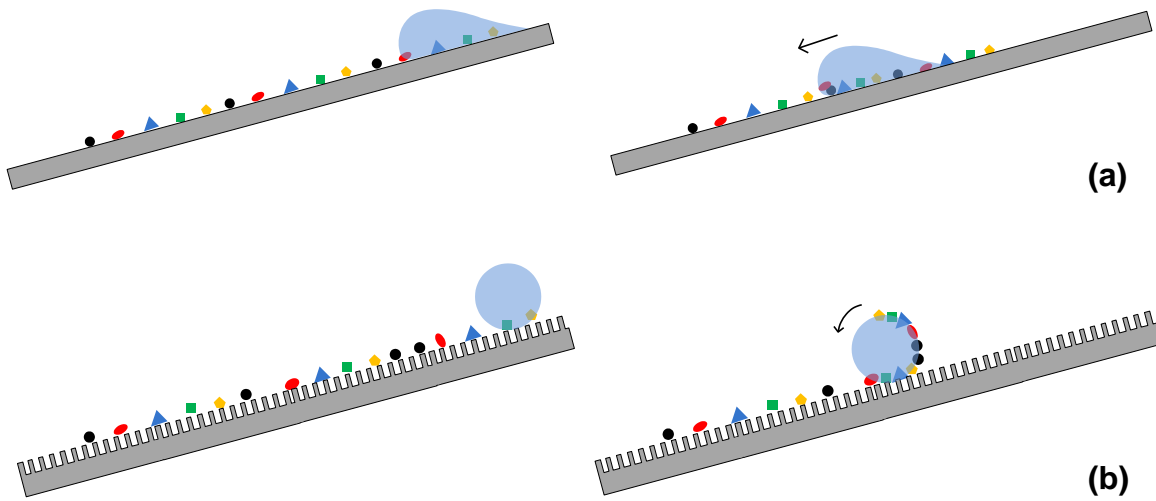


Figure 4-20. (a) Drop slides on an ordinary hydrophobic surface hardly carrying away dirt particles. (b) A drop rolls on a superhydrophobic surface picking up most dirt particles.

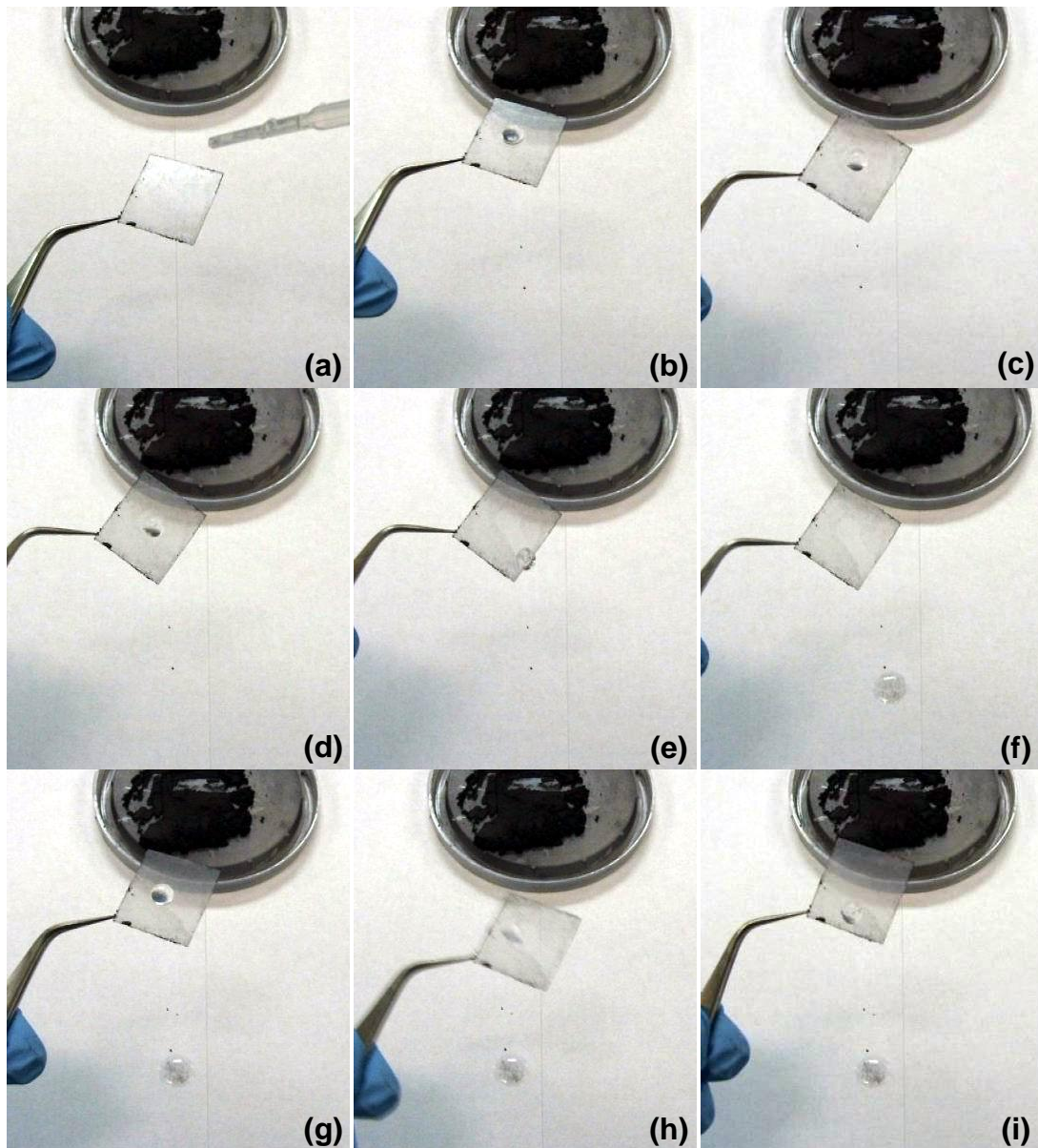


Figure 4-21. Water droplets on an uncast PP sheet contaminated by carbon powder. From (a) to (f), the droplets slide down slowly from the surface if the tilted angle is large enough. A very limited portion of dirt particles was washed out with the droplets.

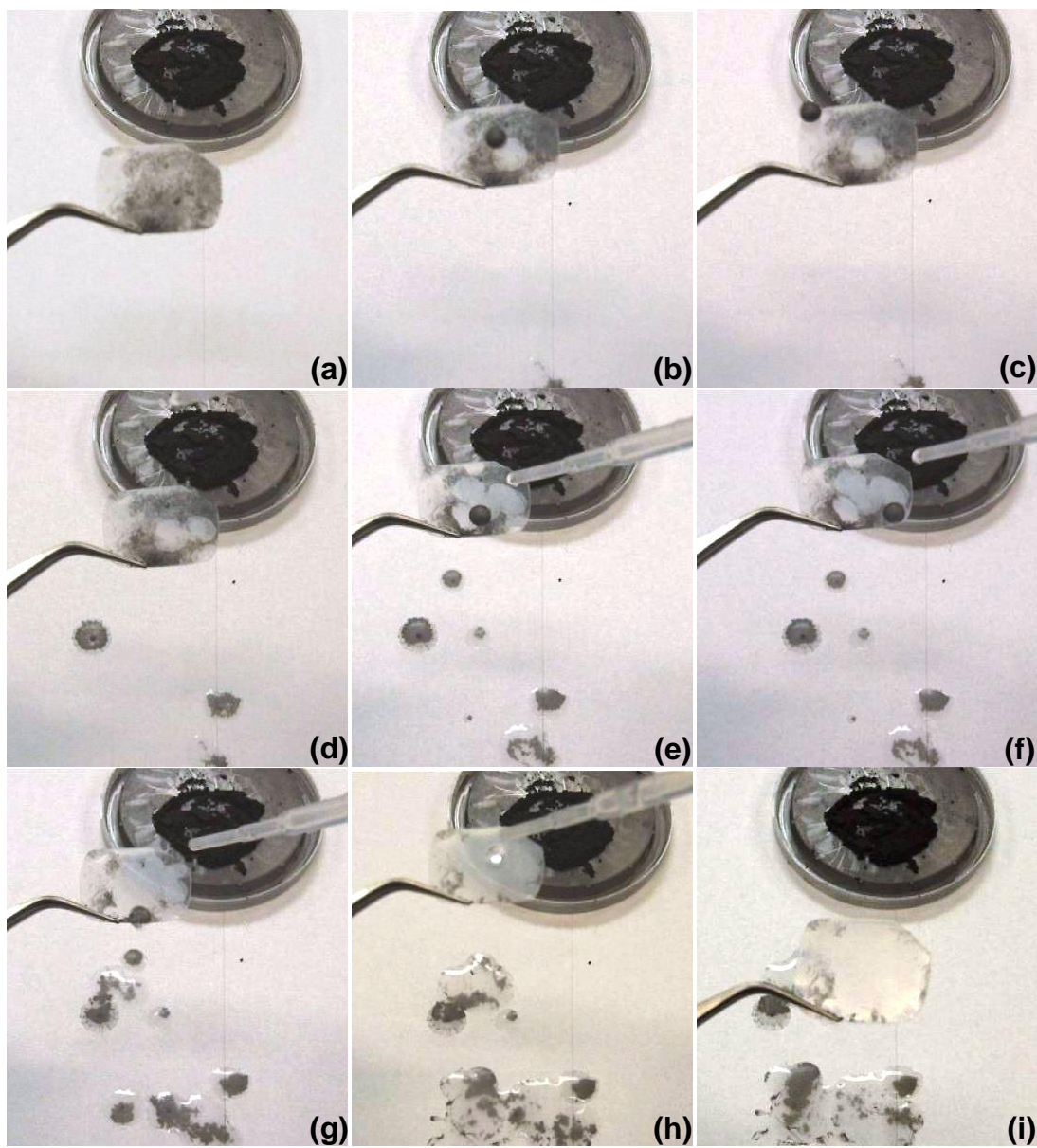


Figure 4-22. Water droplets on a cast hairy PP surface contaminated by dirt particles. From (a) to (i), the droplets were formed beads and rolled off from the surface effortlessly. The surface demonstrates the self-cleaning ability where the dirt particles were effectively washed out with the droplets rolling.

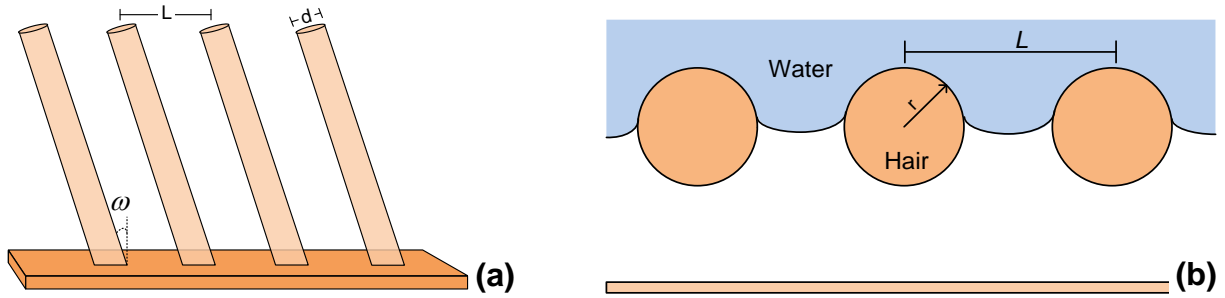


Figure 4-23. Two configurations of models for water-repellent hair pile. (a) A uniform array of pillars titled at an angle. (b) An array of horizontally aligned cylindrical hairs which suspend water interface.

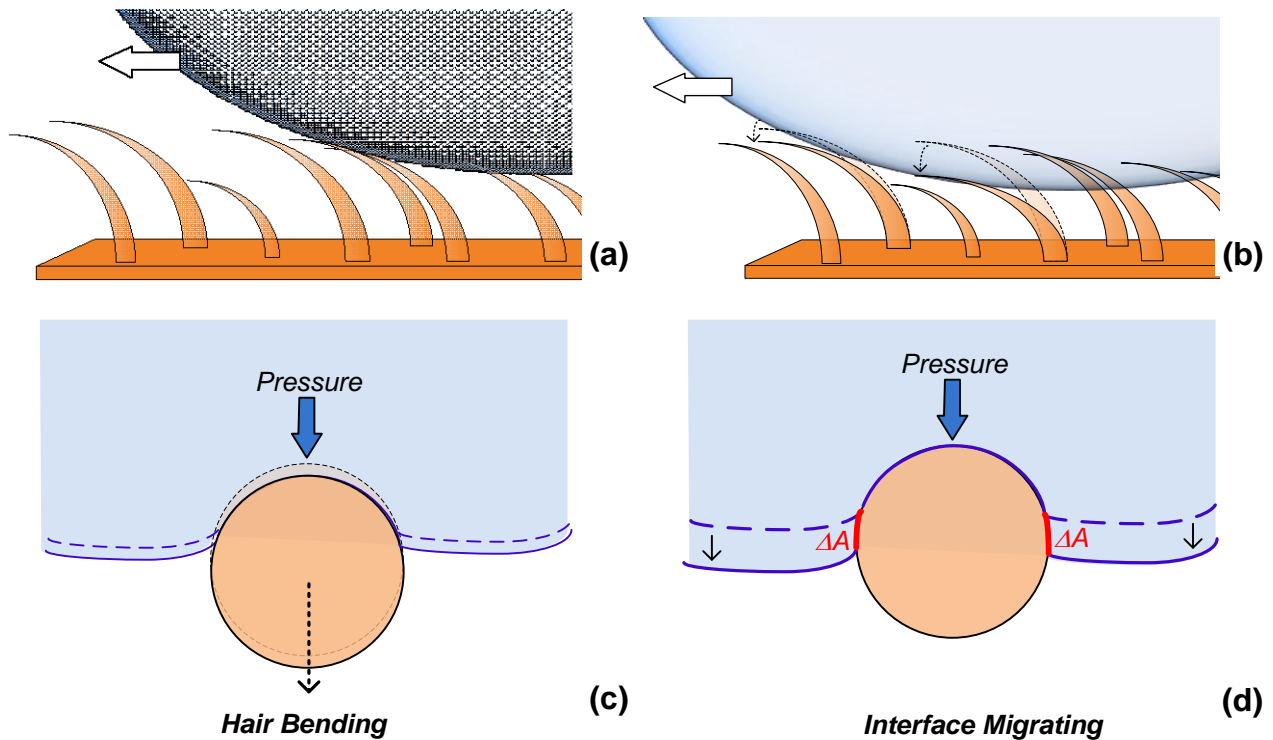


Figure 4-24. (a) and (b) the motion of a droplet on the hairy surface causing the deflection of hairs. (c) hair bending under hydraulic pressure resulting in very little or no change in wet area, (d) stiffer hairs under hydraulic pressure resulting in the increase of wet area.

## CHAPTER 5 TOWARDS SUPEROLEOPHOBIC SURFACES

This chapter aims to extend the cast surfaces to oleophobic (oil-repellent) region. Since most organic liquids or oil have much lower surface tensions (20-30 mN/m), therefore making a surface oil repellent is a great challenge in engineering level. An additional surface treatment of the surface is essential to render superhydrophobic surfaces into oleophobic or *super-oleophobic*. Plasma surface treatment was used as the main tool for surface modification. The chapter starts with experimental work where two different plasma systems were introduced, a home-constructed and a commercial system. The resulting structure and their contact angles are presented at the second section. While the results showed the oil contact angle of the surfaces treated with fluorocarbon compound can be significantly increased, strong oil repellency or super-oleophobicity was not able to be obtained on these hairy surfaces.

### **Experimental Work of Plasma Treatment**

#### **Introduction**

Surface treatment by means of plasma is an effective technique for many bulk materials.<sup>101</sup> One of the special interests is growing in manipulating the degree of surface hydrophobicity. Plasma is usually considered the fourth state of matter, comprised of highly excited atoms, molecules, ions, and radical species; these are typically generated by exciting gas molecules into energetic states with different sources, such as radio frequency (RF) electric fields, microwaves, or electrons from a hot filament discharge. The electromagnetic fields accelerate the electrons to impact the molecules, which in turn results in the excitation of atoms and ions, dissociation of gas molecules, and production of more electrons. Therefore, plasma is a highly unbalanced

and reactive chemical environment in which the high-density of ionized and excited species can promote chemical reactions and change the surface properties of normally inert materials. The materials used for casting hairy structures, polypropylene, polyethylene, and polyvinylidene fluoride, are considered to have relatively inert surfaces where the absence of reactive sites (e.g.,  $-\text{OH}$  or  $-\text{NH}_2$ ) makes it difficult for them to couple with other chemical groups. Plasma treatment is practicable and can introduce radicals or reactive functional groups to the polymer surface through ion bombardment and UV radiation; this enhances the corporation with other new species.

Two opposite routes were applied to test the possibility of enhancing oil repellency: (1) to increase the surface hydrophilicity and (2) to increase the surface hydrophobicity. To increase the hydrophilicity, the surface was treated with water plasma to induce more hydroxyl groups on the surface. To increase the surface hydrophobicity, the surface was coated with a fluorocarbon ( $\text{CF}_x$ ) layer using commercial equipment. Using the Inductive Coupled Plasma (ICP) Deep Reactive Ion Etching (DRIE), a fluorocarbon compound was deposited as a passivation layer during an etching process. The fluorocarbon family is known for having low surface energy and hydrophobic behavior, such as Teflon. DRIE, originally designed for creating high aspect ratio surface structures, provides a stable environment and effective way for performing the plasma deposition of CF compounds.<sup>102,103</sup>

### **Surface Treatment with Water Plasma**

Water plasma treatment was carried out by a home-assembled plasma system at Dr. Eugene Goldberg's lab in materials science department, Univeristy of Florida. The layout of the system was schematically showed in Figure 5-1. Plasma was generated through Radio Frequency Glow Discharge (RFGD) at 13.56 MHz in a modified bell jar

with a copper coil to carry the current (RF Plasma Products, Inc). The chamber vacuum was maintained by a mechanical pump. Samples were placed in the bell jar till the pressure was below 100 mTorr for 10 minutes. Argon was then purged into the chamber at 1000 sccm for 3 times, and then turn on the RF power to generate the plasma at 50 Watts to pre-clean the chamber for 5 minutes.

The source of water vapor was simply provided by connecting a bottle of DI water into the gas tube. Water vapor was then introduced into the chamber and then purged for 3 times. After purging, pressure was kept at 100 mTorr and plasma was generated by adjusting RF power with incident power at around 50 W and reflected power at 25 W. During treatment water vapor was continuously flowed into the chamber, and adjusted to have a stable plume. Cast hairy samples were placed ~3.5 inches below RF coil (Figure 5-2). The duration of plasma treatment was from 1 minute to 5 minutes. After plasma treatment, the samples were immediately tested with distilled water, and other organic liquid to have preliminary results.

### **Surface Treatment with Fluorocarbon Plasma Deposition**

Fluorocarbon coating was deposited by using deep reactive ion etching (DRIE) in Nanoscience Institute for Medical and Engineering Technology (NIMET) at University of Florida. The equipment has two independent RF power source (at 13.56 MHz), the coil around the etching chamber and the platen coil connected to the sample stage (Figure 5-3). The chamber coil is used to dissociate the species and generate radicals, while platen coil is to control the RF bias potential of the sample for having directional etch. Figure 5-4 shows a typical ion etching process where the plasma generated from SF<sub>6</sub>/O<sub>2</sub> mix gas flow is used to directionally etch the silicon, and C<sub>4</sub>F<sub>8</sub> is then introduced to deposit a passivation layer on the sidewalls to protect etched structures. The steps

are repeated to create deep structures. In our hydrophobic layer deposition, the plasma was generated with only  $C_4F_8$  gas introduced to the system.

Cast thermoplastic samples were taped on a 6-inch wafer, and the wafer was fixed by a set of alumina clamps to the electrode. The whole set was then loaded into the DRIE system. The vacuum was first lower to below 1 mTorr and then maintained at 50 mTorr during the deposition with  $C_4F_8$  flow rate at 90 sccm. The fluorocarbon plasma deposition was carried out for 30 seconds at coil power 600 W without applying platen bias. The thickness of 30-second deposition layer was around 60 nm measured by ellipsometer. Different sets of coil power were tested to obtain the optimum condition. After plasma treatment, the samples were immediately tested with distilled water, and other organic liquid to have preliminary results.

## **Characterization of Plasma Treated Surface**

### **Surface morphology**

The surface morphology before and after plasma treatment was characterized by scanning electron microscope (SEM JSM-6400, JEOL co.). All the samples were coated with a thin layer of Au-Pd (thickness ~30 nm) to improve the conductivity prior to the examination. The voltage for observing the plasma treated samples was at 10-15 KV.

### **Surface chemistry**

Surface chemistry was analyzed by X-Ray photoelectron spectrometry (XPS, Perkin-Elmer XPS/ESCA PHI 5100 ESCA system) with Mg  $K\alpha$  exciting radiation source (1253.6 eV). The typical analysis depth is around 1-10 nm from the bulk surface, since the kinetic energy of the photoelectrons is not large enough to escape from deeper in the sample. The photo-electrons were collected with take-off angle at  $45^\circ$  and quantitated by hemispherical analyzer with pass energy of 22.36 eV. Carbon 1s peak

was used to determine the relative areas of CF, CF<sub>2</sub>, CF<sub>3</sub> and C-CF<sub>x</sub> in fluorocarbon deposited samples. The commercial software that came with the instrument was used to smooth the data, and the peaks were fitted with Gaussian-Lorentzian at ratio 60/40.

### **Contact angle measurement**

Contact angle measurement was mainly carried out by sessile drop test as described in Chapter 4. The Images were photographed by putting 4  $\mu$ l of liquid droplet onto at least 5 different areas of the sample. The syringe was lower towards to the sample to carefully place drops on the surface, and then the needle was removed away from the drop. The captured images were analyzed by *DropSnake* program, a plug-in for the *ImageJ* software. The mean value of the water contact angle and its standard deviation were reported as contact angle ( $\theta_c$ ).

## **Experimental Results**

### **Surface with Water Plasma Treatment**

The water plasma treatment was mainly applied to the highest hydrophobic surfaces, 0.6  $\mu$ m-peeded PP samples. The samples were loaded into the chamber and treated with water plasma for 1 minute (including the prior chamber-clean process in Ar plasma for 5 minutes). After the treatment, drops of different liquids (~10  $\mu$ l) were put onto the surface to quickly exam the wettability. Neither hydrophobicity nor oelophobicity was enhanced after plasma treatment. The water contact angle was greatly lowered to around 97° annihilating its superior water repellency, and other organic liquids were spread on the treated surfaces showing no difference from the untreated samples.

Some of the samples were treated with Ar plasma only; however, as pictures shown in Table 5-1, wetting property of all the samples was similar. The superhydrophobicity was totally vanished even with Ar plasma treatment for only 1 minute. Figure 5-5 shows the morphology of the plasma treated surfaces. The hairy structure was severely damaged after 1 minute Ar plasma treatment (Figure 5-5a and b). The plasma also flattened the original PP substrate slightly lowering the contact angle to around  $88^\circ$  (Figure 5-5c and d). This implies the surfaces had been sustained a certain level of ion bombardment which commonly exists in the plasma.

The plasma contains highly reactive and charged species, and easily to be attracted to impacting an oppositely charged surface. The energy of reactive species is transferred into the material surface during the collision resulting in etching, degradation or chain scissions.<sup>101</sup> Degradation yield and rate depend on plasma and polymer natures. Gaseous radicals, such as  $H^\bullet$ ,  $\bullet OH$ , or  $\bullet O^{-2}$ , generated in the water plasma effectively enhance the degradation process. Even with the Ar plasma, since the chamber is simply sealed with o-ring and equipped with a mechanical pump, the residual oxygen coming from the poor vacuum may also have the same effect. AC power was also lowered to reduce the energy of plasma, but it was difficult to obtain a stable plump. Since the surface structure was majorly damaged from the process, water plasma was not further used for making oleophobic hairy surfaces.

### **Surface with Fluorocarbon Coating**

Fluorocarbon coatings were deposited on the samples by plasma polymerization of  $C_4F_8$  in the DRIE chamber. To avoid a possible damage from the plasma, fluorocarbon coating was deposited onto the PP sheet prior to casting process. As shown in

Figure 5-6, the coated CF layer was like a thermal barrier that completely hindered the formation of surface structures during casting. Although the CF coatings jeopardize the casting process, it could actually be applied as a control mechanism if the surface structure is undesired on some particular area. The plasma deposition of CF therefore has to be carried out onto the cast hairy surfaces. Figure 5-7 shows the hairy structure remained the same after plasma deposition.

The CF layer on the original PP sheets increased the hydrophobicity raising water contact angle from  $94^\circ$  to around  $100^\circ$ . Figure 5-8 shows a methanol-water mixture ( $\gamma \sim 25.2$  mN/m) on hairy PP surfaces coated with CF layers under different plasma power. The contact angles of methanol-water mixture were increased with the increase of plasma power. In contrast to many fluorocarbon precursors, the film deposited from  $C_4F_8$  is more sensitive to the applied RF power.<sup>104</sup> Compared to other smaller fluorocarbons (e.g.  $CF_4$ ,  $C_2F_6$ , etc.), the cyclic structure of  $C_4F_8$  (Figure 5-4b) may take significant RF power to dissociate the molecules.<sup>105</sup> The concentration of  $CF_2$  from XPS spectra (Figure 5-9) also shows that the polymerization of CF molecules was increased with the increase of the RF power.

Table 5-2 lists some of the images of the sessile drops on uncoated and coated cast PP surfaces. Test with water-methanol mixtures showed the contact angles were significantly increased from around  $60^\circ$  to above  $130^\circ$ . The contact angle of olive oil was also raised to  $100^\circ$ . The low surface tension drops should be placed onto the surface with extra careful, since they tend to reach the more stable Wenzel state. However, the coated surfaces still had contact angles around  $30^\circ$  with nonpolar liquids.

## General Discussion

Making surfaces become oil repellent is extremely challenging on an engineering level, since the surface tensions of oily liquids are usually in the range of 20-30 mN/m. The first strategy used was to increase the surface hydrophilicity and thus, the capability of repelling hydrophobic liquids. The hydrophilicity was enhanced by using water plasma to generate more hydroxyl groups on the hairy surface. In order to have something to compare with the PP polymer, two common polymers containing the hydroxyl group, polyvinyl alcohol (PVA) and poly(2-hydroxyethyl methacrylate) (pHEMA), were synthesized. The contact angles of oily liquids on the PP surface were around 30°; however, the liquids on the PVA and pHEMA surfaces were completely spread out, making contact angles unable to be measured (Figure 5-11).

Besides the surface structure was severely damaged, the goal and fundamental concepts seemed to be in conflict. The proposed strategy needed to be reconsidered at this point in terms of the most basic and essential criterion for having liquid repellency: maintaining liquid drops in Cassie-Baxter state. The energy of the CB state is considered meta-stable and has the possibility to transfer into the Wenzel state. The energy state of the meta-stable CB state can be quite complicated, depending on the surface structure.<sup>45-47</sup> The threshold value of the equilibrium contact angle ( $\theta_{trans}$ ), however, can be calculated simply by combining the Wenzel and CB equations, as described in Chapter 2 eq. (2-10):

$$\cos \theta_{trans} = (f_s - 1)/(R_f - f_s) \quad (2-10)$$

where  $R_f$  and  $f_s$  are the surface roughness factor and fraction of liquid/solid contact area. Since  $R_f > 1 > f_s$  makes  $\cos \theta_{trans} < 0$ , the value of this transition contact angle is larger

than 90°. This implies a liquid with a surface contact angle smaller than 90° cannot be in a CB state on that surface. From Young's equation, eq. (2-5), the contact angle ( $\theta_c$ ) is determined by:

$$\cos \theta_c = (\gamma_{SV} - \gamma_{SL}) / \gamma_{LV} \quad (2-5)$$

where  $\gamma_{SV}$ ,  $\gamma_{SL}$ , and  $\gamma_{LV}$  are surface tensions solid/vapor, solid/liquid and liquid/vapor, respectively. When the contact angle is 90°, the  $\gamma_{SL}$  and  $\gamma_{SV}$  should be equal. The term  $\gamma_{SL}$  can be approximated as:<sup>106</sup>

$$\gamma_{SL} = \gamma_{SV} + \gamma_{LV} - 2\sqrt{\gamma_{LV}\gamma_{SV}} \quad (5-1)$$

From eq. (2-5) and eq. (5-1), when the contact angle is at 90°, we can have  $\gamma_{SV} = \gamma_{LV}/4$ . Therefore, for low surface tension liquids, such as octane (21.6 mN/m), to have a contact angle larger than 90°, the surface tension of the substrate material must be at the range of just several mN/m. On the other hand, to induce hydrophilic groups on the surface actually increases the polar contribution to the surface energy and reduces the contact angle of liquid, pulling it further away from oleophobicity. Hence, the strategy should turn to lowering the surface energy of the solid. Among all the solid surfaces, fluorocarbon compounds are renowned for their low surface energy, since the high electronegativity of fluorine atoms makes F-C bonds difficult to be polarized; this, in turn, lowers the hydrogen bonding and dispersion interaction with liquids. The degree of this nonattractive feature increases with the number of fluorine atoms, i.e.,  $CF_3 > CF_2 > CF$ , and also with the chain length of perfluoroalkyl compounds. It is the only material to date that is capable of rendering the surface oleophobic. Note that the substrate was either fluorinated compounds or coated with CF materials having a longer perfluoroalkyl chain ( $CF_3(CF_2)_n$ ,  $n > 7$ ).<sup>105-107</sup>

In addition to lowering the surface energy of substrates, the surface structure also plays a crucial role in superoleophobicity. The geometry of the so-called re-entrant structures, such as mushroom heads, micro-hoodoos, or horizontally aligned cylindrical rods, is proven to have good repellency against low surface tension liquids.<sup>108-110</sup> The re-entrant structure implies that a line drawn vertically up from a point on the projection of the solid surface may meet the actual solid interface more than once. Two examples are shown in Figure 5-12, where (b) represents the re-entrant structure. From the diagrams, when  $\theta_c < \phi$ , the interfacial force is downwards, dragging the liquid towards to the substrate. If  $\theta_c > \phi$ , the interfacial force is upwards, preventing the liquid from moving downwards and creating a possibility for having a composite CB state.

The CF coated hairy surface showed a high contact angle with polar liquids, but the surface energy was not low enough to repel non-polar liquids. The yield of  $\text{CF}_2$  from the plasma polymerization of  $\text{C}_4\text{F}_8$  is lower than using compounds with a longer perfluoroalkyl chain.<sup>106</sup> In addition, the hairy structure cannot be categorized as a re-entrant structure, as most of the hairs are inclined at a certain angle with tips of smaller diameters making the profile of liquid interface as it shows in Figure 5-12.

### Summary

In this chapter, the efforts aimed to extend the remarkable water repellency into oil repellency (superoleophobicity). It is a great challenge in engineering because the surface tensions of oily liquids are only a half to one-third that of water. Two opposite strategies were adopted to test the possibility of rendering hairy surface oleophobic: (1) to increase the surface hydrophilicity and (2) to increase the surface hydrophobicity. Water plasma was first used to increase the hydrophilicity by inducing a hydroxyl group

onto the surface. However, the surface structure was destroyed, resulting in the complete loss of superhydrophobicity and oleophobicity. Moreover, the idea of increasing the surface hydrophilicity intrinsically increases the surface energy, making the surfaces more difficult to repel low surface tension liquids. Therefore the water plasma was not used for the purpose of increasing oleophobicity.

To increase the surface hydrophobicity, commercial equipment, DRIE, was used to plasma-polymerize a CF layer onto the hairy surfaces. The contact angle of low surface tension polar liquids ( $\gamma < 35.2$  mN/m) was raised from  $60^\circ$  to around  $140^\circ$ . The surface energy of the coated samples was still not low enough to create a high contact angle with non-polar liquids. To achieve superoleophobicity, the first criterion is to lower the surface energy of the substrate to about one quarter of the oily liquid. Fluorocarbon compounds are the only substances that are able to lower the surface energy enough to the oleophobic range. The so-called re-entrant structure also enhances the surface to maintain the liquid in a composite CB state.

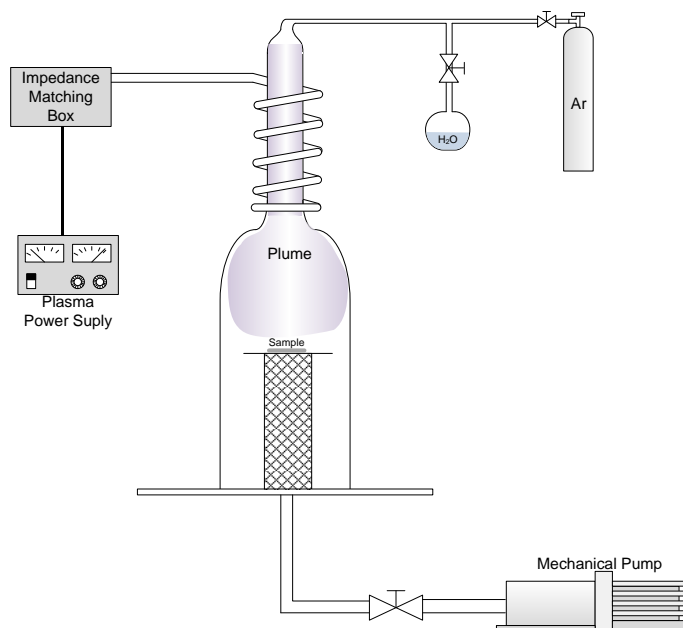


Figure 5-1. Schematic diagram of the plasma system used in this work. The plasma was induced by radio frequency coil. The vacuum was generated simply by a mechanical pump.



Figure 5-2. The plasma chamber is a modified bell jar with a copper cable coiled in the upper part. The sample was placed under the plume of water plasma during the treatment.

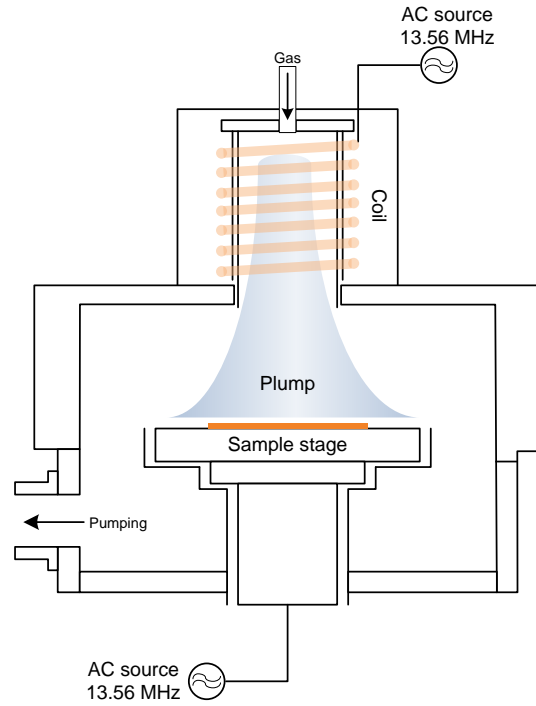


Figure 5-3. Schematic diagram of the STS deep reactive ion etch system.

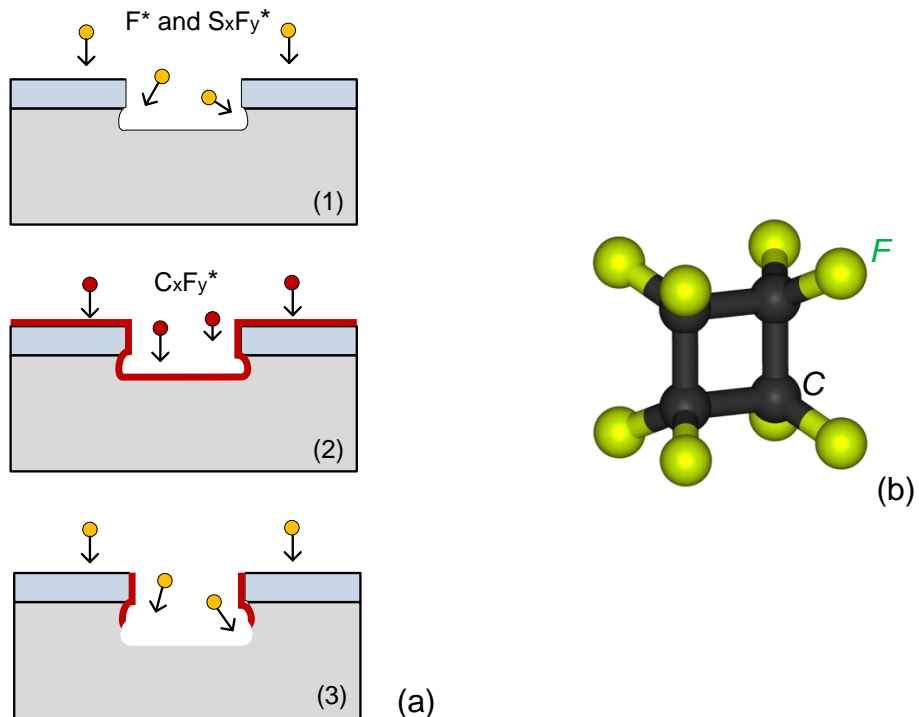
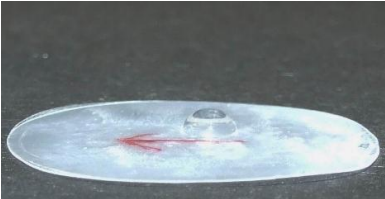
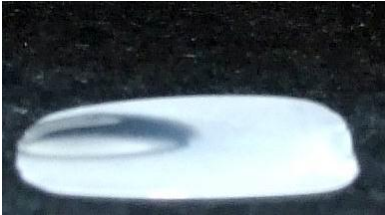


Figure 5-4. (a) Schematic diagram of the typical process of deep reactive ion etching (1) directional etching, (2) deposition of passivation layer, (3) next etch step. (b) Octafluorocyclobutane ( $C_4F_8$ ) molecule for passivation layer.

Table 5-1. Liquid drops on plasma treated 0.6 $\mu$ m-peeled PP samples.

Treatment	Liquid		
	Water ( $\gamma$ ~72.8 mN/m)	Oliver oil ( $\gamma$ ~34.6 mN/m)	Hexane ( $\gamma$ ~18.4 mN/m)
Ar 5 min + H <sub>2</sub> O 1 min			
Ar 5 min			
Ar 1 min			

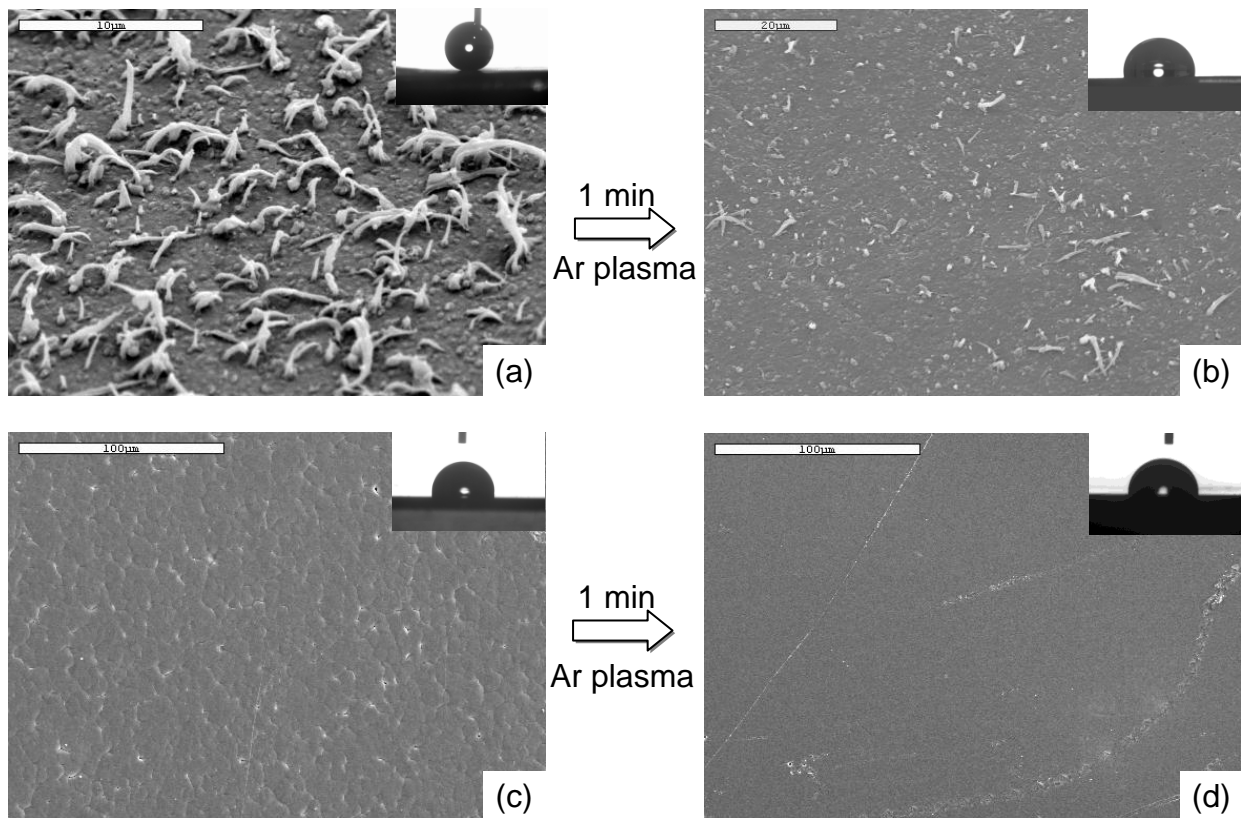


Figure 5-5. (a) and (b) are the morphology of hairy surface before and after Ar plasma. The contact angle was lowered from  $170^\circ$  to  $95^\circ$ . (c) and (d) are the morphology of original PP sheet before and after Ar plasma. The contact angle was slightly lowered from  $94^\circ$  to  $88^\circ$ .

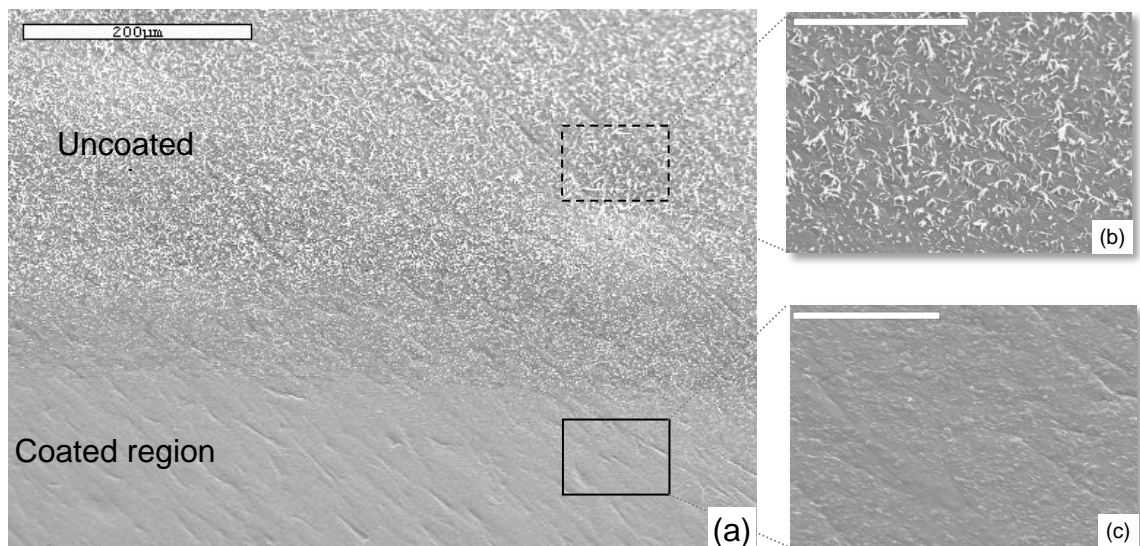


Figure 5-6. The surface morphology of CF coated PP samples after casting process. (a) The CF layer hinders the formation of cast structure. (b) and (c) are closer views of the different regions, and the bars are  $50\mu\text{m}$  and  $20\mu\text{m}$ , respectively.

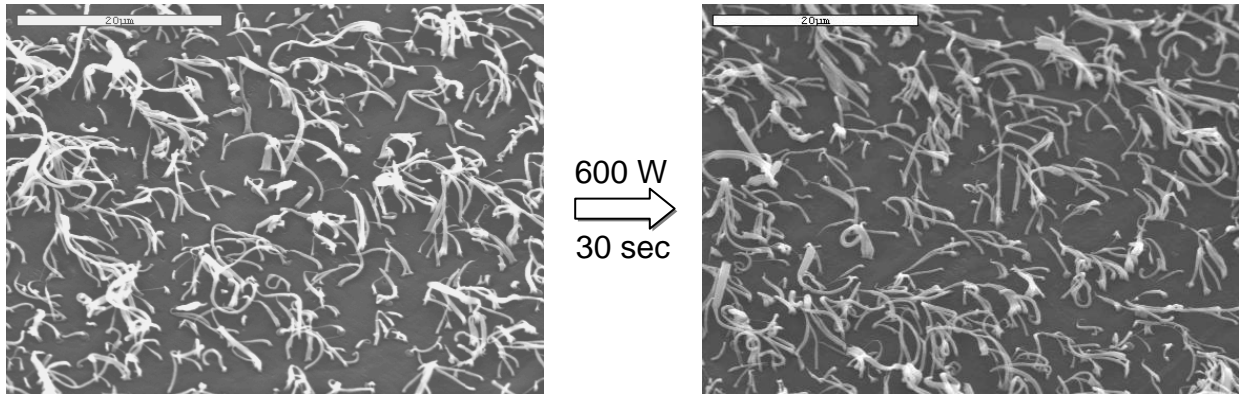


Figure 5-7. The hairy structure before and after plasma deposition of CF layer in DRIE chamber.

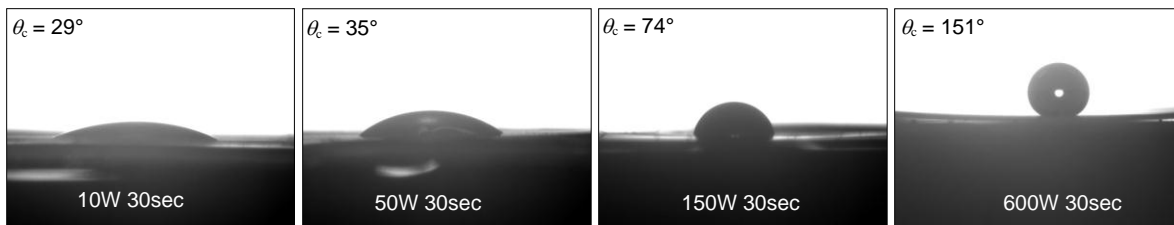


Figure 5-8. Contact angles of methanol-water mixture ( $\gamma \sim 25.2$  mN/m) on hairy surfaces coated with different plasma power.

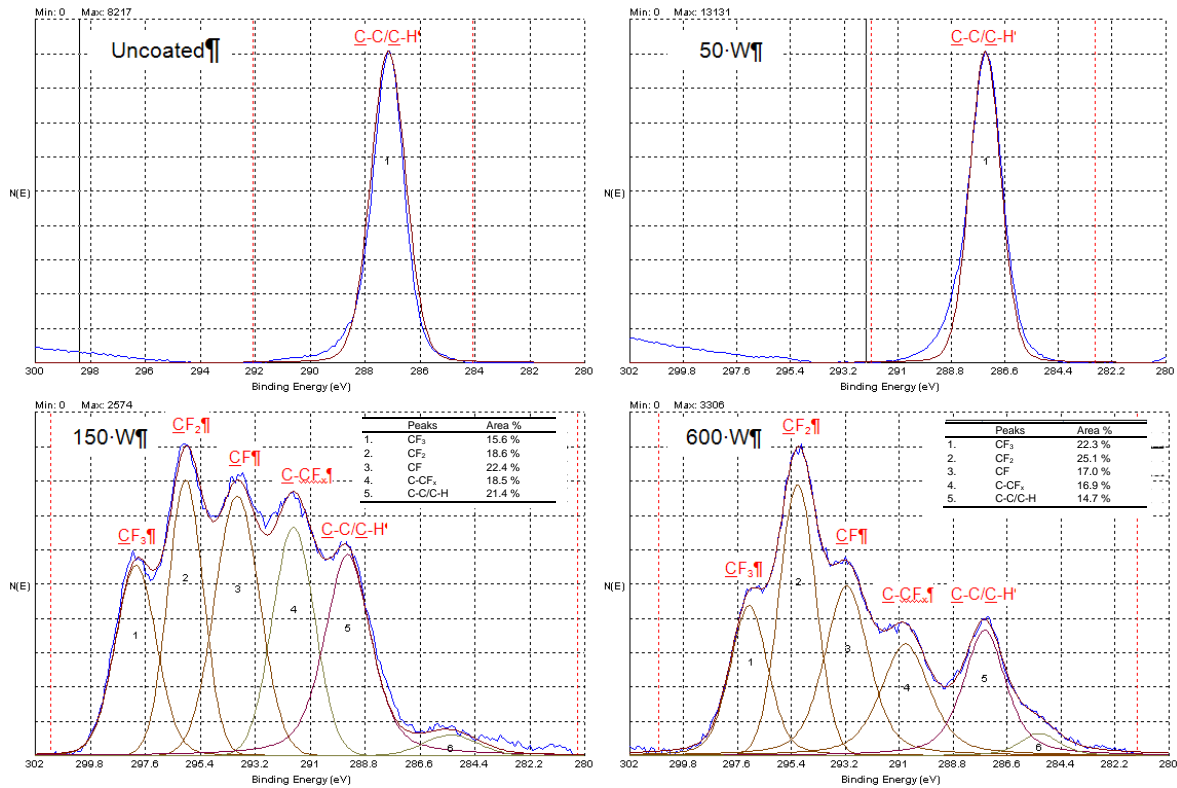


Figure 5-9. XPS results of CF coated surfaces under different plasma power.

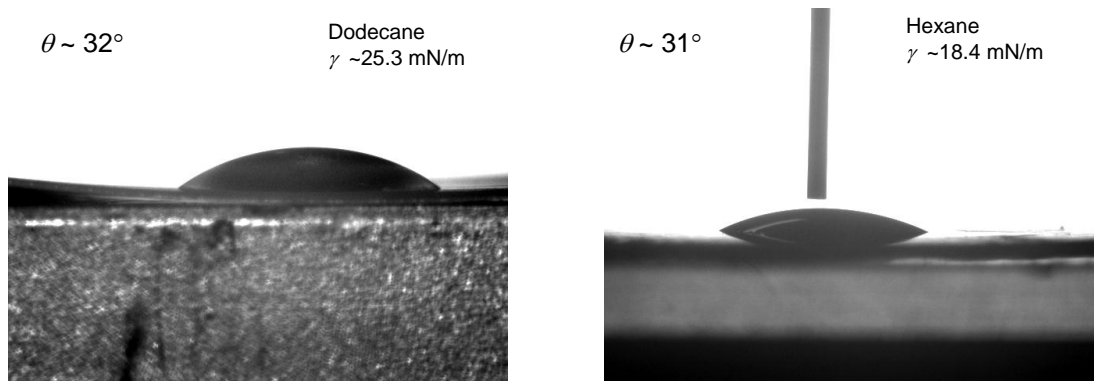
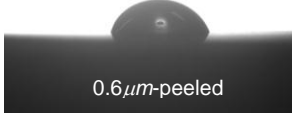
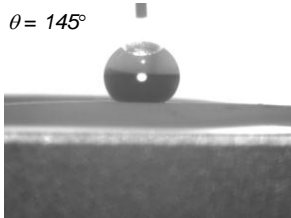
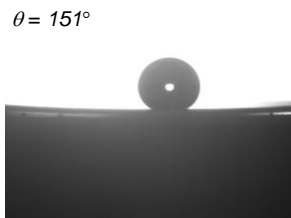
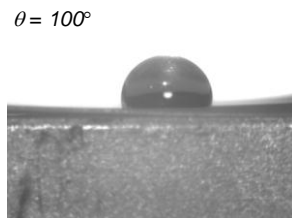
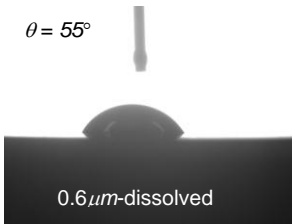
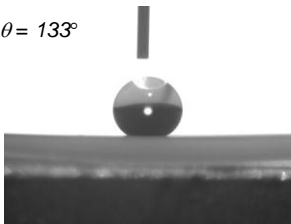
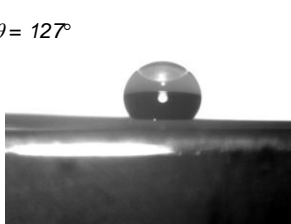
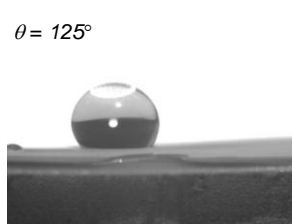
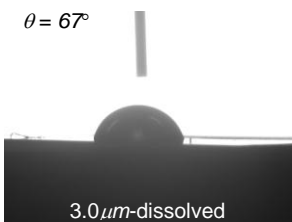
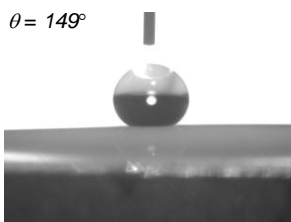
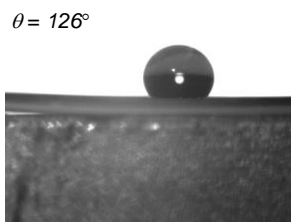
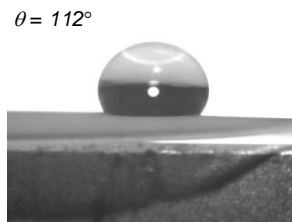


Figure 5-10. Low contact angle of nonpolar liquid (dodecane) on CF coated  $0.6\mu\text{m}$ -peeled hairy surfaces.

Table 5-2. Contact angles of low surface tension liquids on cast PP surfaces before and after CF coatings.

Uncoated	Coated		
	H <sub>2</sub> O-MeOH ( $\gamma \sim 35.2$ mN/m)	H <sub>2</sub> O-MeOH $\square$ ( $\gamma \sim 35.2$ mN/m)	H <sub>2</sub> O-MeOH $\square$ ( $\gamma \sim 25.2$ mN/m)
$\theta = 69^\circ$   0.6 $\mu$ m-peeled	$\theta = 145^\circ$ 	$\theta = 151^\circ$ 	$\theta = 100^\circ$ 
$\theta = 55^\circ$  0.6 $\mu$ m-dissolved	$\theta = 133^\circ$ 	$\theta = 127^\circ$ 	$\theta = 125^\circ$ 
$\theta = 67^\circ$  3.0 $\mu$ m-dissolved	$\theta = 149^\circ$ 	$\theta = 126^\circ$ 	$\theta = 112^\circ$ 

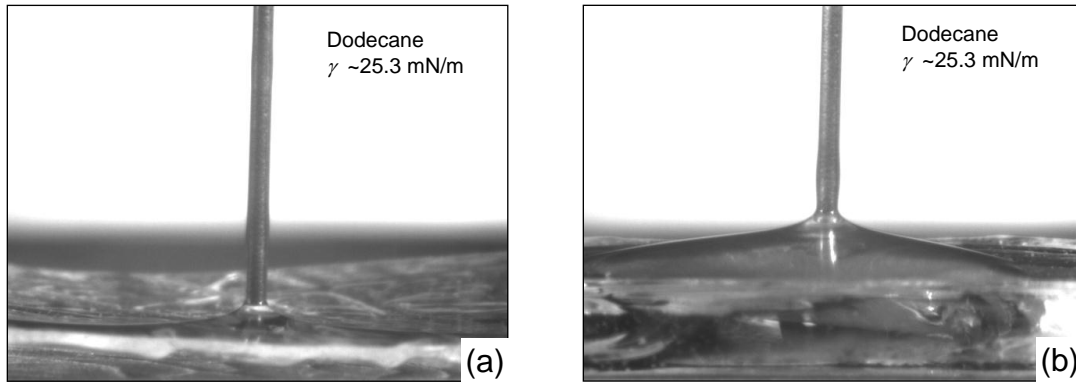


Figure 5-11. Low surface tension liquid (dodecane) completely spread out on the hydrophilic polymers, (a) PVA and (b) pHEMA.



Figure 5-12. Schematic diagrams of interfacial force when a liquid with contact angle  $\theta_c$  on the same substrate material but having different geometry. (a) non-reentrant structure, and (b) reentrant structure.

## CHAPTER 6 CONCLUSIONS AND SUGGESTIONS FOR FUTURE WORK

### **Conclusions**

The main goal of this study, as delineated in the introduction, is to develop a liquid repellent surface by mimicking the hairy exterior of arthropods. The synthetic superhydrophobic surfaces based on this type of structure are still very limited, though the role of the piliferous integument has long been recognized as rendering many arthropods water repellent and providing critical living functions. Therefore the main efforts of the study were devoted to creating the artificial hairy surfaces and to studying their wetting behaviors.

The majority of the surfaces in the study were prepared by casting the thermoplastics with commercial porous membranes. The fabrication method was relatively simple and cost-effective, but the membrane limited the control of the experimental parameters, such as the areal density and distribution of structures. The particular hairy surface was successfully created on cast PP substrates after peeling off the PC membrane, where the surface was covered with *I*-shaped pillars analogous to the natural hairs of the arthropods. They tapered to a point from a base with the pore-size diameter while the length varied from less than a micron to about 10 microns. The longer hairs were tilted around 30° to 45° with their tips curled towards or parallel to the substrate.

The process to create hair-like surface structure has been demonstrated on other thermoplastics, including LDPE and PVDF. The casting temperature needs to be higher than the melting point of the substrate, while the peeling has to be performed at a temperature below the glass-transition range. The cast structure is not robust and easily

damaged with an external force. However, the durability is a general concern on all superhydrophobic surfaces. The current process has the possibility to be scaled up for the production of large-area superhydrophobic surfaces.

In general, the water contact angles on the cast structures were all significantly increased. The high contact angle denotes that a fair amount of air pockets were trapped underneath the droplet; the angle value can be rationalized by the CB equation. Remarkable water repellency was found on the PP surfaces possessing artificial hairy structures. Video assessment has confirmed that the PP hairy surfaces is perfectly hydrophobic ( $\theta_{adv}=\theta_{rec}=180^\circ$ ) and is by far one of the best superhydrophobic surfaces within the non-chemically treated surfaces. The hydrophobic methyl group of PP and a possible mechanical response to the liquid interface, where the deflected hairs resist further wetting, are considered the major factors in lowering the contact angle hysteresis. However, the hydrophobicity of hairy leaves is quite different from the synthetic surfaces. The  $180^\circ$  water contact angle of droplets on Lady's Mantle comes simply from the strong pinning of contact lines rather than the elastic response of the hairs.

To extend the repellency to oily liquids (oleophobicity) is a great challenge on an engineering level as the surface tensions of oily liquids are only half to one-third of water. To achieve superoleophobicity, the first criterion is to lower the surface energy of the substrate to about one quarter of the oily liquid. Fluoro-carbon (CF) compounds are the only substances that are able to lower the surface energy enough to the oleophobic range. The CF layer was coated onto the hairy PP surface with commercial equipment, DRIE, to enhance the liquid repellency. The contact angle of the water-methanol liquid

( $\gamma < 35.2$  mN/m) was raised from  $60^\circ$  to around  $140^\circ$ . However, the surface energy of the coated samples was still not low enough to have a high contact angle with non-polar liquids.

## **Suggestions for Future Work**

### **The Role of Elasticity on Water Repellency**

Although the superior water repellency of the synthetic hairy surface is believed to be mainly based on the physical interaction of the interface, no direct evidence was available in this study. Direct observation on the interface between the artificial hairs and the droplet will be the best investigation to solve this mystery. However, it will be a challenge for optical microscopes to observe an event this size. Environmental scanning electron microscopes (E-SEM) may provide a better solution. The imaging chamber pressure of the E-SEM can be as high as  $10^{-2}$  atm, and it can be filled with water vapor, keeping the sample hydrated over an extended period. It has already been operated in this fashion to examine the interaction of droplets and the lotus leaf. The technique will be able to discover the direct interaction of droplets and the hair arrays.

### **Quantitative Study of Self-Cleaning Effect**

As demonstrated in Chapter 4, the synthetic hairy surface features a strong, self-cleaning ability. Although this effect has been a subject of considerable scientific interest for over a decade, compared to the efforts in making surfaces superhydrophobic, insightful studies on understanding this effect are still very rare. The synthetic hairy surfaces provide appropriate media for the study, as the adequate surface area of samples with different morphology and hydrophobicity are easily prepared. The research should rule out the factors and relationships, such as particle size, particle hydrophobicity, and contact angle hysteresis vs. cleaning efficiency. The

challenge will be mainly on how to quantify the cleaning ability, since the mass of washed-off dirt particles will be small. Observation under a microscope, either through fluorescent particles or direct count, is a possible solution.

## LIST OF REFERENCES

1. Young, T. An Essay on the Cohesion of Fluids. *Phil. Trans. R. Soc. Lond.* **1804**, 95, 65–87.
2. Feng, X. J.; Jiang, L. Design and creation of superwetting/antiwetting surfaces. *Adv Mater.* **2006**, 18, 3063–3078.
3. Ma, M. L.; Hill, R. M. Superhydrophobic surfaces. *Curr. Opin. Colloid In.* **2006**, 11, 193–202.
4. Zhang, X.; Shi, F.; Niu, J.; Jiang, Y. G. Wang, Z. Q. Superhydrophobic surfaces: from structural control to functional application. *J. Mater. Chem.* **2008**, 18, 621–633.
5. Nosonovsky, M.; Bhushan, B. Superhydrophobic surfaces and emerging applications: Non-adhesion, energy, green engineering. *Curr. Opin. Colloid In.* **2009**, 14, 270–280.
6. Roach, P.; Shirtcliffe, N. J.; Newton, M. I. Progress in superhydrophobic surface development. *Soft Matter.* **2008**, 4, 224–240.
7. Genzer, J.; Efimenko, K. Recent developments in superhydrophobic surfaces and their relevance to marine fouling: a review. *Biofouling.* **2006**, 22, 339–360.
8. Zhang, H.; Lamb, R. Lewis, J. Engineering nanoscale roughness on hydrophobic surface – preliminary assessment of fouling behaviour. *Sci. Technol. Adv. Mat.* **2005**, 6, 236–239.
9. Daniello, R. J.; Waterhouse, N. E.; Rothstein, J. P. Drag reduction in turbulent flows over superhydrophobic surfaces. *Phys Fluids.* **2009**, 21, 085103.
10. Barthlott, W.; Neinhuis, C. Purity of the sacred lotus, or escape from contamination in biological surfaces. *Planta.* **1997**, 202, 1–8.
11. Neinhuis, C.; Barthlott, W. Characterization and distribution of water-repellent, self-cleaning plant surfaces. *Ann. Bot-London.* **1997**, 79, 667–677.
12. Liu, Y. Y.; Chen, X. Q.; Xin, J. H. Can superhydrophobic surfaces repel hot water? *J. Mater. Chem.* **2009**, 19, 5602–5611.
13. Otten, A.; Herminghaus, S. How plants keep dry: A physicist's point of view. *Langmuir* **2004**, 20, 2405–2408.
14. Wenzel, R. N. Resistance of solid surfaces to wetting by water. *Ind Eng Chem.* **1936**, 28, 988–994.

15. Holdgate, M. W. The wetting of insect cuticles by water. *J. Exp. Biol.* **1955**, *32*, 591–617.
16. Hu, D. L.; Chan, B.; Bush, J. W. M. The hydrodynamics of water strider locomotion. *Nature* **2003**, *424*, 663–666.
17. Thorpe, W. H.; Crisp, D. J. Studies on plastron respiration .1. The biology of aphelocheirus [Hemiptera, Aphelocheiridae (Naucoridae)] and the mechanism of plastron retention. *J. Exp. Biol.* **1947**, *24*, 227–269.
18. Hinton, H. E. Plastron respiration in bugs and beetles. *J. Insect Physiol.* **1976**, *22*, 1529–1550.
19. Gao, X. F.; Jiang, L. Water-repellent legs of water striders. *Nature* **2004**, *432*, 36–36.
20. Comstock, J. H. Note on the respiration of aquatic bugs. *Am. Nat.* **1887**, *21* 577–578.
21. del Campo, A.; Arzt, E. Fabrication approaches for generating complex micro- and nanopatterns on polymeric surfaces. *Chem. Rev.* **2008**, *108*, 911–945.
22. Mock, U.; Forster, R.; Menz, W.; Ruhe, J. Towards ultrahydrophobic surfaces: a biomimetic approach. *J. Phys-Condens. Mat.* **2005**, *17*, S639–S648.
23. Goodwyn, P. P.; De Souza, E.; Fujisaki, K.; Gorb, S. Moulding technique demonstrates the contribution of surface geometry to the super-hydrophobic properties of the surface of a water strider. *Acta. Biomater.* **2008**, *4*, 766–770.
24. Dupre, A. *Theorie Mechanique de la Chaleur*; Gauthier-Villars: Paris, **1869**, 36W.
25. Cassie, A. B. D.; Baxter, S. Wettability of porous surfaces. *T. Faraday. Soc.* **1944**, *40*, 0546–0550.
26. Bico, J.; Marzolin, C.; Quere, D. Pearl drops. *Europhys. Lett.* **1999**, *47*, 220–226.
27. Lafuma, A.; Quere, D. Superhydrophobic states. *Nat. Mater.* **2003**, *2*, 457–460.
28. Quere, D.; Non-sticking drops. *Rep. Prog. Phys.* **2005**, *68*, 2495–2532.
29. Dupuis, A.; Yeomans, J. M. Modeling droplets on superhydrophobic surfaces: Equilibrium states and transitions. *Langmuir* **2005**, *21*, 2624–2629.
30. Patankar, N. A. Transition between superhydrophobic states on rough surfaces. *Langmuir* **2004**, *20*, 7097–7102.

31. Patankar, N. A. Mimicking the lotus effect: Influence of double roughness structures and slender pillars. *Langmuir* **2004**, *20*, 8209–8213.
32. Marmur, A. The lotus effect: Superhydrophobicity and metastability. *Langmuir* **2004**, *20*, 3517–3519.
33. Bico, J.; Thiele, U.; Quere, D. Wetting of textured surfaces. *Colloid Surface A*. **2002**, *206*, 41–46.
34. Miwa, M.; Nakajima, A.; Fujishima, A.; Hashimoto, K.; Watanabe, T. Effects of the surface roughness on sliding angles of water droplets on superhydrophobic surfaces. *Langmuir* **2000**, *16*, 5754–5760.
35. McHale, G.; Shirtcliffe, N. J.; Newton, M. I. Contact-angle hysteresis on superhydrophobic surfaces. *Langmuir* **2004**, *20*, 10146–10149.
36. Furmidge, C. G. Studies at Phase Interfaces 1. Sliding of Liquid Drops on Solid Surfaces and a Theory for Spray Retention. *J. Coll. Sci. Imp. U. Tok.* **1962**, *17*, 309–324.
37. Dettre, R. H.; Johnson, R. E. Jr. *Contact Angle, Wettability and Adhesion; Adv. Chem. Ser.*; Amer. Chem. Soc., Washington, DC: **1964**; *43*, p 136–144.
38. Extrand, C. W. Model for contact angles and hysteresis on rough and ultraphobic surfaces. *Langmuir* **2002**, *18*, 7991–7999.
39. Yoshimitsu, Z.; Nakajima, A.; Watanabe, T.; Hashimoto, K. Effects of surface structure on the hydrophobicity and sliding behavior of water droplets. *Langmuir* **2002**, *18*, 5818–5822.
40. Wolfram, E.; Faust, R. *Wetting, Spreading, and Adhesion*, Academic, London: **1978**, p 213.
41. Holloway, P. J. Surface factors affecting the wetting of leaves. *Pestic. Sci.* **1970**, *1*, 156–163.
42. Koch, K.; Dommissie, A.; Barthlott, W. Chemistry and crystal growth of plant wax tubules of Lotus (*Nelumbo nucifera*) and Nasturtium (*Tropaeolum majus*) leaves on technical substrates. *Crystl. Growth Des.* **2006**, *6*, 2571–2578.
43. Gao, L.; McCarthy, T.J. The lotus effect explained: Two reasons why two length scales of topography are Important. *Langmuir* **2006**, *22*, 2966–2967.
44. Nosonovsky M, Multiscale roughness and stability of superhydrophobic biomimetic interfaces. *Langmuir* **2007**, *23*, 3157–3161.

45. Nosonovsky, M. Model for solid-liquid and solid-solid friction for rough surfaces with adhesion hysteresis. *J. Chem. Phys.*, **2007**, *126*, 224701.
46. Nosonovsky, M.; Bhushan, B. Hierarchical roughness makes superhydrophobic surfaces stable. *Microelectronic Eng.* **2007**, *84*, 382–386.
47. Nosonovsky, M.; Bhushan, B. Hierarchical roughness optimization for biomimetic superhydrophobic surfaces. *Ultramicroscopy* **2007**, *107*, 969–979.
48. Nosonovsky, M.; Bhushan, B. Multiscale friction mechanisms and hierarchical surfaces in nano- and bio-tribology. *Mater. Sci. Eng. R.* **2007**, *58*, 162–193.
49. Nosonovsky, M.; Bhushan, B. Roughness-induced superhydrophobicity: a way to design non-adhesive surfaces. *J. Phys.: Condens. Matter* **2008**, *20*, 225009.
50. Furstner, R.; Barthlott, W.; Neinhuis, C.; Walzel, P. Wetting and self-cleaning properties of artificial superhydrophobic surfaces. *Langmuir* **2005**, *21*, 956–961.
51. Thorpe, W. H.; Crisp, D. J. Studies on plastron respiration III. The orientation responses of *Apelocheirus* [Hemiptera, Aphelocheiridae (Naucoridae)] in relation to plastron respiration; together with an account of specialized pressure receptors in aquatic insects. *J. Exp. Biol.* **1947**, *24*, 310–328.
52. Wigglesworth, V. B. The physiology of the cuticle and of ecdysis in *Rhodnius prolixus* (Triatomidae, Hemiptera); with special reference to the function of the oenocytes and of the dermal glands. *Q. J. Microsc. Sci.* **1933**, *76*, 269–318.
53. Wigglesworth, V. B. Transpiration through the cuticle of insects. *J. Exp. Biol.* **1945**, *21*, 97–114.
54. Pal, R. The wetting of insect cuticle. *Bull. Ent. Res.* **1951**, *51*, 121–139.
55. Stratton, G. E.; Suter, R. B.; Miller, P. R. Taxonomic variation among spiders in the ability to repel water: surface adhesion and hair density. *J. Arachnol.* **2004**, *32*, 11–21.
56. Bush, J. W. M.; Hu, D. L. Prakash, M. The integument of water-walking arthropods: Form and function. *Adv Insect Physiol.* **2007**, *34*, 117–192.
57. Lamoral, B. H. On the ecology and habitat adaptations of two intertidal spiders, *Desis formidabilis* and *Amaurobioides africanus* Hewitt at 'The Island' (Kommetjie, Cape Peninsula), with notes on the occurrence of two other spiders. *Ann. Natal. Mus.* **1968**, *20*, 151–193.
58. Lange, N.A.; Dean, J. A. *Lange's Handbook of chemistry 11th ed.* McGraw-Hill, NY: **1973**, p 1661-1665.

59. ASTM D638, Standard test method for tensile properties of plastics, ASTM International: USA, **2008**
60. Zheng, H. P.; Lee, I. S.; Rubner, M. F.; Hammond, P. T. Two component particle arrays on patterned polyelectrolyte multilayer templates. *Adv. Mater.* **2002**, *14*, 569.
61. Liu, Z. F.; Shen, Z. Y.; Zhu, T.; Hou, S. F.; Ying, L. Z.; Shi, Z. J.; Gu, Z. N. Organizing single-walled carbon nanotubes on gold using a wet chemical self-assembling technique. *Langmuir* **2000**, *16*, 3569–3573.
62. Wu, B.; Zhang, J.; Wei, J.; Cai, S. M.; Liu, Z. F. Chemical alignment of oxidatively shortened single-walled carbon nanotubes on silver surface. *J. Phys. Chem. B* **2001**, *105*, 5075–5078.
63. Kim, B.; Sigmund, W. M. Self-alignment of shortened multiwall carbon nanotubes on polyelectrolyte layers. *Langmuir*, **2003**, *19*, 4848–4851.
64. Lau, K. K. S.; Bico, J.; Teo, K. B. K.; Chhowalla, M.; Amaratunga, G. A. J.; Milne, W. I.; McKinley, G. H. Gleason, K. K. Superhydrophobic carbon nanotube forests. *Nano Lett.* **2003**, *3*, 1701-1705.
65. Journet, C.; Moulinet, S.; Ybert, C.; Purcell, S. T.; Bocquet, L. Contact angle measurements on superhydrophobic carbon nanotube forests: Effect of fluid pressure. *Europhys. Lett.* **2005**, *71*, 104-109.
66. Joseph, P.; Cottin-Bizonne, C.; Benoit, J.-M.; Ybert, C.; Journet, C.; Tabeling, P.; Bocquet, L. Slippage of water past superhydrophobic carbon nanotube forests in microchannels, *Phys. Rev. Lett.* **2006**, *97*, 156104.
67. Demczyk, B. G.; Wang, Y. M.; Cumings, J.; Hetman, M.; Han, W.; Zettl A.; Ritchie, R. O. Direct mechanical measurement of the tensile strength and elastic modulus of multiwalled carbon nanotubes. *Mat. Sci. Eng. A* **2002**, *334*, 173–178.
68. Quake, S. R.; Scherer, A. From micro- to nanofabrication with soft materials. *Science* **2000**, *290*, 1536-1540
69. Roca-Cusachs, P.; Rico, F.; Martinez, E.; Toset, J.; Farre, R. Navajas, D. Stability of microfabricated high aspect ratio structures in poly(dimethylsiloxane). *Langmuir* **2005**, *21*, 5542-5548.
70. Sharp, K. G.; Blackman, G. S.; Glassmaker, N. J.; Jagota, A. Hui, C. Y. Effect of stamp deformation on the quality of microcontact printing: Theory and experiment. *Langmuir.* **2004**, *20*, 6430-6438

71. Moore, E. P. *Polypropylene Handbook. Polymerization, Characterization, Properties, Processing, Applications*. Hanser Publishers: NY, **1996**
72. Kang, T. S.; Smith, A. P.; Taylor, B. E. Durstock, M. F. Fabrication of Highly-Ordered TiO<sub>2</sub> Nanotube Arrays and Their Use in Dye-Sensitized Solar Cells. *Nano Lett.* **2009**, 9, 601-606.
73. Steinhart, M.; Wehrspohn, R. B.; Gosele, U. Wendorff, J. H. Nanotubes by template wetting: A modular assembly system. *Ange. Chem. Internat. Ed.* **2004**, 43, 1334-1344
74. Zhang, Q. M.; Bharti, V.; Kavarnos, G.; Schwartz, M. (Ed.), *Poly (Vinylidene Fluoride) (PVDF) and its Copolymers. Encyclopedia of Smart Materials*. John Wiley & Sons: NY **2002**, 1-2, p 807-825.
75. Geim, A. K.; Dubonos, S. V.; Grigorieva, I. V.; Novoselov, K. S.; Zhukov, A. A.; Shapoval, S. Y. Microfabricated adhesive mimicking gecko foot-hair. *Nat Mater.* **2003**, 2, 461-463.
76. Baeurle, S. A.; Hotta, A.; Gusev, A. A. On the glassy state of multiphase and pure polymer materials. *Polymer* **2006**, 47, 6243-6253.
77. Biswas, S. K.; Vijayan, K.; Friction and Wear of PTFE - a Review. *Wear* **1992**, 158, 193-211.
78. Kwak, G.; Seol, M.; Tak, Y.; Yong, K. Superhydrophobic ZnO nanowire surface: chemical modification and effects of UV irradiation. *J. Phys. Chem. C.* **2009**, 113, 12085-12089.
79. Li, L. H.; Chen, Y. Superhydrophobic Properties of Nonaligned Boron Nitride Nanotube Films. *Langmuir* **2010**, 26, 5135-5140.
80. Yeh, K. Y.; Cho, K. H. Chen, L. J. Preparation of superhydrophobic surfaces of hierarchical structure of hybrid from nanoparticles and regular pillar-like pattern. *Langmuir* **2009**, 25, 14187-14194.
81. Ma, M.; Hill, R. M. Rutledge, G. C. A Review of Recent Results on Superhydrophobic materials based on micro- and nanofibers. *J. Adhes. Sci. Technol.* **2008**, 22, 1799-1817.
82. Majidi, C.; Groff, R. E.; Maeno, Y.; Schubert, B.; Baek, S.; Bush, B.; Maboudian, R.; Gravish, N.; Wilkinson, M.; Autumn, K. Fearing, R. S. High friction from a stiff polymer using microfiber arrays. *Phys. Rev. Lett.* **2006**, 97, 076103.
83. Lee, J.; Fearing, R. S.; Contact self-cleaning of synthetic gecko adhesive from polymer microfibers. *Langmuir.* **2008**, 24, 10587-10591.

84. Autumn, K.; Majidi, C.; Groff, R. E.; Dittmore, A. Fearing, R. Effective elastic modulus of isolated gecko setal arrays. *J. Exp. Biol.* **2006**, *209*, 3558-3568.
85. Guo, C. W.; Feng, L.; Zhai, J.; Wang, G. J.; Song, Y. L.; Jiang, L.; Zhu, D. B. Large-area fabrication of a nanostructure-induced hydrophobic surface from a hydrophilic polymer. *Chem. Phys. Chem.* **2004**, *5*, 750-753.
86. Wu, Y. Y.; Bekke, M.; Inoue, Y.; Sugimura, H.; Kitaguchi, H.; Liu, C. S.; Takai, O. Mechanical durability of ultra-water-repellent thin film by microwave plasma-enhanced CVD *Thin Solid Films* **2004**, *457*, 122-127.
87. Cui, Z.; Wang, Q. J.; Xiao, Y.; Su, C. H.; Chen, Q. M. The stability of superhydrophobic surfaces tested by high speed current scouring *Appl. Surf. Sci.* **2008**, *254*, 2911-2916.
88. Marmur, A. From hydrophilic to superhydrophobic: Theoretical conditions for making high-contact-angle surfaces from low-contact-angle materials. *Langmuir* **2008**, *24*, 7573-7579
89. Stalder, A.F.; Kulik, G.; Sage, D.; Barbieri, L.; Hoffmann, P. *Colloids Surf., A: Physicochem. Eng. Aspects* **2006**, *286*, 92-103
90. Kass M.; A. Witkin, D. Terzopoulos, Snakes: Active contour models. *Int. J. Comput. Vis.* **1988**, *2*, 321–331.
91. The program *ImageJ* can be downloaded from: <http://rsbweb.nih.gov/ij/>
92. The program *DropSnake* can be downloaded from: <http://bigwww.epfl.ch/demo/dropanalysis/>
93. Bernardino, N. R.; Blicke, V.; Dietrich, S. Wetting of surfaces covered by elastic hairs *Langmuir*, **2010**, *26*, 7233–7241.
94. Quere, D. Wetting and roughness. *Annu Rev Mater Res.* **2008**, *38*, 71-99.
95. Jung, Y. C.; Bhushan B. Dynamic effects induced transition of droplets on biomimetic superhydrophobic surfaces *Langmuir*, **2009**, *25*, 9208–9218.
96. Erbil, H. Y.; Demirel, A. L.; Avci, Y.; Mert, O. Transformation of a simple plastic into a superhydrophobic surface. *Science* **2003**, *299*, 1377-1380.
97. Gao, L. C.; McCarthy, T. J. A perfectly hydrophobic surface. *J Am. Chem. Soc.* **2006**, *128*, 9052-9053.
98. Gao, L. C.; McCarthy, T. J. A commercially available perfectly hydrophobic material. *Langmuir* **2007**, *23*, 9125-9127.

99. The videos can be accessed through ACS *Langmuir* website on:  
<http://pubs.acs.org/doi/abs/10.1021/la903813g>
100. Jin, M. H.; Feng, X. J.; Feng, L.; Sun, T. L.; Zhai, J.; Li, T. J. Jiang, L. Superhydrophobic aligned polystyrene nanotube films with high adhesive force. *Adv Mater.* **2005**, *17*, 1977
101. Lejeune, M.; Lacroix, L. M.; Bretagnol, F.; Valsesia, A.; Colpo, P. Rossi, F. Plasma-based processes for surface wettability modification. *Langmuir.* **2006**, *22*, 3057-3061.
102. Andersson, H.; van der Wijngaart, W.; Griss, P.; Niklaus, F. Stemme, G. Hydrophobic valves of plasma deposited octafluorocyclobutane in DRIE channels. *Sensor Actuat B-Chem.* **2001**, *75*, 136-141.
103. Zhuang, Y. X. Menon, A. Wettability and thermal stability of fluorocarbon films deposited by deep reactive ion etching. *Journal of Vacuum Science & Technology A.* **2005**, *23*, 434-439
104. Labelle, C. B.; R. Opila,;. Kornblitc A. Plasma deposition of fluorocarbon thin films from c-C4F8 using pulsed and continuous rf excitation *J. Vac. Sci. Technol. A* **2005**, *23*, 190-196.
105. Gnanappa, A. K.; Slattery, O.; Peters, F.; O'Murchu, C.; O'Mathuna, C.; Fahey, R.; Taylor, J. A. Krupenkin, T. N. Factors influencing adhesion of fluorocarbon (FC) thin film on silicon substrate. *Thin Solid Films.* **2008**, *516*, 5673-5680.
106. Coulson, S. R.; Woodward, I. S.; Badyal, J. P. S.; Brewer, S. A. Willis, C. Ultralow surface energy plasma polymer films. *Chem. Mater.* **2000**, *12*, 2031-2038.
107. Coulson, S. R.; Woodward, I. S.; Badyal, J. P. S.; Brewer, S. A. Willis, C. Plasmachemical functionalization of solid surfaces with low surface energy perfluorocarbon chains. *Langmuir* **2000**, *16*, 6287-6293.
108. Marmur, A. From hydrophilic to superhydrophobic: Theoretical conditions for making high-contact-angle surfaces from low-contact-angle materials. *Langmuir.* **2008**, *24*, 7573-7579
109. Tuteja, A.; Choi, W.; Ma, M. L.; Mabry, J. M.; Mazzella, S. A.; Rutledge, G. C.; McKinley, G. H. Cohen, R. E. Designing superoleophobic surfaces. *Science* **2007**, *318*, 1618-1622
110. Tuteja, A.; Choi, W.; Mabry, J. M.; McKinley, G. H. Cohen, R. E. Robust omniphobic surfaces. *P Natl Acad Sci USA.* **2008**, *105*, 18200-18205

## BIOGRAPHICAL SKETCH

Shu-Hau Hsu was born in a rural township on the coast in northern Taiwan. He did his undergraduate and master's studies both in Materials Science Department at National Cheng Kung University, Tainan, Taiwan. During his undergraduate, he was awarded *Dr. Paul C.W. Chu* Material Science Scholarship, a prestigious four-year national scholar-ship, which ultimately led him to explore superconductivity. Together with his team-mates, they have built up several systems to demonstrate the super-conducting magnetic levitation. They also have a video on YouTube showing how this phenomenal event works. The video has been watched over 750,000 times (as of Aug. 2010). What he had enjoyed most there was being an instructor for a science camp where he met hundreds of high school students each summer, and they brainstormed together to bring up any possible ideas of utilizing this phenomenon.

After a two-year military service and another two years as a research assistant in Academia Sinica, he continued his education in pursuit of a Doctor of Philosophy degree in the Department of Materials Science and Engineering at University of Florida, Gainesville. He worked with Dr. Wolfgang Sigmund in UF since 2006 on various topics including colloidal processing, novel ceramic casting and his dissertation work—another filed of *super*-property—Superhydrophobicity. They are the first one that successfully developed an artificial hairy surface exhibiting perfect hydrophobicity. This work also made him on the national and international media, including USA Today and Scientific American. He hopes that he can find a way of using his knowledge well and always have the enthusiasm for delivering the aspects of science to the young generation.